

ABSTRACT

COLLINS, JAMES BURTON. Dimension Reduction: Modeling and Numerical Analysis of Two Applied Problems. (Under the direction of Pierre Gremaud.)

In this work we consider two problems, a simplified model for laser drilling, and transport on networks. In both problems, the technique of dimensional reduction is applied. In the model for laser drilling, radial averaging is used to allow for a two-dimensional geometry to be assigned to the domain, while maintaining one-dimensional computation cost. Many network problems inherently use dimensional reduction to model complicated systems on a domain which is a graph.

In addition to radial averaging, the laser drilling model utilizes kinetic theory, and parameter estimation techniques using experimental data. The domain decomposition method is implemented for linear transport problems defined on networks. The convergence of this method is analyzed and *a priori* estimates of the total iterations are established. Network problems are examined locally by considering gas flow through pipe junctions. Algebraic conditions derived to model the multi-dimensional effects occurring at the junctions and the network approximation is validated against the numerical solution of the multi-dimensional problem.

© Copyright 2010 by James Burton Collins

All Rights Reserved

Dimension Reduction: Modeling and Numerical Analysis of
Two Applied Problems

by
James Burton Collins

A dissertation submitted to the Graduate Faculty of
North Carolina State University
in partial fulfillment of the
requirements for the Degree of
Doctor of Philosophy

Mathematics

Raleigh, North Carolina

2010

APPROVED BY:

Ralph Smith

Alina Chertock

Michael Shearer

Jay Tu

Pierre Gremaud
Chair of Advisory Committee

DEDICATION

This work is dedicated to my parents, who always knew I could do this, and supported me every step of the way.

BIOGRAPHY

James Burton Collins, better known as Jeb, was born in Hayward, California. After spending two years in Madrid, Spain, he spent the majority of his childhood in Alexandria, Virginia. He is the son of Craig and Joann Collins, and older brother of Jonathan Collins. He attended Thomas A. Edison High School. After graduating in 2000, he went on to James Madison University in Harrisonburg, Virginia. He graduated in May, 2005 with a Bachelors of Science in Mathematics and Computer Science.

Jeb then went on to attend North Carolina State University for graduate school in mathematics. He obtained his Masters of Science in Applied Mathematics in December of 2007. In December, 2010 he earned his Doctor of Philosophy degree in Mathematics under the guidance of Dr. Pierre Gremaud.

ACKNOWLEDGEMENTS

I would like to begin by thanking my advisor, Dr. Pierre Gremaud, for mentoring me through the hard research years, and for his understanding of my extracurricular mathematical activities. I also thank Jay Tu and Alex Paleocrassas for their help in provided experimental data for the laser drilling model, and Dr. Tu for serving on my committee. I thank my other committee members as well, Ralph Smith, Alina Chertock, and Michael Shearer.

I would like to thank all of the professors here at NC State that have made the past five years both enjoyable and at times stressful, and have helped to shape me into the mathematician that I am today. I also thank Paul and Debra Warne, who showed me I was a mathematician, and without whom I would not have even considered graduate school.

I would also like to thank all of my family, for their support and understanding for all the missed holidays and birthdays. Finally, I would like to thank all my fellow graduate students, for helping me to stay sane and making sure graduate school was always fun.

TABLE OF CONTENTS

List of Tables	viii
List of Figures	ix
Chapter 1 Introduction	1
Chapter 2 Preliminaries	3
2.1 Conservation Laws	3
2.1.1 Characteristic Lines and Characteristic Variables	5
2.1.2 Weak solutions and Rankine-Hugoniot Conditions	7
2.1.3 Entropy Selection Criterion	10
2.1.4 Euler Gas Dynamics Equations	12
2.1.5 Boundary Conditions	16
2.2 Numerical Methods	17
2.2.1 Finite Volume Methods: Godunov Scheme	17
2.2.2 Central Difference Methods	21
Chapter 3 Model of Laser Drilling	25
3.1 Introduction	25
3.1.1 Previous Work	26
3.1.2 Overview of the Model	28
3.2 Model of Workpiece	28
3.2.1 Heat Equation	30
3.2.2 Radial Averaging	30
3.2.3 Boundary Conditions	35
3.3 Model of the Vaporized Material	36
3.3.1 Kinetic Theory of Gases	37
3.3.2 Knudsen Layer	38
3.3.3 Jump Conditions for Knudsen Layer	39
3.3.4 Closing the system	41
3.3.5 Summary of Equations	44
3.4 Computing the Speed of Drilling	45
3.4.1 Equation for U	45
3.4.2 Determining U by iteration	46
3.5 Implementation of the Model	47
3.6 Results	49
3.7 Conclusions	52

Chapter 4 Transport on Networks	54
4.1 Introduction	54
4.1.1 Previous work	57
4.2 Linear Transport Problems	59
4.2.1 Junction Conditions	59
4.2.2 Numerical Procedure for Network Problems	61
4.2.3 Linear Acoustics Equations	61
4.2.4 Junction Conditions for the Linear Acoustics Equations	62
Chapter 5 Domain Decomposition Applied to Network Problems	64
5.1 Introduction	64
5.1.1 Current Work	67
5.2 Convergence Analysis	68
5.2.1 Domain Decomposition Convergence	70
5.2.2 Convergence Variables	73
5.2.3 Generalization to Systems	74
5.2.4 Constant Speed and Constant Length Edges	75
5.2.5 Variable Speed and Edge Length	79
5.2.6 Multi-Edge Subdomains	80
5.3 Numerical Results	84
5.3.1 Justification of the Update Formula	84
5.3.2 Comparison of Iteration Estimates with Numerical Results	87
5.4 Conclusions	93
Chapter 6 Numerical Investigation of Gas Flow through a Nozzle	96
6.1 Introduction	96
6.1.1 Previous Work	97
6.2 Analysis of Nozzle flow equations	97
6.2.1 Derivation	98
6.2.2 Augmented System	101
6.2.3 Analysis of the Riemann Problem	102
6.2.4 Solutions to the Riemann Problem	104
6.2.5 Non-Unique Solutions	106
6.3 Properties of Constructions J2P/J2N	107
6.4 Results	111
6.4.1 Numerical Methods	111
6.4.2 Nozzle Results	113
6.5 Conclusions	123
Chapter 7 Numerical Investigation of Gas Flow through a Splitting Junction	125
7.1 Introduction	125

7.1.1	Previous Work	126
7.1.2	Overview	128
7.2	Split Junction Conditions	128
7.2.1	Splitting Pipe Junction Conditions	130
7.3	Results	133
7.3.1	Numerical Considerations	133
7.3.2	Error Computation	135
7.3.3	Split Results	136
7.4	Conclusions	145
Chapter 8 Conclusions		146
References		148
Appendices		155
Appendix A	Analysis of Φ	156
Appendix B	Proof of Lemma 2	161
Appendix C	Pressure Loss Model Derivation	163

LIST OF TABLES

Table 3.1	Parameters of the heat equations	30
Table 3.2	Material properties of 316 stainless steel and laser parameters; the "star values" are estimated from measured values for iron, the "dagger" values are estimated from 304 stainless steel [13].	49
Table 3.3	Experimental and numerical results.	51
Table 3.4	Results due to varying power profiles.	52
Table 5.1	Comparison of analytical estimates to iteration count for the 3 generation binary tree.	89
Table 5.2	Comparison of analytical estimates to iteration count for the 3 Clusters Network.	90
Table 5.3	Comparison of analytical estimates to iteration count for the Bird Island Network.	92
Table 5.4	Comparison of various partitioning of the caveman network.	92
Table 6.1	Results from varying the initial condition of the J2P construction. Average error can be bounded below the threshold error by setting initial conditions sufficiently close to the left bounding curve.	118
Table 6.2	Results from varying the geometry of the nozzle. Average error can be bounded below the threshold error by setting the jump in area sufficiently small.	121

LIST OF FIGURES

Figure 2.1	Region where discontinuity (shock) $\xi(t)$ exists in the solution. In the open sets D_L and D_R the solution is continuous.	9
Figure 2.2	Structure of a solution to the Euler equations with Riemann initial conditions.	14
Figure 2.3	The curves defining the set of states connected to \mathbf{q}_L by a 1-wave, and \mathbf{q}_R by a 3-wave. Their intersection represent the velocity and pressure of the intermediate state.	16
Figure 2.4	Uniform discretization mesh used for finite volume schemes. . . .	18
Figure 2.5	Staggered grid used in central difference methods.	21
Figure 2.6	Progression for one time step of the Kurganov-Tadmor method. Values of w used to eliminate staggered grid.	23
Figure 3.1	Experimental data showing the spatial dependency of the laser intensity in the x and y directions.	28
Figure 3.2	Three-dimensional representation of the workpiece and hole. Radius of hole at surface is given by R and hole depth is given by ξ	29
Figure 3.3	Assumed hole shapes; left: cone, right: paraboloid.	32
Figure 3.4	Infinitesimal washer over which we integrate to obtain the radially averaged equations.	33
Figure 3.5	Shock waves for subsonic vapor flow near the Knudsen layer. . . .	42
Figure 3.6	Shock waves for supersonic vapor flow near the Knudsen layer. .	43
Figure 3.7	Flow of the model.	46
Figure 3.8	(Left) Profile of the peak laser power as a function of time. (Right) Approximate power profile used in computations.	50
Figure 3.9	Average surface temperature of the dense material as a function of time for the three different hole types.	50
Figure 3.10	Velocity of drilling as a function of time for the three different hole types.	51
Figure 4.1	A sample network [68].	54
Figure 4.2	Visualization of a portion of the Internet network. Example of a network that is on the upper limit of what is useful to visualize [68].	56
Figure 5.1	General domain split into two subdomains.	65
Figure 5.2	A network partitioned into subdomains for application of the domain decomposition method.	67
Figure 5.3	Notation used to describe various types of edges connected to edge i .	70
Figure 5.4	A simple two edge loop network.	71

Figure 5.5	Error propagation after the first iteration for the two-edge loop network.	72
Figure 5.6	Error propagation after second iteration for two-edge loop network. At this iteration a region of exactness exists below the dotted line.	72
Figure 5.7	Two edge straight network. Domain decomposition will converge in two iterations, regardless of final time T	73
Figure 5.8	Convergence variable $\tau_{e_i}^{k+1}$ depends on convergence variables to the left at iteration k , and speed of propagation.	76
Figure 5.9	Sets defining the incoming and outgoing edges adjacent to a multi-edge subdomain.	81
Figure 5.10	Network partitioned into two subdomains, each containing three edges.	82
Figure 5.11	Numerical plot of error propagation for two-edge loop network after first iteration. Nodes used are 300.	85
Figure 5.12	Numerical plot of error propagation for two-edge loop network after second iteration. Nodes used are 300.	85
Figure 5.13	Numerical plot of error propagation for two-edge loop network with variable speed of propagation after first iteration. Nodes used are 300.	87
Figure 5.14	Numerical plot of error propagation for two-edge loop network with variable speed of propagation after second iteration. Nodes used are 300.	87
Figure 5.15	The three-generation binary tree. The multi-edge subdomains are shown.	89
Figure 5.16	The three cluster network with partitioning.	90
Figure 5.17	The traffic network on Bird Island, NC. The six subdomain are shown, three on each side of the main street.	91
Figure 5.18	Caveman network with three "caves" and 8 nodes per cave. Subdomains are defined to take advantage of the clustering inherit to the network.	93
Figure 5.19	Caveman network with three "caves" and 8 nodes per cave. Partitioning does not take advantage of clustering within the network.	94
Figure 6.1	The cross section of the nozzle over which the radial averaging takes place.	98
Figure 6.2	Four main constructions possible with the augmented system of equations.	104
Figure 6.3	Two entropy satisfying solutions to the nozzle equations.	107
Figure 6.4	The left and right bounding curves for construction J2P and $a_L < a_R$	109
Figure 6.5	The discontinuous nozzle geometry.	112
Figure 6.6	A smooth nozzle of width $\epsilon = .25$	112

Figure 6.7	A comparison of the solution of the Riemann problem for nozzles of various widths ϵ . As $\epsilon \rightarrow 0$, the solutions converge to the discontinuous geometry solution.	114
Figure 6.8	The relative error between the smooth nozzle and discontinuous nozzle for $\epsilon \in [.01, .1]$	115
Figure 6.9	Result of initial conditions that give good agreement with multi-dimensional solution. Intersection of the 1- and 3- curves relative to the 3-bounding curves (Top). The exact solution to the one-dimensional problem is compared with the radially averaged solution of the multi-dimensional problem at time $T = .2$ (Bottom). .	116
Figure 6.10	Result of initial conditions that give poor agreement with multi-dimensional solution. Intersection of the 1- and 3- curves relative to the 3-bounding curves(Top). The exact solution to the one-dimensional problem is compared with the radially averaged solution of the multi-dimensional problem at time $T = .2$ (Bottom). .	117
Figure 6.11	Results of the straight pipe geometry, $a_L = a_R$	120
Figure 6.12	Results of a discontinuous nozzle with 20% jump in area.	120
Figure 6.13	Results of a discontinuous nozzle with a 200% jump in area. . . .	121
Figure 6.14	Results for J1 construction.	122
Figure 6.15	Results for J3 construction.	123
Figure 7.1	A generic multi-edge pipe junction with inflow and outflow. . . .	126
Figure 7.2	A generic splitting junction with three pipes. All pipe areas can be different and two angles made by outflow pipes can be different.	127
Figure 7.3	Top portion of the splitting junction domain.	129
Figure 7.4	Diagram of the physics modeled by the pressure loss junction condition.	131
Figure 7.5	Mesh used to simulate a splitting junction for the two-dimensional solution. Black line denotes where one-dimensional domains lies on the mesh.	134
Figure 7.6	Lines used to denote where the junction is in the two-dimensional domain. State variables are averaged over these lines and compared.	135
Figure 7.7	Plot of the error in junction conditions for the two-dimensional solution using initial conditions and geometry (7.17).	137
Figure 7.8	Full two-dimensional solution of the density at the junction. . . .	138
Figure 7.9	Plot of the average mass flow ratio over time with error bars determined by standard deviation. Linear fit is used to determine function $\alpha(\theta)$	139
Figure 7.10	Relative error results for the density, velocity and pressure for initial conditions (7.22) and junction geometry $\theta = \frac{\pi}{6}, \psi = 2$	140
Figure 7.11	Relative error results for the density, velocity and pressure for initial conditions (7.23) and junction geometry $\theta = \frac{\pi}{6}, \psi = 2$	141

Figure 7.12	Relative error results for the density, velocity and pressure for initial conditions (7.24) and junction geometry $\theta = \frac{\pi}{6}, \psi = 2$	141
Figure 7.13	Plot of average error for each variable vs angle.	142
Figure 7.14	Plot of average error for each variable vs ψ	143
Figure 7.15	Two-dimensional solution of the horizontal velocity. Multi-dimensional effects are seen beyond that of a propagating shock wave.	144
Figure 7.16	A test of the modified junction conditions with different initial conditions.	144
Figure A.1	Plot of $\Phi(\rho)$, for $\rho \in [0, \hat{\rho}]$. Area ratio is varied to show examples of two solutions, one solution and no solutions.	158
Figure C.1	Diagram of the physics modeled by the pressure loss junction condition.	164

Chapter 1

Introduction

Physical processes occur in three-dimensions. Mathematical models of these processes can not always incorporate the multi-dimensional aspects, due to the high computational cost. To obtain results in a reasonable time, the dimensions of the model are reduced. This is done by making assumptions about the solution that eliminate the dependency on particular dimensions, and then employing an averaging technique to reduce the information from those dimensions to a point. In this work, we examine two problems that utilize dimension reduction to model multi-dimensional physical processes, laser drilling and transport network problems.

The laser drilling process is inherently three-dimensional, however dimensional reduction can be applied to simplify the mathematical model. The spatial profile of the laser allows us to assume the hole is axisymmetric. Further assumptions on the material being drilled, along with an averaging technique give a one-dimensional model. Reducing the dimensions produces a model that is computationally inexpensive, but the geometry of the laser drilling process.

The premise of transport network problems is to use dimension reduction to simplify a large multi-dimensional system. This system can be a grid of beams, or a network of blood vessels. Each system is made up of large regions for which dimension reduction can be applied. These regions are reduced to one-dimensional domains, represented by edges in the network. This reduction allows a large multi-dimensional system to be solved in tractable time. The regions for which dimension reduction does not work well are approximated through other means. We study these regions for the particular application of gas flow, determining the accuracy of the approximations. We also study

the application of the domain decomposition method to such problems, in an effort to again increase speed.

In Chapter 2, we introduce some preliminary concepts about conservation law for those who are not familiar. We also introduce the numerical methods we use that are not well known. Chapter 3 discusses the laser drilling model and its results. Network problems are introduced in chapter 4. Chapter 5 discusses the domain decomposition methods applied to network problems, and chapters 6 and 7 describe the pipe junction models for two distinct junctions and their results. Finally, chapter 8 presents some final comments and summarizes the results from this work.

Chapter 2

Preliminaries

In this chapter we discuss some preliminary concepts used throughout this dissertation. Section 2.1 covers the general theory of conservation laws. We review the definition of a weak solution, as well as the various types of solutions that are created by the Riemann problem. Finally we consider the non-uniqueness of solutions of conservation laws and review the entropy condition used to select a unique solution. In Section 2.2 we review the numerical methods used to solve the partial differential equations that arise from both the laser drilling model and the conservation laws considered in the network problems.

2.1 Conservation Laws

Much of this dissertation will involve work with conservation laws, therefore this section will give a brief overview of what these types of partial differential equations are, as well some of their properties [55], p. 422. Conservation laws derive their name from the types of physical situations they are usually used to model. These are models in which a substance or quantity $q : \mathbb{R}^d \times \mathbb{R}^+ \mapsto \mathbb{R}$ is neither created nor destroyed during the process, that is q is conserved. Consider a region $\Omega \subset \mathbb{R}^d$, we can measure the quantity q within Ω by integrating,

$$Q = \int_{\Omega} q d\mathbf{x}. \tag{2.1}$$

Let us consider the time derivative of Q . Since we assume that q is conserved, the change of Q will depend upon how q changes at the boundary $\partial\Omega$ of Ω ,

$$\frac{d}{dt}Q := \frac{d}{dt} \int_{\Omega} q d\mathbf{x} = \text{net flux across } \partial\Omega, \quad (2.2)$$

We let \mathbf{n} be the outward unit normal to the boundary, and,

$$\mathbf{f}(q) = \begin{pmatrix} f_1(q) \\ \vdots \\ f_d(q) \end{pmatrix} \quad (2.3)$$

be the flux vector, where $f_i(q)$ represents the flux of q through the boundary $\partial\Omega$ in the i^{th} coordinate direction. We rewrite (2.2) as [33], p. 1,

$$\frac{d}{dt} \int_{\Omega} q d\mathbf{x} = - \int_{\partial\Omega} \mathbf{f}(q) \cdot \mathbf{n} dS. \quad (2.4)$$

This is the integral form of the conservation law. We have assumed for simplicity that the flux functions depend solely on q . By the application of the divergence theorem and assuming q is smooth Equation (2.4) becomes,

$$\int_{\Omega} \frac{\partial q}{\partial t} + \nabla \cdot \mathbf{f}(q) d\mathbf{x}. \quad (2.5)$$

Since (2.5) must hold for any arbitrary region Ω , we have,

$$\frac{\partial q}{\partial t} + \nabla \cdot \mathbf{f}(q) = 0. \quad (2.6)$$

If we assign an initial condition $q_0(\mathbf{x})$ at time $t = 0$ we obtain the Cauchy problem,

$$\frac{\partial q}{\partial t} + \nabla \cdot \mathbf{f}(q) = 0 \quad (2.7)$$

$$q(\mathbf{x}, 0) = q_0(\mathbf{x}), \quad (2.8)$$

in $\mathbb{R}^d \times \mathbb{R}^+$.

In the above example we considered a scalar quantity q . It is also possible to consider a vector valued function and a conservation law of similar form can be derived [33], p. 1.

The partial differential equation (2.6) is also not required to be homogeneous, that is it can be of the form,

$$\frac{\partial q}{\partial t} + \nabla \cdot \mathbf{f}(q) = \psi(q). \quad (2.9)$$

Equations such as (2.9) are often called balance laws. These represent quantities which are not conserved within a region but whose change with time must be balanced by both the flux through the boundary and the source term $\psi(q)$ [55], pp. 375-416.

2.1.1 Characteristic Lines and Characteristic Variables

For the following discussion we consider one-dimensional conservation laws. An important property of conservation laws are the characteristic curves. These are curves in the x - t plane along which the solution of the equation is constant.

Assuming the solution $q(x, t)$ is smooth, we define the characteristic curve of (2.6) by,

$$\dot{X}(t) = f'(q(X(t), t)). \quad (2.10)$$

Since the flux depend on q only, and q is constant along $X(t)$, we see that the characteristic curve is a straight line.

Characteristic curves are very useful, especially in the linear case, i.e. where $f(q)$ is a linear function, that is,

$$f(q) = aq, \quad a \in \mathbb{R}. \quad (2.11)$$

Here we see that $f'(q)$ has a constant slope for all q , so all characteristic lines have the same slope in the x - t plane. The characteristics can be used to solve (2.7)-(2.8) with flux function (2.11), which is often called an advection equation. Given any point (x^*, t^*) , we can follow the unique characteristic line through (x^*, t^*) back to the initial condition to obtain,

$$q(x^*, t^*) = q_0(x^* - at^*). \quad (2.12)$$

This demonstrates an important property of conservation laws, that information travels

with a finite speed of propagation.

When $\mathbf{q}(x, t) : \mathbb{R} \times \mathbb{R}^+ \mapsto \mathbb{R}^n$ is a vector valued function the linear conservation law is given by,

$$\frac{\partial}{\partial t}\mathbf{q} + \frac{\partial}{\partial x}A\mathbf{q} = 0, \quad A \in \mathbb{R}^{n \times n}. \quad (2.13)$$

Therefore $f'(\mathbf{q}) = A$. A similar procedure to the scalar case can be used to solve the case of linear systems, but we must first convert our equation into characteristic variables [55], p. 47-61. In order to define characteristic variables, we assume that Equations (2.13) is strictly hyperbolic.

Definition 1. A system of hyperbolic partial differential equations given in the following form,

$$\frac{\partial}{\partial t}\mathbf{q} + \frac{\partial}{\partial x}f(\mathbf{q}) = 0, \quad (2.14)$$

is called **strictly hyperbolic** if all the eigenvalues of $f'(\mathbf{q}) = A$ are real and distinct [9].

Since, in the linear case, $f'(\mathbf{q}) = A$, this implies that A is diagonalizable with real eigenvalues. We decompose A as

$$A = R\Lambda R^{-1}, \quad (2.15)$$

where,

$$\Lambda = \text{diag}(\lambda_1, \lambda_2, \dots, \lambda_n) \quad (2.16)$$

$$R = [\mathbf{r}_1, \mathbf{r}_2, \dots, \mathbf{r}_n] \quad (2.17)$$

$$R^{-1} = [\mathbf{l}_1, \mathbf{l}_2, \dots, \mathbf{l}_n]^T. \quad (2.18)$$

The left and right eigenvectors of A are given by \mathbf{l}_i and \mathbf{r}_i respectively, and the eigenvalues of A are given by λ_i . We left multiply Equation (2.13) by R^{-1} to get,

$$\frac{\partial}{\partial t}\mathbf{w} + \Lambda \frac{\partial}{\partial x}\mathbf{w} = 0, \quad (2.19)$$

where,

$$\mathbf{w} = R^{-1}\mathbf{q}, \quad (2.20)$$

are the characteristic variables. This turns a coupled system of conservation laws into a decoupled system of advection equations, each with speed of propagation λ_i . We solve each of these advection equations in the same way as above, and then convert back to our state variables \mathbf{q} . The final solution is given by,

$$\mathbf{q}(x, t) = \sum_{p=1}^n [\mathbf{l}_p \mathbf{q}_0(x - \lambda_p t)] \mathbf{r}_p. \quad (2.21)$$

In the case of multiple dimensions, characteristic curves are not as simple. The flux function $\mathbf{f}(\mathbf{q})$ is a vector, and there exist multiple matrices A_1, A_2, \dots, A_d , one for each dimension. Theory exists to define a strictly hyperbolic problem, and characteristic *surfaces*, however determining a solution is not as simple as for the one-dimensional case. For more information see [33], p. 306, and references therein.

2.1.2 Weak solutions and Rankine-Hugoniot Conditions

Solutions to conservation laws are often not smooth. This causes a problem when considering the partial differential equation these solutions must satisfy, as their derivatives may not exist in the classical sense. This is dealt with by redefining the solutions to Equation (2.7)-(2.8) in a weak sense [33], p. 15. The goal of the weak formulation of the problem is to move the derivatives off the state variable. We start by integrating (2.7) against a function $\phi \in \mathcal{C}_0^1(\mathbb{R}^d \times \mathbb{R}^+)$, the space of differentiable functions with compact support, across the space and time domain.

$$\int_0^\infty \int_{\mathbb{R}^d} \left[\frac{\partial q}{\partial t} + \nabla \cdot \mathbf{f}(q) \right] \phi(x, t) d\mathbf{x} dt = 0 \quad (2.22)$$

Then, using Green's theorem, we move the derivatives off of q and onto ϕ to get,

$$\int_0^\infty \int_{\mathbb{R}^d} \left[q \frac{\partial \phi}{\partial t} + \mathbf{f}(q) \cdot \nabla \phi \right] d\mathbf{x} dt = - \int_{\mathbb{R}^d} q_0(x) \phi d\mathbf{x}. \quad (2.23)$$

We can now define a weak solution.

Definition 2. A function $q(\mathbf{x}, t)$ is a **weak solution** of (2.6) with initial condition $q_0(\mathbf{x})$, if (2.23) is satisfied for all $\phi \in \mathcal{C}_0^1(\mathbb{R}^d \times \mathbb{R}^+)$.

Assume that $q(x, t)$ is a solution to (2.7)-(2.8), that we know to be piecewise \mathcal{C}^1 . That is, $q \in \mathcal{C}^1$ everywhere in except along finitely many smooth surfaces $\xi(t)$ in (\mathbf{x}, t) -space, and across these surfaces there exists a jump discontinuity in q . Let $\mathbf{n} = \langle \mathbf{n}_t, \mathbf{n}_x \rangle$ denote a normal vector to $\xi(t)$. The following theorem gives a relation that must hold across each surface $\xi(t)$ [33], p. 16.

Theorem 1. *Let $q(\mathbf{x}, t) : \mathbb{R}^d \times \mathbb{R}^+ \rightarrow \mathbb{R}$ be a piecewise \mathcal{C}^1 function as described above. If q is a weak solution to (2.6) then the following conditions hold,*

1. q is a classical solution to (2.6) everywhere that it is \mathcal{C}^1 .
2. Across the surfaces $\xi(t)$ where a jump discontinuity exists, the following relation holds,

$$\mathbf{n}_t(q_R - q_L) + [\mathbf{f}(q_R) - \mathbf{f}(q_L)] \cdot \mathbf{n}_x = 0 \quad (2.24)$$

where

$$q_L = \lim_{\epsilon \rightarrow 0^+} q((\xi(t), t) - \epsilon \mathbf{n}), \quad q_R = \lim_{\epsilon \rightarrow 0^+} q((\xi(t), t) + \epsilon \mathbf{n})$$

Proof. The first condition is easy to prove simply by considering (2.23) in a domain where q is \mathcal{C}^1 and using integration by parts to move the derivatives back onto q , which we can do since q is \mathcal{C}^1 . To prove the second condition we consider a region $D = D_R \cup D_L$ of (\mathbf{x}, t) -space which contains one of the curves of discontinuity $\xi(t)$, where D_L and D_R are the two open components of D on either side of $\xi(t)$. Figure 2.1 shows this region D , split into its two components, in the one-dimensional case. We consider (2.23) on D , taking $\phi \in \mathcal{C}_0^1(D)$, and split the integral across the curve of discontinuity to get,

$$\begin{aligned} 0 &= \int_D q \frac{\partial}{\partial t} \phi + \mathbf{f}(q) \cdot \nabla \phi \, d\mathbf{x} dt \\ &= \int_{D_L} q \frac{\partial}{\partial t} \phi + \mathbf{f}(q) \cdot \nabla \phi \, d\mathbf{x} dt + \int_{D_R} q \frac{\partial}{\partial t} \phi + \mathbf{f}(q) \cdot \nabla \phi \, d\mathbf{x} dt \end{aligned}$$

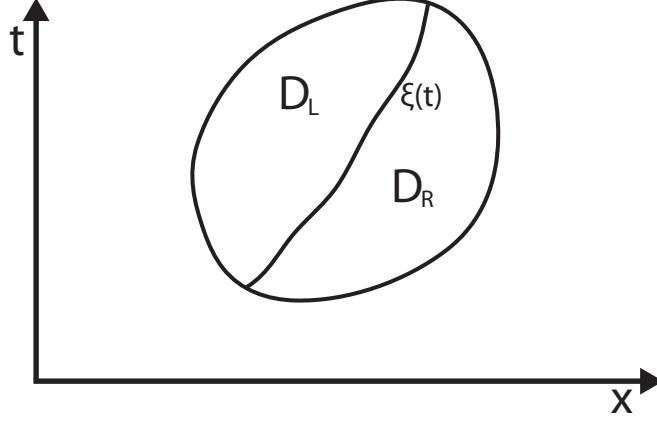


Figure 2.1: Region where discontinuity (shock) $\xi(t)$ exists in the solution. In the open sets D_L and D_R the solution is continuous.

We now use Green's identity on each component of D . We define the outward normal along $\xi(t)$ of D_R to be $\mathbf{n}_R = \langle \mathbf{n}_t, \mathbf{n}_x \rangle$, where $\mathbf{n}_t \in \mathbb{R}$ and $\mathbf{n}_x \in \mathbb{R}^d$, and the outward normal of D_L to be $\mathbf{n}_L = -\mathbf{n}_R$.

$$\begin{aligned}
0 &= - \int_{D_L} \phi \nabla_{(t,\mathbf{x})} \cdot \begin{pmatrix} q \\ \mathbf{f}(q) \end{pmatrix} d\mathbf{x}dt + \int_{\xi(t)} \phi \begin{pmatrix} q_L \\ \mathbf{f}(q_L) \end{pmatrix} \cdot \mathbf{n}_L dt \\
&\quad - \int_{D_R} \phi \nabla_{(t,\mathbf{x})} \cdot \begin{pmatrix} q \\ \mathbf{f}(q) \end{pmatrix} d\mathbf{x}dt + \int_{\xi(t)} \phi \begin{pmatrix} q_R \\ \mathbf{f}(q_R) \end{pmatrix} \cdot \mathbf{n}_R dt \\
&= - \int_{D_L} \phi [q_t + \nabla \cdot \mathbf{f}(q)] d\mathbf{x}dt - \int_{\xi(t)} \phi [\mathbf{n}_t q_L + \mathbf{f}(q_L) \cdot \mathbf{n}_x] dt \\
&\quad - \int_{D_R} \phi [q_t + \nabla \cdot \mathbf{f}(q)] d\mathbf{x}dt + \int_{\xi(t)} \phi [\mathbf{n}_t q_R + \mathbf{f}(q_R) \cdot \mathbf{n}_x] dt \\
&= \int_{\xi(t)} \phi [\mathbf{n}_t (q_R - q_L) + [\mathbf{f}(q_R) - \mathbf{f}(q_L)] \cdot \mathbf{n}_x] dt.
\end{aligned} \tag{2.25}$$

Since this must hold for all $\phi \in \mathcal{C}_0^1(D)$, we get,

$$\mathbf{n}_t (q_R - q_L) + [\mathbf{f}(q_R) - \mathbf{f}(q_L)] \cdot \mathbf{n}_x = 0 \tag{2.26}$$

□

Equation (2.26) is called the Rankine-Hugoniot jump condition. It must hold over

all discontinuities for conservation laws, and is used to determine the solution for such equations, as well as the speed and direction of propagation. In the one-dimensional case (2.26) becomes,

$$s(q_R - q_L) = f(q_R) - f(q_L), \quad (2.27)$$

where $s = \dot{\xi}(t)$ is the speed of the discontinuity.

2.1.3 Entropy Selection Criterion

The weak formulation of the problem allows the solution to have discontinuities and gives information about the solution near those discontinuities. However, with these benefits of the weak solution, there are also problems that occur, and must be dealt with. The problem we explain here is the loss of uniqueness to the solution. For this discussion we consider the one-dimensional conservation law. We demonstrate with the following example. Consider the inviscid Burger's equation with piecewise constant initial conditions,

$$\frac{\partial}{\partial t} u + \frac{\partial}{\partial x} \left(\frac{u^2}{2} \right) = 0 \quad (2.28)$$

$$u(x, 0) = u_0(x) = \begin{cases} u_L, & x < 0 \\ u_R, & x > 0 \end{cases}. \quad (2.29)$$

A conservation law with such initial conditions is called a *Riemann problem*. If $u_L \neq u_R$, we can use the Rankine-Hugoniot jump conditions to propagate the initial discontinuity with speed $s = \frac{u_L + u_R}{2}$. However, if $u_L < u_R$, we can also create a solution of the form,

$$u(x, t) = \begin{cases} u_L, & x \leq u_L t \\ \frac{x}{t}, & u_L t \leq x \leq u_R t \\ u_R, & x \geq u_R t \end{cases}. \quad (2.30)$$

Thus we have at least two weak solutions to the same initial value problem. So we see that we must have some kind of selection criterion, to determine which solution is the correct one. One selection criterion is called the vanishing viscosity technique. Certain conservation laws, are approximations of more complicated models. An example of such

a conservation law is Euler gas dynamics. These equations approximate the Navier-Stokes equations, which include viscosity terms. The Euler equations approximate the Navier-Stokes equations by removing the viscosity terms. This is the physical reasoning behind the vanishing viscosity technique. The idea is to augment (2.7)-(2.8) with a small viscosity term,

$$\frac{\partial}{\partial t} q_\epsilon + \frac{\partial}{\partial x} f(q_\epsilon) = \epsilon \frac{\partial^2}{\partial x^2} q_\epsilon \quad (2.31)$$

$$q_\epsilon(\mathbf{x}, 0) = q_0(\mathbf{x}). \quad (2.32)$$

Equation (2.31)-(2.32) has a unique solution, under suitable conditions on the initial conditions, due to the smoothing property of parabolic equations. Therefore, the solution of (2.31)-(2.32) as $\epsilon \rightarrow 0$, if it exists, is defined to be the correct solution to the conservation law and is called the vanishing viscosity solution [9].

The vanishing viscosity method is difficult to implement, as a closed form solution of the parabolic equation can not always be found or the limiting solution as $\epsilon \rightarrow 0$ is difficult to obtain. An equivalent criterion was developed to select the vanishing viscosity solution, the entropy selection criterion. This theory is based on the physical principle that entropy must be nondecreasing with time. When modeling gas dynamics, this principle is used to select the physically meaningful solution. The entropy selection criterion extends this physical principle to apply it to general conservation laws to select the vanishing viscosity solution. The full theory involved and the details are not given here, see [50], [33], p. 21-34, 303-315 and references therein for a full explanation.

Under certain conditions given in [50], the entropy selection criterion can determine the correct solution by examination of the flux function. Let us consider a system of conservation laws in one dimension,

$$\frac{\partial \mathbf{q}}{\partial t} + \frac{\partial}{\partial x} \mathbf{f}(\mathbf{q}) = 0. \quad (2.33)$$

Assuming that (2.33) is strictly hyperbolic, we have that the Jacobian $f'(\mathbf{q})$ has real and distinct eigenvalues which we order such that,

$$\lambda_1(\mathbf{q}) < \lambda_2(\mathbf{q}) < \dots < \lambda_n(\mathbf{q}). \quad (2.34)$$

The following condition determines when a discontinuity in the solution satisfies the

entropy selection criterion [50].

Lax Entropy Condition: Given a system of conservation laws (2.33), let \mathbf{q} be a weak solution of (2.33) with a discontinuity propagating with speed s that separates the values \mathbf{q}_L and \mathbf{q}_R . Assume \mathbf{q} satisfies the conditions set forth in [50]. The weak solution \mathbf{q} satisfies the entropy selection criterion if there exists an index k such that,

$$\begin{aligned}\lambda_{k-1}(\mathbf{q}_L) &< s < \lambda_k(\mathbf{q}_L) \\ \lambda_k(\mathbf{q}_R) &< s < \lambda_{k+1}(\mathbf{q}_R),\end{aligned}\tag{2.35}$$

defining $\lambda_0 = -\infty$ and $\lambda_{n+1} = \infty$.

The Lax entropy condition gives a method to check whether a shock is an admissible solution. This condition essentially states that there exists one set of characteristic that impinge on the shock, and all other characteristics cross the shock. This can be written for a scalar conservation law as,

$$f'(q_L) > s > f'(q_R).\tag{2.36}$$

If a shock does not satisfy the Lax entropy criterion, then a different solution is used to connect the states \mathbf{q}_L to \mathbf{q}_R .

2.1.4 Euler Gas Dynamics Equations

The previous sections apply to general conservation laws. One in particular that is often used, and of interest to this work is the Euler gas dynamics equations. The one-dimensional version is given by the following system,

$$\frac{\partial}{\partial t}\rho + \frac{\partial}{\partial x}(\rho u) = 0\tag{2.37}$$

$$\frac{\partial}{\partial t}(\rho u) + \frac{\partial}{\partial x}(\rho u^2 + p) = 0 \quad \text{in } \mathbb{R} \times \mathbb{R}^+\tag{2.38}$$

$$\frac{\partial}{\partial t}E + \frac{\partial}{\partial x}(u(E + p)) = 0.\tag{2.39}$$

The state variables being modeled are the density ρ , the momentum ρu , and the total energy E . The entropy of the system is denoted by S . This represents the disorder present in the gas. The pressure p is given by a constitutive equation which depends on the type of gas being modeled. For our discussions, we will assume a polytropic ideal gas,

which states that the gas obeys the ideal gas law, and that internal energy is proportional to the temperature [55], p. 294. The constitutive equation for this type of gas is given by,

$$p = (\gamma - 1)E - \frac{\gamma - 1}{2}\rho u^2 \quad (2.40)$$

where γ is the ratio of specific heats. For example, if the gas is air, $\gamma = 1.4$.

In this section we describe how to determine the solution of the Riemann problem for the system (2.37) - (2.39). Therefore, we have the following initial conditions,

$$\mathbf{q}_0(x) = \begin{cases} \mathbf{q}_L, & x < 0 \\ \mathbf{q}_R, & x > 0 \end{cases} \quad (2.41)$$

where $\mathbf{q} = (\rho, \rho u, E)^T$. Many details are involved in solving a Riemann problem for systems of equations, most of which will be left out of this discussion. Here we simply give the reader a general idea of how such problems are solved.

First we consider a spectral decomposition of the Jacobian of the flux for the gas dynamics equations. The Jacobian is given by,

$$f'(\mathbf{q}) = \begin{bmatrix} 0 & 1 & 0 \\ \frac{1}{2}(\gamma - 3)u^2 & (3 - \gamma)u & \gamma - 1 \\ \frac{1}{2}(\gamma - 1)u^3 - uH & H - (\gamma - 1)u^2 & \gamma u \end{bmatrix} \quad (2.42)$$

where,

$$H = \frac{E + p}{\rho}. \quad (2.43)$$

The eigenvalues of (2.42) are,

$$\lambda^1 = u - c \quad \lambda^2 = u \quad \lambda^3 = u + c \quad (2.44)$$

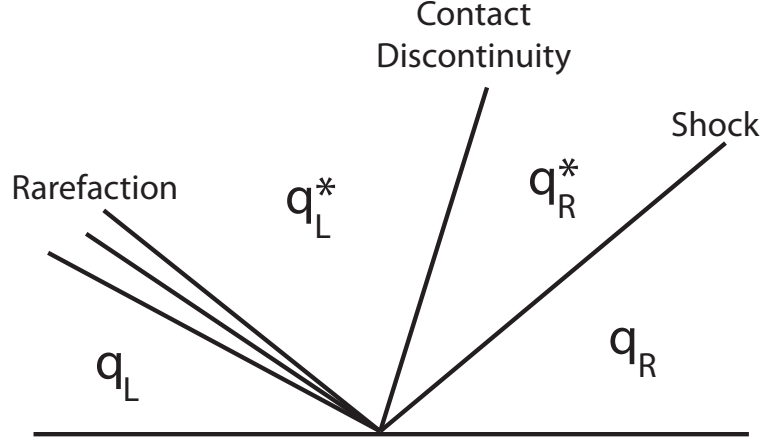


Figure 2.2: Structure of a solution to the Euler equations with Riemann initial conditions.

where $c = \sqrt{\frac{\gamma p}{\rho}}$ is the speed of sound. The respective eigenvectors are,

$$\mathbf{r}^1 = \begin{bmatrix} 1 \\ u - c \\ H - uc \end{bmatrix} \quad \mathbf{r}^2 = \begin{bmatrix} 1 \\ u \\ \frac{1}{2}u^2 \end{bmatrix} \quad \mathbf{r}^3 = \begin{bmatrix} 1 \\ u + c \\ H + uc \end{bmatrix}. \quad (2.45)$$

From the theory of systems of conservation laws [55], p. 260, we know that there will exist three “waves”, or changes in the solution, with an intermediate constant state between the waves, see Figure 2.2. Each wave is associated with an eigenvalue-eigenvector pair (λ^i, r^i) of the Jacobian. There are three types of waves that can exist for the gas dynamics equations, each characterized by the associated eigenvalue of the wave. Let \mathbf{q}_L^i and \mathbf{q}_R^i denote the constant state to the left and right of the i^{th} wave respectively.

The first type of wave is a shock, which is mentioned above as a discontinuity in the solution traveling with a set speed determined by the Rankine-Hugoniot condition. This wave is characterized by the Lax entropy condition (2.35). If the Lax entropy condition is not satisfied, and $\lambda_i(\mathbf{q}_L^i) \neq \lambda_i(\mathbf{q}_R^i)$, then the wave is a rarefaction. This is a continuous but not smooth solution that connect the two states. Finally there is a contact discontinuity. This is a discontinuity that propagates with speed $s = \lambda_i(\mathbf{q}_L^i) = \lambda_i(\mathbf{q}_R^i)$.

For each wave there exist Riemann invariants. These are quantities that are invariant

across rarefactions and contact discontinuities [33]. For the Euler gas dynamics equations, there exist two Riemann invariants for each wave given by,

$$\text{1-Wave: } \frac{p}{\rho^\gamma}, \quad u + \frac{2c}{\gamma - 1} \quad (2.46)$$

$$\text{2-Wave: } u, \quad p \quad (2.47)$$

$$\text{3-Wave: } \frac{p}{\rho^\gamma}, \quad u - \frac{2c}{\gamma - 1}. \quad (2.48)$$

By examining the eigenvalues of the Jacobian, we determine that the 1-wave and 3-wave is either shocks or rarefactions, while the 2-wave is a contact discontinuity [55], p. 300. From the Riemann invariants given above we see that u and p are continuous across the contact discontinuity. Since we know the basic structure of the solution to the Riemann problem, solving it is reduced to determining whether the 1-wave and 3-wave are shocks or rarefactions, and determining the intermediate states that develop between the left and right state, see Figure 2.2. Since u and p are constant across the contact discontinuity, to determine those variables we only consider relations from the 1-wave and 3-wave.

The idea behind determining the intermediate states u^* and p^* is to use the properties of a rarefaction wave and shock to create a one-dimensional family of states in (p, u) -space that can be connected to \mathbf{q}_L by a 1-wave, and then do the same for the 3-wave connected to \mathbf{q}_R . We can find a unique intermediate state by finding the state that is contained in both of these families. The family for the 1-wave is defined by the following equation,

$$u = \begin{cases} u_L + \frac{2c_L}{\gamma - 1} \left[1 - \left(\frac{p}{p_L} \right)^{(\gamma-1)/(2\gamma)} \right] & p \leq p_L \\ u_L + \frac{2c_L}{\sqrt{2\gamma(\gamma-1)}} \left(\frac{1 - p/p_L}{\sqrt{1 + \beta p/p_L}} \right) & p > p_L \end{cases} \quad (2.49)$$

where $\beta = \frac{\gamma+1}{\gamma-1}$. The two parts of the curve correspond to a rarefaction and a shock, and the conditions that define which equation to use correspond to the Lax entropy condition.

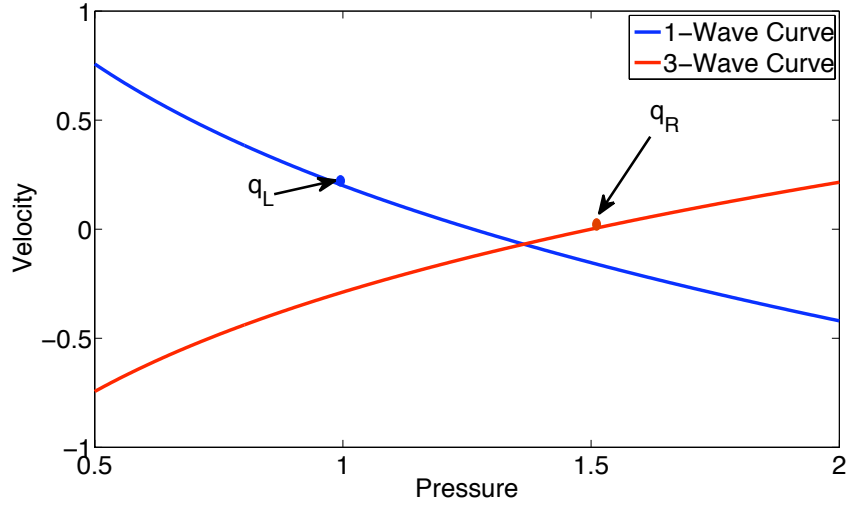


Figure 2.3: The curves defining the set of states connected to \mathbf{q}_L by a 1-wave, and \mathbf{q}_R by a 3-wave. Their intersection represent the velocity and pressure of the intermediate state.

Similar equations can be written for the 3-wave,

$$u = \begin{cases} u_R - \frac{2c_R}{\gamma - 1} \left[1 - \left(\frac{p}{p_R} \right)^{(\gamma-1)/(2\gamma)} \right] & p \leq p_R \\ u_R - \frac{2c_R}{\sqrt{2\gamma(\gamma-1)}} \left(\frac{1 - p/p_R}{\sqrt{1 + \beta p/p_R}} \right) & p > p_R \end{cases}. \quad (2.50)$$

So the to find the intermediate pressure and velocity, we need to find the intersection of these two curves. It can be proven that the 1-wave curve is decreasing, and the 3-wave is increasing [85], so that their intersection is unique, see Figure 2.3. Once p and u are determined, we can use the properties of the 1-wave and 3-wave to determine ρ_L^* and ρ_R^* on either side of the contact discontinuity.

2.1.5 Boundary Conditions

Finally, we want to discuss how to implement boundary conditions for conservation laws in one dimension. When considering a bounded domain, we must look at the characteristic lines to determine how to set the boundary conditions. Depending on the

characteristic structure at the boundary, certain variables can be determined from initial conditions, while others must be set using boundary conditions. This is due to the direction in which the characteristic lines propagate. So we see that the number of boundary conditions needed depends on the characteristic structure, that is the direction of the characteristic lines, at that boundary [33], p. 423-426.

Dealing with boundary conditions is very different depending on whether the problem is linear or nonlinear. For linear problems, the characteristic structure can be determined from the eigenvalues and does not change with time. Theory has been developed to implement boundary conditions for linear problems in multiple dimensions [44]. Setting boundary conditions for nonlinear problems is still an open area of research, see [26, 70] and [33], pp. 435-442. The method for nonlinear problems used in this work is to linearize the equations about the solution at the boundary at each point in time, and then apply the techniques for linear problems [39].

2.2 Numerical Methods

While the work presented here is not directly related to numerical discretization schemes for hyperbolic equations, such schemes are used extensively to achieve our results. We therefore give a brief discussion here regarding the numerical schemes used throughout the research.

There are two schemes used throughout this work, the first-order Godunov scheme [34], and the second-order Kurganov-Tadmor scheme [47]. Both of these are finite volume methods, though the Kurganov-Tadmor scheme belongs to a subclass called central difference methods. Here we describe the idea behind finite volume methods, and these two schemes in particular.

2.2.1 Finite Volume Methods: Godunov Scheme

Finite volume methods are a widely used class of numerical method for solving conservation laws. These methods are very similar to finite differences. In fact, many first order finite difference methods, such as Lax-Friedrichs and upwind, can be developed from a finite volume viewpoint. The main difference between the two types is in definition of the spatial values.

Let us consider the following mesh of one-dimensional space and time, see Figure 2.4.

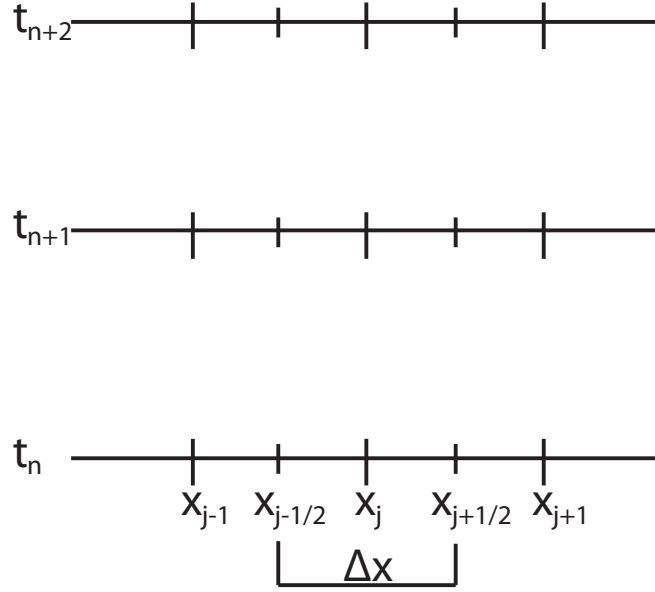


Figure 2.4: Uniform discretization mesh used for finite volume schemes.

We partition the temporal domain into equidistant subintervals $[t_n, t_{n+1}]$ of length Δt , where,

$$t_n := n\Delta t \quad n = 0, 1, \dots \quad (2.51)$$

Similarly we partition the spatial domain into equidistant subintervals $[x_j, x_{j+1}]$ of length Δx , where,

$$x_j = j\Delta x \quad j = \dots, -2, -1, 0, 1, 2, \dots \quad (2.52)$$

Finite differences approximates the solution at the points of the mesh. Let $q(x, t)$ be the exact solution, a finite difference method would define q_j^n at each mesh point by,

$$q_j^n \approx q(x_j, t_n). \quad (2.53)$$

In contrast, finite volume methods approximate the spatial average of the solution over

a small interval of each mesh point,

$$q_j^n \approx \frac{1}{\Delta x} \int_{\mathcal{C}_j} q(x, t_n) dx, \quad (2.54)$$

where \mathcal{C}_j is a small interval around the point x_j .

We introduce these methods for a scalar conservation law in one dimension as done in [55], p. 64. Let us define the cell average of the solution at each grid point by,

$$Q_j^n := \frac{1}{\Delta x} \int_{\mathcal{C}_j} q(x, t_n) dx. \quad (2.55)$$

The first step is to integrate the conservation law across the spatio-temporal box $\mathcal{C}_j \times (t_n, t_{n+1})$. For now, we let $\mathcal{C}_j = (x_{j-1/2}, x_{j+1/2})$, where $x_{j\pm 1/2} = x_j \pm \frac{\Delta x}{2}$. This gives,

$$\begin{aligned} \int_{x_{j-1/2}}^{x_{j+1/2}} q(x, t_{n+1}) dx - \int_{x_{j-1/2}}^{x_{j+1/2}} q(x, t_n) dx &= \int_{t_n}^{t_{n+1}} f(q(x_{j-1/2}, t)) dt \\ &\quad - \int_{t_n}^{t_{n+1}} f(q(x_{j+1/2}, t)) dt. \end{aligned} \quad (2.56)$$

Rearranging and dividing by Δx we get,

$$Q_j^{n+1} = Q_j^n - \frac{1}{\Delta x} \left[\int_{t_n}^{t_{n+1}} f(q(x_{j+1/2}, t)) dt - \int_{t_n}^{t_{n+1}} f(q(x_{j-1/2}, t)) dt \right]. \quad (2.57)$$

Since the solution is given at $t = 0$, we know Q_j^0 for all j . We use (2.57) iteratively to determine the solution at each time t_n . This process is exact if the integrals in (2.57) can be evaluated, however this is usually not that case as the integrals depend upon the solution. Therefore, let us define,

$$F_{j+1/2}^n \approx \frac{1}{\Delta t} \int_{t_n}^{t_{n+1}} f(q(x_{j+1/2}, t)) dt, \quad (2.58)$$

to approximate the integrals. $F_{j+1/2}^n$ is called the numerical flux it is defined by the method used to approximate the integral. Rewriting (2.57) in terms of the numerical fluxes we have,

$$Q_j^{n+1} \approx Q_j^n - \frac{\Delta t}{\Delta x} [F_{j+1/2}^n - F_{j-1/2}^n]. \quad (2.59)$$

Each finite volume method is defined by the choice of numerical flux, that is by the method used to approximate the flux integrals. Recalling that $q_j^n \approx Q_j^n$, we write the update formula for the approximate solution as,

$$q_j^{n+1} = q_j^n - \frac{\Delta t}{\Delta x} [F_{j+1/2}^n - F_{j-1/2}^n]. \quad (2.60)$$

To define the numerical fluxes for the first-order Godunov scheme, we begin by assuming q_j^n is known for all j . We define the reconstructed solution at time t^n to be,

$$\tilde{q}^n(x, t_n) = q_j^n \quad \forall \quad x \in \mathcal{C}_j. \quad (2.61)$$

We then evolve $\tilde{q}^n(x, t_n)$ to time $t = t_{n+1}$. This is done by considering each discontinuity as a local Riemann problem. The time step Δt is chosen such that the waves from adjoining subintervals do not interact. Once we have evolved the solution, we know that it will be constant along the ray $(x - x_{j+1/2})/t = 0$. This says that

$$\tilde{q}^n(x_{j+1/2}, t) = \tilde{q}^n(x_{j+1/2}, t_{n+1}) \quad \forall \quad t \in (t_n, t_{n+1}). \quad (2.62)$$

By substituting $\tilde{q}^n(x_{j+1/2}, t_{n+1})$ in Equation (2.58), we obtain an approximation for $F_{j+1/2}^n$, that can be used in Equation (2.57), and give the first-order Godunov scheme for a scalar conservation law in one dimension,

$$F_{j-1/2}^n = \begin{cases} \min_{q_{j-1}^n \leq p \leq q_j^n} f(p) & \text{if } q_{j-1}^n \leq q_j^n \\ \min_{q_j^n \leq p \leq q_{j+1}^n} f(p) & \text{if } q_j^n \leq q_{j+1}^n \end{cases}. \quad (2.63)$$

Higher-order Godunov schemes can be derived by using higher-order polynomial reconstructions of the solution. However, care must be taken when reconstructing using high-order polynomials to ensure that undesired oscillations are not introduced [40, 61, 81]. While this method is very good at solving Riemann problems and propagating discontinuities in the solution, it has some difficulties as well. For many nonlinear problems, a solution of the Riemann problem may be very difficult to obtain, or may not exist. Approximate Riemann solvers have been introduced to deal with this [77], but they can also be computationally expensive.

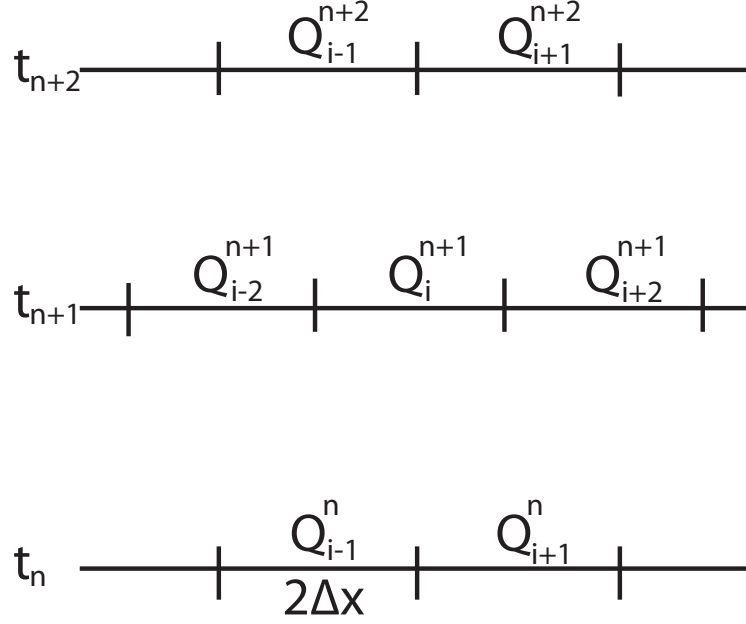


Figure 2.5: Staggered grid used in central difference methods.

2.2.2 Central Difference Methods

Central difference schemes were introduced by Nessyahu and Tadmor [67] as an alternative finite volume scheme that could handle discontinuities without requiring Riemann solvers. An example of such a method is the Lax-Friedrichs method, the numerical flux for which is,

$$F_{j-1/2}^n = \frac{1}{2}[f(q_{j-1}^n) + f(q_j^n)] - \frac{\Delta x}{2\Delta t}(q_j^n - q_{j-1}^n). \quad (2.64)$$

This method does not use a Riemann solver and can be applied to very general problems. The downside is that it is first-order and introduces a high amount of diffusivity into the solution. We introduce central schemes by showing how Lax-Friedrichs can be derived as one.

Central difference methods work by defining the interval \mathcal{C}_j around each point x_j as (x_{j-1}, x_{j+1}) , so that the cells are twice the length. A staggered grid is then defined at each time step, as seen in Figure 2.5. The conservation law is integrated across the region $\mathcal{C}_j \times (t_n, t_{n+1})$ as above. The approximate cell averages q_j^n are known at time

t_n . This is used to create a piecewise polynomial approximation $\tilde{q}(x, t_n)$ which is used to evaluate the flux integrals. A higher order polynomial approximation yields a higher order method. If a piecewise constant approximation is used, the Lax-Friedrichs method is obtained [55], pp. 198-199.

The method used in this work utilizes a piecewise linear approximation and incorporates local speed of propagation into the calculations. It was developed by Kurganov and Tadmor[46]. It is second order and does not use a staggered grid. The method can be written in semi-discrete form,

$$\frac{d}{dt}q_j(t) = -\frac{F_{j+1/2}(t) - F_{j-1/2}(t)}{\Delta x}. \quad (2.65)$$

Here we see we have discretized in spatial, and left the temporal derivative alone. The function $q_j(t)$ denotes the approximation within the cell \mathcal{C}_j as a function of time. This allows us to use high order temporal discretizations.

The numerical fluxes defined in [47] are given by,

$$F_{j+1/2}(t) = \frac{a_{j+1/2}^+ f(q_{j+1/2}^-) - a_{j+1/2}^- f(q_{j+1/2}^+)}{a_{j+1/2}^+ - a_{j+1/2}^-} + \frac{a_{j+1/2}^+ a_{j+1/2}^-}{a_{j+1/2}^+ - a_{j+1/2}^-} [q_{j+1/2}^+ - q_{j+1/2}^-]. \quad (2.66)$$

The linear reconstruction gives the following definitions,

$$q_{j+1/2}^+ = q_{j+1} - \frac{\Delta x}{2}(q_x)_{j+1} \quad (2.67)$$

$$q_{j+1/2}^- = q_j + \frac{\Delta x}{2}(q_x)_j \quad (2.68)$$

where $(q_x)_j$ is an approximation of the derivative within the cell using a limiter such as minmod [36, 51, 71].

Finally, the local speed of propagation is introduced through the values of $a_{j+1/2}^+$ and $a_{j+1/2}^-$. We denote $\frac{\partial f}{\partial q}$ as the Jacobian of the flux for a system of conservation laws, and we order its eigenvalues so that $\lambda_1 < \dots < \lambda_N$. Then we have that,

$$a_{j+1/2}^+ := \max_{\omega \in C(q_{j+1/2}^-, q_{j+1/2}^+)} \left\{ \lambda_N \left(\frac{\partial f}{\partial q}(\omega) \right), 0 \right\} \quad (2.69)$$

$$a_{j+1/2}^- := \min_{\omega \in C(q_{j+1/2}^-, q_{j+1/2}^+)} \left\{ \lambda_1 \left(\frac{\partial f}{\partial q}(\omega) \right), 0 \right\}, \quad (2.70)$$

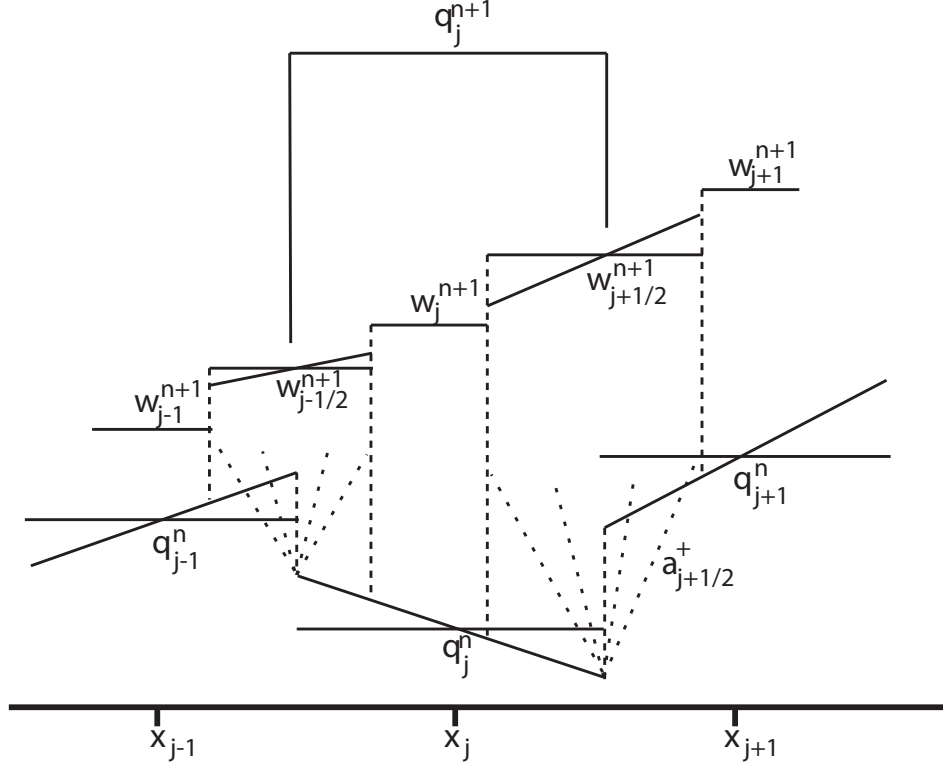


Figure 2.6: Progression for one time step of the Kurganov-Tadmor method. Values of w used to eliminate staggered grid.

where $C(q_{j+1/2}^-, q_{j+1/2}^+)$ is the curve in phase space connecting the two states. These quantities approximate the left and right speed of propagation of the waves created by the discontinuities between cells. For the flux functions we consider, these can be rewritten as,

$$a_{j+1/2}^+ = \max \left\{ \lambda_N \left(\frac{\partial f}{\partial q}(q_{j+1/2}^-) \right), \lambda_N \left(\frac{\partial f}{\partial q}(q_{j+1/2}^+) \right), 0 \right\} \quad (2.71)$$

$$a_{j+1/2}^- = \min \left\{ \lambda_1 \left(\frac{\partial f}{\partial q}(q_{j+1/2}^-) \right), \lambda_1 \left(\frac{\partial f}{\partial q}(q_{j+1/2}^+) \right), 0 \right\}. \quad (2.72)$$

This method is illustrated in Figure 2.6. We see the linear reconstruction of the cell averages at time t_n . The rays emanating from the discontinuities show the maximum distance the waves can travel, as given by $a_{j+1/2}^+$ and $a_{j+1/2}^-$. The values of w are used by the method to eliminate the need for a staggered grid, making the method easier

to implement. Finally all these values are combined to obtain the updated solution approximation q_j^{n+1} .

Chapter 3

Model of Laser Drilling

3.1 Introduction

Since the invention of lasers by Maiman in 1960 [86], researchers have found many uses in different areas. Lasers are used to create circuit boards [75]. They can be used for alignment purposes, as in an atomic force microscope [78]. Lasers have also found many applications in medical fields, such as dentistry [74] or biomedical devices [42]. Finally, lasers can be used in machinery, which include cutting, welding and drilling [76]. This work is interested in the use of lasers in drilling.

Laser drilling is used mostly on metals and ceramics [76]. The process of laser drilling is mainly thermal, where the energy from a high powered laser is used to melt or evaporate the material to be drilled. There are two types of drilling methods, percussion and trepanning. In trepan drilling, the laser is moved about the circumference of the hole to cut out the shape desired [21]. In percussion drilling, both the laser and the workpiece remain stationary and material is removed until the desired depth is reached. Percussion drilling can also use multiple short pulses instead of a single pulse. The disadvantage of multiple pulses is that some of the material begins to solidify and must be melted again with each pulse. When high powered lasers are used, lasers with intensity in the range $> 10^5 \text{ W/cm}^2$, material is removed through both vaporization and melt ejection [30]. Through the process of vaporization, the material is heated by the laser intensity above its melting point and evaporates. Melt ejection is a byproduct of vaporization. As the material evaporates, the vapor creates pressure which acts on the liquid material and forces it in a radial direction removing it from the hole [30].

Laser drilling has many advantages over traditional drilling techniques. First equipment failure does not depend on the amount of use of the laser. In traditional drilling techniques, some kind of a bit is used to drill into the material. After a certain number of times used, the bit will fail and must be replaced. While a laser can still malfunction, it does not wear out as a bit does. A laser also has very low heat output to the surrounding area of the hole. Due to the thermal nature of the drilling process, lasers are able to drill into a wider range of materials, such as ceramics, that would prove difficult with mechanical drilling due to cracking. Laser drilling can also be easily automated for production lines, being able to drill at a rate of 100 holes per second. The diameter and shape of the hole can be changed without needing to change bits. Finally, a unique property of laser drilling is the size of hole that can be drilled. Depending on the power and duration of pulse, holes can be made with a diameter on the nanometer scale. This is not achievable by any mechanical method [14, 76].

3.1.1 Previous Work

There are many aspects involved in laser drilling. As mentioned above, evaporation and melt ejection are the two main processes by which material is removed from a workpiece. A model including melt ejection was first introduced by von Allmen [1]. This used a recoil pressure induced from the vaporization to model the ejection of the liquid material. Chan and Mazumder [12] created a model that used both melt ejection as well as evaporation to model material removal. This one-dimensional steady-state model treats both the solid-liquid and the liquid-vapor interfaces as free boundaries. The solid-liquid interface was modeled as a classical Stefan problem. A classical Stefan problem models the phase change of a material, tracking the free boundary between the phases [64]. A Knudsen layer was assumed to form between the liquid and the vapor. This is a small region where the vapor is in a non-equilibrium state represented by a boundary layer in the solution [43]. A discontinuity in the states was assumed to exist across this layer. The equations describing the states on either side of this discontinuity were obtained from the well-cited Knight paper [43]. This model was used to study the damage done to the material due to the evaporation and melt ejection. Transient two dimensional models were considered by both Ganesh [30] and by Kar and Mazumder [41]. The model by Ganesh put great emphasis on the melting and solidification process. They assumed the temperature to be constant across the liquid-vapor interface, and did not take the free boundary of the hole

into account in their boundary conditions. Kar and Mazumder created a model to study the damage done to a material by the drilling process. They utilized the conservation of energy, that is the Stefan condition, at the solid-liquid and liquid-vapor interface. The Stefan condition, as well as the effects of the curvature of the hole, were taken into account at various places along the hole shape and then interpolation was used to determine the size and shape of the hole.

The above models incorporated the power from the laser by way of energy conservation. This is essentially considering the power flux as a surface element. Another method that has been used is to consider the power flux as a volumetric element. This is the method used by Yilbas [92, 93, 94]. He initially studied the steady state problem of laser drilling with a volumetric source term. He was able to determine an analytical solution for the temperature profile within the dense phase. He then considered the one-dimensional time-dependent problem. Again the temperature profile was determined analytically using Laplace transform. Then the full two-dimensional time-dependent problem was considered with an enthalpy method used to model phase change from solid to liquid. This sequence of three papers is a good example of how models for laser drilling have been taken from an initial state and grown to incorporate more of the physics involved in the process.

Recently, work has been done to model some of the more complicated aspects of laser drilling. For instance the plasma, that is ionized vapor, that can be created during laser drilling. Sankaranarayanan [79] considered the effect of the vapor and plasma on the laser itself, as well as the surface temperature of the dense phase. In [84], Solana considers the absorption effect of the vapor on the power of the laser. An averaged absorption coefficient is used to model the attenuation of the laser beam intensity.

Finally, we note the research of Shusser [82]. Here we see a simplified, one-dimensional model presented to describe the laser drilling process. The hole is assumed to be purely one-dimensional and the vapor is fully modeled by gas dynamics. The work presented here follows along these same lines, in that we try to simplify the modeling of the laser drilling process. However, we consider the hole to have an axisymmetric geometry, while keeping the model one-dimensional. We also use the work of [43] to determine only the necessary variables of the vapor, and incorporate experimental data to fit geometrical parameters included in our model.

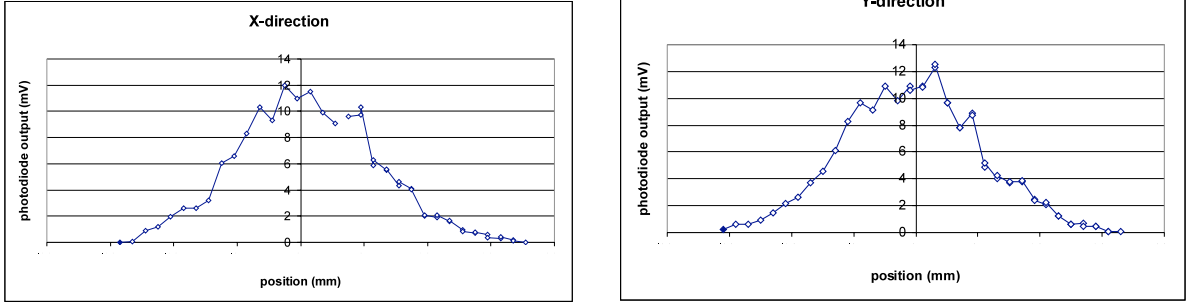


Figure 3.1: Experimental data showing the spatial dependency of the laser intensity in the x and y directions.

3.1.2 Overview of the Model

The purpose of this model is to represent the laser drilling process with low computational costs. To this end, certain simplifying assumptions were made. Regarding the laser process itself, it is assumed that the removal of material is dominated by the vaporization process, therefore melt ejection is not modeled. To simplify calculations, all aspects of the laser drilling process are modeled in one dimension. The vaporized material is assumed to not interact with the laser. Finally the hole is assumed to have axisymmetric geometry.

The model is separated into three parts, the heat transfer, the Knudsen layer, and the computation of the speed of drilling. To solve the heat transfer problem within the solid, radial averaging techniques are used on the heat equation to assume a three-dimensional shape for the hole but keep the model one-dimensional. The Knudsen layer problem employs kinetic theory and the work of Knight [43] to determine the states of the vapor. These values determine the speed of drilling over a particular time step. An iteration procedure is required to determine the speed of drilling since that speed is used in the heat transfer problem. Calculating the speed of drilling over time gives the depth of the hole being drilled, which is compared with experimental data.

3.2 Model of Workpiece

The first component of the model considers the effect of the laser on the solid workpiece that is being drilled. In particular, the temperature of the workpiece is modeled using

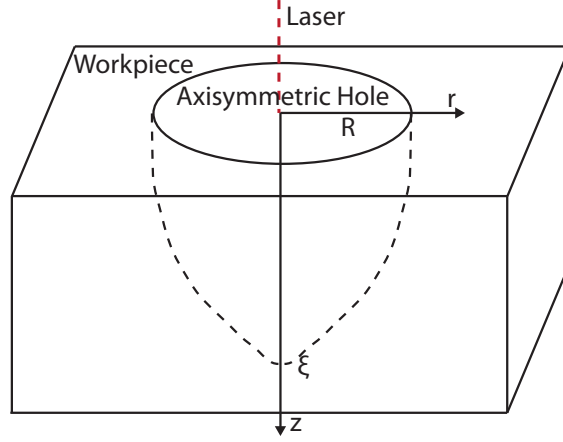


Figure 3.2: Three-dimensional representation of the workpiece and hole. Radius of hole at surface is given by R and hole depth is given by ξ .

the heat equation. The solid portion is assumed to be homogenous. The properties of the laser are obtained from our collaborator Dr. Tu [87]. In particular, the power profile of the laser, that is the spatial dependency of the laser intensity, is shown in Figure 3.1. We approximate this data by defining the laser intensity to have a Gaussian profile,

$$W(r, t) = W_0(t)e^{-2(r/R_b)^2}, \quad (3.1)$$

where r is the radial distance from the center of the laser beam. The peak laser intensity $W_0(t)$ is obtained from experiments. Experimentalists also define a laser beam radius R_b , which is defined as the radius at which the laser intensity is $W_0(t)e^{-2}$.

These assumptions on the material and laser beam lead to an axisymmetric model. Therefore we consider the problem in cylindrical coordinates as shown in Figure 3.2.

3.2.1 Heat Equation

The problem is considered to be axisymmetric, and cylindrical coordinates are used, therefore the heat equation for the solid is written in the following form,

$$\rho_s c_s \frac{\partial T}{\partial t} = k_s \left[\frac{1}{r} \frac{\partial}{\partial r} \left(r \frac{\partial T}{\partial r} \right) + \frac{\partial^2 T}{\partial z^2} \right] \quad r > 0, z > 0, t > 0 \quad (3.2)$$

$$T(r, z, 0) = T_0 \quad r > 0, z > 0 \quad (3.3)$$

$$k_s \nabla T \cdot \mathbf{n} = -W n_z + \rho_s L_v \mathbf{u} \cdot \mathbf{n} \quad (r, z) \in \Gamma \quad (3.4)$$

$$\lim_{r, z \rightarrow \infty} T = T_0 \quad (3.5)$$

where Γ is the boundary of the hole, \mathbf{n} is the outward normal vector at the boundary, and \mathbf{u} is the velocity of the interface at each point along Γ . The physical parameters are listed in Table 3.1. This models the solid region using a two-dimensional equation,

Table 3.1: Parameters of the heat equations

ρ_s (kg/m ³)	Density of the solid
c_s (J/kg K)	Specific heat of the solid
k_s (W/m K)	Thermal conductivity of the solid
L_v (J/kg)	Latent heat of vaporization
W (W/m ²)	Laser intensity
T_0 (K)	Ambient temperature of the solid

however as mentioned before we would like our model to be one-dimensional. Therefore we use radial averaging to reduce (3.2) to a one-dimensional equation.

3.2.2 Radial Averaging

Before we employ averaging techniques, we argue that the variation of the temperature along the radial direction is negligible. This argument justifies using radial averaging, as well as some assumptions used to simplify after averaging is applied. We present this argument by first non-dimensionalizing equation (3.2). We use the following change of

variables,

$$r^* = R_b \quad z^* = \frac{k_s(T_v - T_m)}{W} \quad t^* = \rho_s c_s k_s \frac{(T_v - T_m)^2}{W^2}$$

where R_b is the laser beam radius and T_v, T_m are the vaporization and melting temperature of the material, respectively. We now define our non-dimensional variables,

$$\begin{aligned} \hat{r} &= \frac{r}{r^*} & \hat{z} &= \frac{z}{z^*} \\ \hat{t} &= \frac{t}{t^*} & \hat{T} &= \frac{T - T_m}{T_v - T_m}. \end{aligned}$$

Using these variables in equation (3.2) and dropping the bar notation for simplicity we get,

$$\frac{\partial T}{\partial t} = \epsilon \frac{1}{r} \frac{\partial}{\partial r} \left(r \frac{\partial T}{\partial r} \right) + \frac{\partial^2 T}{\partial z^2}. \quad (3.6)$$

Table 3.2 shows the values for the above variables typical of the experiments simulated. Plugging these values in we see that,

$$\epsilon = \frac{k_s^2 (T_v - T_m)^2}{W^2 R_b^2} \approx 10^{-7} \quad (3.7)$$

This tells us that, compared to the axial direction, the change of the temperature in the radial direction is negligible.

The two shapes assumed are a cone and a paraboloid as seen in Figure 3.3. Since we assume the hole is axisymmetric, we can prescribe the shape of the hole by defining the radius $s(z, t)$ as a function of the depth. The maximum hole depth is denoted by $\xi(t)$, this is the depth of the hole along the z axis. The hole radius is denoted by $R(t)$ and is defined to be the radius of the hole at $z = 0$. The hole depth $\xi(t)$ is the quantity we wish to determine from this model, as it is the most easily verifiable data point, which leaves $R(t)$ as an unknown function. Therefore some assumption must be made about $R(t)$ in order to have a fully determined shape. As stated above, based upon experimental data we assume that the hole radius is proportional to the depth. We define this relation by

$$R(t) = \kappa \xi(t), \quad (3.8)$$

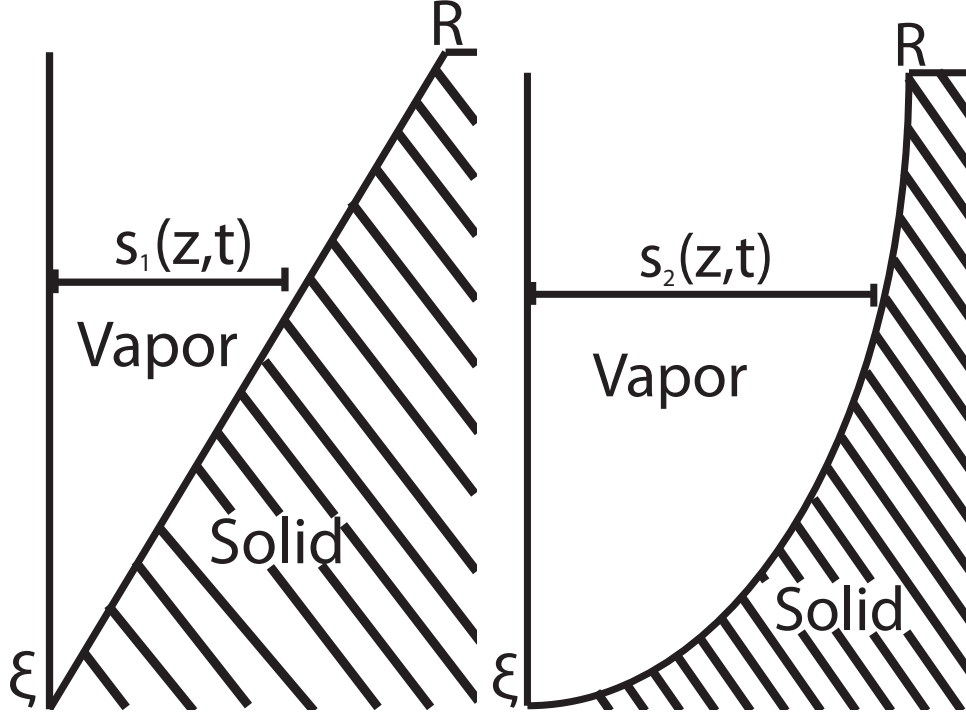


Figure 3.3: Assumed hole shapes; left: cone, right: paraboloid.

where κ is a proportionality constant. We can now define the shapes used by this model.

We define the radius of the cone and paraboloid as a function of the axial direction z and time t to be,

$$s_1(z, t) = \begin{cases} \kappa_1(\xi(t) - z) & \text{if } z < \xi(t) \\ 0 & \text{if } z \geq \xi(t) \end{cases} \quad \textbf{Conical profile} \quad (3.9)$$

$$s_2(z, t) = \begin{cases} \kappa_2\sqrt{\xi^2(t) - \xi(t)z} & \text{if } z < \xi(t) \\ 0 & \text{if } z \geq \xi(t) \end{cases} \quad \textbf{Parabolic profile.} \quad (3.10)$$

While these are the shapes we use in our model, it is interesting to notes that these are specific examples of a more general shape profile,

$$s_\ell(z, t) = \begin{cases} \kappa_\ell (\xi^\ell(t) - \xi(t)^{\ell-1}z)^{\frac{1}{\ell}} & \text{if } z < \xi(t) \\ 0 & \text{if } z \geq \xi(t) \end{cases}.$$

If we take the limit of this general shape profile as $\ell \rightarrow \infty$ we get,

$$\lim_{\ell \rightarrow \infty} s_\ell(z, t) = \begin{cases} \kappa_\infty \xi(t) & \text{if } z < \xi(t) \\ 0 & \text{if } z \geq \xi(t) \end{cases} \quad \textbf{Constant profile.} \quad (3.11)$$

This is the constant profile since we assume that $R(t) = \kappa \xi(t)$. We use this as our third and final profile. Note that using this shape is the same as assuming our problem to be fully one-dimensional, without the radial averaging done below.

We now begin radially averaging (3.2) using a general shape profile $s(z, t)$. We define the radial average of some quantity q by,

$$\begin{aligned} \bar{q}(z, t) &= \frac{1}{\pi(4R^2 - s^2)} \int_0^{2\pi} \int_{s(z, t)}^{2R(t)} q(r, z, t) r dr d\theta \\ &= \frac{2}{4R^2 - s^2} \int_{s(z, t)}^{2R(t)} q(r, z, t) r dr \end{aligned} \quad (3.12)$$



Figure 3.4: Infinitesimal washer over which we integrate to obtain the radially averaged equations.

where we integrate over a washer within the solid at depth z and divide by the area of that washer, see Figure 3.4. To obtain (3.2) in terms of averaged quantities, we apply the above averaging operator to each term in the equation.

We now derive the radially averaged heat equation. First we average the time derivative,

$$\begin{aligned}
\frac{\partial \bar{T}}{\partial t} &= \frac{2}{4R^2 - s^2} \int_{s(z,t)}^{2R(t)} \frac{\partial T}{\partial t} r dr \\
&= \frac{2}{4R^2 - s^2} \frac{\partial}{\partial t} \int_{s(z,t)}^{2R(t)} T r dr + \frac{2}{4R^2 - s^2} \left[T(s, z, t) s \dot{s} - T(R, z, t) R \dot{R} \right] \\
&= \frac{\partial \bar{T}}{\partial t} + \frac{2}{4R^2 - s^2} \left[(R \dot{R} - s \dot{s}) \bar{T} + T(s, z, t) s \dot{s} - T(R, z, t) R \dot{R} \right].
\end{aligned}$$

Next we average the axial derivative,

$$\begin{aligned}
\frac{\partial^2 \bar{T}}{\partial z^2} &= \frac{2}{4R^2 - s^2} \int_{s(z,t)}^{2R(t)} \frac{\partial^2 T}{\partial z^2} r dr \\
&= \frac{2}{4R^2 - s^2} \left[\frac{\partial^2}{\partial z^2} \int_{s(z,t)}^{2R(t)} T r dr + \frac{\partial}{\partial z} (T(s, z, t) s s') + \frac{\partial}{\partial z} (T(R, z, t)) s s' \right] \\
&= \frac{\partial^2 \bar{T}}{\partial z^2} - \frac{4 s s'}{4R^2 - s^2} \left[\frac{\partial \bar{T}}{\partial z} - \frac{\partial}{\partial z} T(s, z, t) \right] - \frac{2((s')^2 + s s'')}{4R^2 - s^2} [\bar{T} - T(s, z, t)].
\end{aligned}$$

We use the dot notation to denote a time derivative, and the prime notation to denote an axial derivative. From arguments above we see that the radial derivative of the temperature is zero. Combining each of these terms we get,

$$\begin{aligned}
\rho_s c_s \frac{\partial \bar{T}}{\partial t} &= k_s \left[\frac{\partial^2 \bar{T}}{\partial z^2} - \frac{4 s s'}{4R^2 - s^2} \left(\frac{\partial \bar{T}}{\partial z} - \frac{\partial}{\partial z} T(s, z, t) \right) - \right. \\
&\quad \left. \frac{2((s')^2 + s s'')}{4R^2 - s^2} (\bar{T} - T(s, z, t)) \right]
\end{aligned}$$

Also from arguments above $\bar{T} = T(s, z, t)$ at each fixed depth z , so the last term in the above equation drops out. Now dropping the bars for convenience the averaged heat equation becomes,

$$\rho_s c_s \frac{\partial T}{\partial t} = k_s \left[\frac{\partial^2 T}{\partial z^2} - \frac{4 s s'}{4R^2 - s^2} \left(\frac{\partial T}{\partial z} - \frac{\partial}{\partial z} T(s, z, t) \right) \right]. \quad (3.13)$$

3.2.3 Boundary Conditions

Next we must average the boundary conditions. The boundary condition at infinity does not change in the averaged case. However, we must deal with the condition at the interface of the hole. Recall that the boundary condition is given by,

$$k_s \nabla T \cdot \mathbf{n} = -W n_z + \rho_s L_v \mathbf{u} \cdot \mathbf{n} \quad (r, z) \in \Gamma. \quad (3.14)$$

This condition is a typical Stefan condition, which results from conservation of energy across the interface. In this case, there is a balance between the input of energy due to the laser power flux, and the loss of energy due to the fact the hole interface is moving.

Due to the non-dimensionalization argument above, the radial component of the temperature gradient term is neglected, giving us an ordinary derivative in the axial direction only. The main complication comes from the moving interface term, namely from calculating the velocity function \mathbf{u} . This function determines how each point on the interface changes with time. In terms of simulating our model; given the interface at time t ,

$$\Gamma(t) = \{(r, z) | 0 \leq z \leq \xi(t), r = s(z, t)\}$$

\mathbf{u} maps $\Gamma(t)$ to $\Gamma(t + \Delta t)$. There is no obvious way to define u ; however, since our goal is a one-dimensional model in the z -direction, we choose to define \mathbf{u} as pointing in the z -direction. Put more precisely, given $\Gamma(t)$ defined by,

$$r = s_\ell(z, t)$$

we can rewrite this as,

$$z = \xi(t) - \frac{r^\ell}{\kappa_\ell^\ell \xi^{\ell-1}(t)}. \quad (3.15)$$

Taking the time derivative of (3.15), we get the velocity in the axial direction. We can then define our velocity function as,

$$\mathbf{u} = \begin{bmatrix} 0 \\ \dot{z} \end{bmatrix} = \begin{bmatrix} 0 \\ \dot{\xi} \left(1 + (\ell - 1) \left(\frac{r^\ell}{\kappa_\ell^\ell \xi^\ell} \right) \right) \end{bmatrix}, \quad (3.16)$$

where $\dot{\xi} = U$ is the speed at which the hole is being drilled, which is still unknown.

Now using (3.16) in the Stefan condition (3.14), we can rewrite it as an averaged boundary condition,

$$\begin{aligned} k_s \frac{\partial}{\partial z} T(s, z, t) &= -W + \rho_s L_v U \left(1 + (\ell - 1) \left(\frac{r^\ell}{\kappa_\ell^\ell \xi^\ell} \right) \right) \\ &= -W + \rho_s L_v u_{z,\ell}, \end{aligned} \quad (3.17)$$

where $\ell = 1, 2$ depending on which shape we choose for the hole.

Our final step is to calculate the temperature at the evaporation front. This scalar value, which we call T_s , will be needed in the final two parts of the model. To convert the temperature at the boundary into a scalar value, we average across the boundary of the hole. This can be done in several ways, we choose to integrate the temperature across the boundary, defining T_s as,

$$T_s = \frac{\int_\Gamma T(r, z, t) dS}{\int_\Gamma dS}, \quad (3.18)$$

where Γ represents the boundary of the hole, therefore the integral in the denominator gives the surface area of the hole.

3.3 Model of the Vaporized Material

The next part of our model considers the state of the evaporated material. Recall that we assume the removal of material is done solely through vaporization. Therefore we must accurately model the vapor created by the drilling process, as it will contribute to calculating hole depth. Early work by Hertz and Knudsen on evaporation of liquid mercury in a vacuum showed that strong phase change processes, such as vaporization by a high powered laser, requires the use of kinetic theory, due to non-equilibrium effects. Therefore, we use kinetic theory, as well as the macroscopic Euler gas dynamics equations to model the state of the vapor.

This section describes kinetic theory, and a phenomenon called the Knudsen layer. An overview of the physics behind the Knudsen layer is given, as well as its properties. Then the use of the physics of the Knudsen layer to our model is given, as well as the process for determining the state of the vapor. This process comes mostly from a well

cited paper in this field by Knight [43].

3.3.1 Kinetic Theory of Gases

Kinetic theory was first developed by Maxwell and Boltzmann to describe the state of gases. Molecules within a gas can be modeled in many ways, but one of the simplest is as a hard elastic sphere. The equations to describe the dynamics of a group of elastic spheres are well known, however, to use these mechanical equations to describe molecules within a gas would be prohibitively difficult, due to the large number of molecules present. Therefore, a statistical approach is necessary to describe gases. Instead of modeling the position and velocity of each molecule, the probability that a particle is at a point \mathbf{x} with velocity $\boldsymbol{\xi}$ is determined [11], pp. 1-2. This method simplifies the equations and computation, but sacrifices information about the particles. However, this loss of information is acceptable since experimentally, we are unable to see this microscopic information of position and velocity. The macroscopic information of temperature, bulk velocity, density, etc., that we are able to determine experimentally, we can obtain from the probabilistic model that we get from kinetic theory.

The particle distribution function $f(\mathbf{x}, \boldsymbol{\xi}, t)$, gives the probability that a particle exists at the point \mathbf{x} and time t with velocity $\boldsymbol{\xi}$. This function can be used to determine the density, bulk velocity, energy, and other macroscopic quantities, as discussed below. The equation which governs f is the Boltzmann equation, given by,

$$\frac{\partial f}{\partial t} + \boldsymbol{\xi} \cdot \frac{\partial f}{\partial \mathbf{x}} = Q(f, f), \quad (3.19)$$

where $Q(f, f)$ is the collision integral. This term takes into account the effect of the molecules colliding with each other and is dependent upon how the molecules are modeled [11], p. 9-11. The Boltzmann equation can be used to derive the macroscopic Euler gas dynamics equations. First we note that there exists a five-dimensional subspace of continuous functions ϕ called collision invariants, that satisfy the property,

$$\int_{\mathbb{R}^3} Q(f, g) \phi(\boldsymbol{\xi}) d\boldsymbol{\xi} = 0, \quad (3.20)$$

for any distribution functions f and g . This subspace is spanned by the following func-

tions, usually called the elementary collision invariants [10], p. 72-78,

$$\phi_1(\boldsymbol{\xi}) = 1 \quad (3.21)$$

$$\phi_2(\boldsymbol{\xi}) = \xi_1 \quad (3.22)$$

$$\phi_3(\boldsymbol{\xi}) = \xi_2 \quad (3.23)$$

$$\phi_4(\boldsymbol{\xi}) = \xi_3 \quad (3.24)$$

$$\phi_5(\boldsymbol{\xi}) = \|\boldsymbol{\xi}\|^2. \quad (3.25)$$

Now, if we integrate a particle distribution function f against a collision invariant with respect to $\boldsymbol{\xi}$, we get the following macroscopic quantities,

$$\int_{\mathbb{R}^3} f d\boldsymbol{\xi} = \rho(\mathbf{x}, t) \quad (\text{density}) \quad (3.26)$$

$$\int_{\mathbb{R}^3} f \xi_i d\boldsymbol{\xi} = \rho(\mathbf{x}, t) u_i(\mathbf{x}, t) \quad (\text{bulk momentum}) \quad (3.27)$$

$$\int_{\mathbb{R}^3} f \|\boldsymbol{\xi}\|^2 d\boldsymbol{\xi} = 2e(\mathbf{x}, t) \quad (\text{specific energy}) \quad (3.28)$$

where $u_i(\mathbf{x}, t)$ is the bulk velocity in the i^{th} coordinate direction, and $e(\mathbf{x}, t)$ is the energy density. Finally, if we integrate the Boltzmann equation against each collision invariant over velocity space, and after some manipulation we can obtain the Euler gas dynamics equations. This method of integrating a distribution function against a function of collision invariants is called the method of moments [11], pp. 16-19.

3.3.2 Knudsen Layer

We now take a closer look at the processes that are involved when a laser is applied to a solid or liquid material, in particular the evaporation and condensation processes. We assume a dense material, evaporating into a vapor. Molecules from this dense material evaporate according to some distribution function, which depends on parameters such as the temperature of the material. At the same time, molecules in the vapor are condensing. When the system is in equilibrium, the rate of evaporation and condensation is equal, and the state properties of the vapor and dense material become the same. However, in general these rates are not equal, and thus the system is not in equilibrium. This leads to a net transport of material, as well as a difference in the temperature, pressure

and density between the vapor and the dense material. This difference in states causes a boundary layer to be created near the dense material in which non-equilibrium effects occur. This boundary layer has a thickness on the order of the molecular mean free path and is called the Knudsen layer [95].

The non-equilibrium effects in the Knudsen layer require the use of the Boltzman equation to determine what goes on inside of the layer. For the process of evaporation, we consider the one-dimensional steady state Boltzman equation,

$$\xi_y \partial_y f(\mathbf{x}, \boldsymbol{\xi}) = Q(f, f). \quad (3.29)$$

Both Cercignani [11] and Ytrehus [95] examined the solution to (3.29). They proved that for a solution of this form to exist, $M_\infty < 1$, where M_∞ is the Mach number of the vapor molecules. Therefore, the vapor just outside the Knudsen layer is required to be subsonic. This will be useful when considering the jump conditions across the Knudsen layer.

3.3.3 Jump Conditions for Knudsen Layer

Due to the complexity of the physics within the Knudsen layer, we assume it to be infinitesimally thin. This introduces a discontinuity between the state of the dense material and the state of the vapor. Kinetic theory can be used to describe this discontinuity and determine conditions that must hold across it.

In [43], Knight calculates the jump conditions that hold across the Knudsen layer. These are Rankine-Hugoniot like conditions which relate the state of the dense material to the state of the vapor. Certain assumptions are made by Knight for this calculation. First, it is assumed that thermal equilibrium is achieved by the gas on the outside of the Knudsen layer. The emitted particles are also assumed to be in thermal equilibrium with the solid before they are emitted. These assumptions lead to the following distribution function at the phase interface,

$$f = \begin{cases} \rho_s (2\pi R T_s)^{-3/2} \exp \left[-\frac{\xi_x^2 + \xi_y^2 + \xi_z^2}{2 R T_s} \right] & \xi_z > 0 \\ \beta \rho (2\pi R T)^{-3/2} \exp \left[-\frac{\xi_x^2 + \xi_y^2 + (\xi_z - u)^2}{2 R T} \right] & \xi_z < 0 \end{cases}, \quad (3.30)$$

where ρ_s is the saturation vapor density, R is the specific gas constant, T_s is the tem-

perature of the solid at the evaporation front, ρ, u , and T are the density, velocity and temperature of the gas, respectively, and ξ_i are the components of the velocity vector. The parameter β will be determined below. Finally, all back-scattered particles are assumed to condense on the surface of the solid.

Using the distribution function (3.30), we determine the relations across the boundary by the following conditions,

$$\rho u = \int_{\mathbb{R}^3} \xi_z f d\boldsymbol{\xi} \quad (3.31)$$

$$\rho u^2 + p = \int_{\mathbb{R}^3} \xi_z^2 f d\boldsymbol{\xi} \quad (3.32)$$

$$u(E + p) = \int_{\mathbb{R}^3} \frac{1}{2} \|\boldsymbol{\xi}\|^2 \xi_z f d\boldsymbol{\xi} \quad . \quad (3.33)$$

which state that mass, momentum and energy must be conserved across the Knudsen layer. After integrating and much algebraic manipulation, we obtain the following jump conditions for the temperature and density,

$$\frac{T}{T_s} = \left[\sqrt{1 + \pi \left(\frac{\gamma - 1}{\gamma + 1} \frac{m}{2} \right)^2} - \sqrt{\pi} \frac{\gamma - 1}{\gamma + 1} \frac{m}{2} \right]^2 \quad (3.34)$$

$$\frac{\rho}{\rho_s} = \frac{F^- + \sqrt{\frac{T}{T_s}} G^-}{2e^{-m^2} \frac{T}{T_s}}, \quad (3.35)$$

with the parameter β given by,

$$\beta = \left[(2m^2 + 1) - m \sqrt{\frac{\pi T_s}{T}} \right] e^{m^2} \frac{\rho_s}{\rho} \sqrt{\frac{T_s}{T}}, \quad (3.36)$$

where,

$$m = \frac{u}{\sqrt{2RT}} \quad (3.37)$$

$$F^-(m) = e^{-m^2} - \sqrt{\pi} m \operatorname{erfc}(m) \quad (3.38)$$

$$G^-(m) = (2m^2 + 1) \operatorname{erfc}(m) - \frac{2}{\sqrt{\pi}} m e^{-m^2}. \quad (3.39)$$

The variable m is a dimensionless quantity which represents the evaporation rate.

Using equations (3.34) - (3.35), and the state of the solid from our heat model in Section 3.2, we can calculate the state variables of the gas. However, we are missing information on the variable m .

3.3.4 Closing the system

The final equation needed to close the Knudsen layer jump conditions is derived from the physics of the expanding vapor [43]. We know the vapor is expanding into ambient air and that it obeys the Euler gas dynamics equations. Since the vapor is expanding rapidly due to the high power of the laser, a shock wave develops between the vapor and the ambient air. From the Euler gas dynamics equations, there exists a Rankine-Hugoniot jump condition that relates the state of the vapor to the state of the ambient air across the shock wave, which can be written as,

$$u_v = \frac{c_a \left(\frac{p_v}{p_a} - 1 \right)}{\gamma_a \sqrt{1 + \frac{\gamma_a + 1}{2\gamma_a} \left(\frac{p_v}{p_a} - 1 \right)}}, \quad (3.40)$$

where $c_i = \sqrt{\gamma_i R_i T_i}$ is the sound speed, and the subscripts a, v represent ambient air and vapor respectively.

We manipulate (3.34), (3.35) to generate a scalar equation for m . With this equation we can solve for m , and then determine the state of the vapor near the Knudsen layer. We recall from Section 3.3.2, that the vapor near the Knudsen layer can not be supersonic, therefore extra care must be taken for vapor that is supersonic away from the Knudsen layer. Finally we use an empirical model to relate the temperature of the solid to the saturation pressure called the Clausius-Clapeyron relation, given by,

$$\frac{p_s}{p_a} = \exp \left[\frac{L_v}{R_v T_{\text{ref}}} \left(1 - \frac{T_{\text{ref}}}{T_s} \right) \right]. \quad (3.41)$$

where the reference temperature T_{ref} is the temperature required for the solid to produce vapor with pressure p_a . The details of how the above equations are combined into a scalar equation for m are presented in [43] for both the subsonic and supersonic cases. We summarize the derivation below.

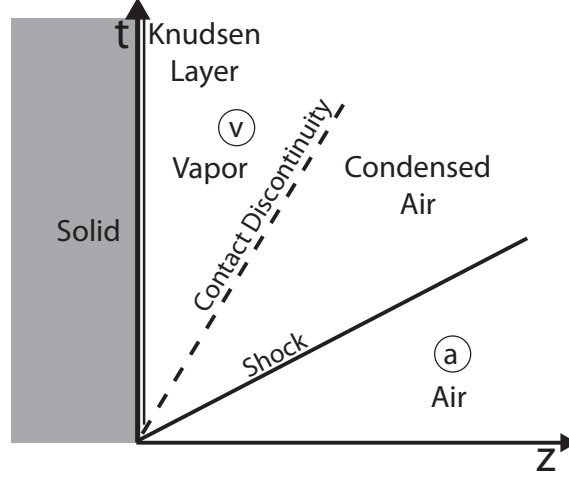


Figure 3.5: Shock waves for subsonic vapor flow near the Knudsen layer.

Subsonic Case

In the first situation we assume the ejected vapor is subsonic or sonic. This situation is represented by Figure 3.5. In this case, the shock wave between the vapor and the ambient air gives enough information to complete the system. We rearrange equation (3.40) by solving for $\frac{p_v}{p_a}$ to get,

$$\frac{p_v}{p_a} = 1 + \gamma_a M_v \frac{c_v}{c_a} \left[\frac{\gamma_a + 1}{4} M_v \frac{c_v}{c_a} + \sqrt{1 + \left(\frac{\gamma_a + 1}{4} M_v \frac{c_v}{c_a} \right)^2} \right], \quad (3.42)$$

where $M_v = \frac{u_v}{c_v}$ is the Mach number of the vapor. Using equation (3.37) and the definition of the speed of sound given above, we write the Mach speed as $M_v = m \sqrt{\frac{2}{\gamma_v}}$. Finally, using the Knudsen layer jump condition (3.34), c_v is a function of m and T_s . Therefore, equation (3.42) relates p_v and m with T_s and the state of the ambient air as parameters. Next, we write the ratio of the vapor pressure and the saturation pressure in terms of the Knudsen layer jump conditions using the ideal gas law,

$$\frac{p_v}{p_s} = \frac{\rho_v T_v}{\rho_s T_s}. \quad (3.43)$$

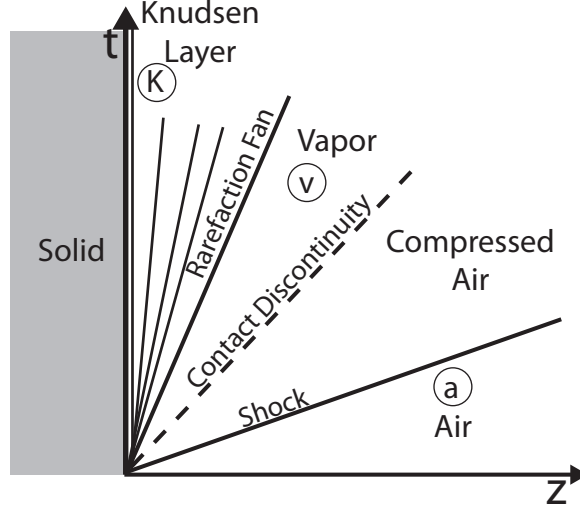


Figure 3.6: Shock waves for supersonic vapor flow near the Knudsen layer.

Equation (3.43) is a function of m due to the Knudsen layer jump conditions given above.

Finally, we combine equations (3.42) and (3.43) in the following way,

$$\frac{p_s}{p_a} = \frac{p_v}{p_a} \left(\frac{p_v}{p_s} \right)^{-1}. \quad (3.44)$$

Using the Clasiuss-Clayperon relation (3.41), we write p_s in terms of T_s , so equation (3.44) is a scalar nonlinear equation for m alone.

Supersonic Case

As stated above, the vapor near the Knudsen layer can not move faster than the sound speed, so in order for the ejected vapor to be supersonic, a rarefaction wave is produced. The situation where supersonic vapor occurs is shown in Figure 3.6. The vapor at the Knudsen layer will be sonic, and directly after the Knudsen layer a rarefaction wave will take the vapor to supersonic speeds. After this wave, the same interaction takes place between the supersonic vapor and the ambient air as in the subsonic case.

A similar procedure can be used to determine the scalar equation for m in this case, with an adjustment that must be made to account for the rarefaction wave. First, the states we are trying to determine, ρ_v and T_v , are no longer near the Knudsen layer, but

are downwind of the rarefaction wave, therefore the Knudsen layer jump conditions (3.34) - (3.35) no longer relate the state of the solid to ρ_v and T_v . Instead, these equations now relate the temperature of the solid to the sonic vapor near the Knudsen layer, ρ_K and T_K . We use the fact that these states are sonic, which implies that $m = \sqrt{\frac{\gamma_v}{2}}$, and the jump conditions to determine ρ_K, T_K and p_K .

We next use the properties of the rarefaction wave to relate the pressure near the Knudsen layer to the supersonic pressure. From conservation law theory, we know that Riemann invariants are constant throughout a rarefaction fan. From the Euler gas dynamics equations we know that the entropy S as well as $P = \frac{2c}{\gamma - 1} + u$ are Riemann invariants for this particular wave. Using the fact that $u_K = c_K$, we can derive the following relation,

$$\frac{c_K}{c_v} = \left(\frac{p_K}{p_v} \right)^{\frac{\gamma_v - 1}{2\gamma_v}} = \frac{2}{\gamma_v + 1} + \frac{\gamma_v - 1}{\gamma_v + 1} M_v. \quad (3.45)$$

Finally, we again use the Rankine-Hugoniot condition that comes from the shock between the compressed and ambient air. The derived equation is the same, however in the supersonic case we can not relate the speed of sound c_v to m simply. To do this, we note the trivial equation,

$$\frac{c_v}{c_a} = \sqrt{\frac{\gamma_v R_v T_K}{\gamma_a R_a T_a}} \left(\frac{c_K}{c_v} \right)^{-1}. \quad (3.46)$$

Combining this with equation (3.45) we relate c_v to our parameter m .

Using the jump conditions (3.34) - (3.35) to determine p_K and T_K , and equations (3.45), (3.41) and (3.42), we get the following equation,

$$\frac{p_s}{p_a} = \frac{p_K}{p_v} \frac{p_v}{p_a} \left(\frac{p_K}{p_s} \right)^{-1}. \quad (3.47)$$

3.3.5 Summary of Equations

We now have taken the Knudsen layer jump conditions, along with equations from the physics of the vapor, and reduced them to a scalar equation for m which depends on the temperature of the solid at the surface, T_s , for both the subsonic (3.44) and supersonic

(3.47) case. This equation can be solved numerically to determine m . For the subsonic case, it is then straightforward to determine the states of the vapor, since they are involved in the jump conditions. However, for the supersonic case, the jump conditions give the states near the Knudsen layer, whereas we want the states of the supersonic vapor. To determine these states we use equations (3.45) and (3.46) to determine c_v . Using c_v we determine T_v, p_v and ρ_v .

3.4 Computing the Speed of Drilling

The final step, and in fact the purpose, of the model is to calculate U , the speed at which the hole depth is increasing. The value for U is determined by assuming the vapor satisfied the same Maxwellian properties listed above, and using the continuity equation. Recall that the boundary condition used in the heat transfer model (3.17), U is still an unknown value, but the results of the heat transfer model are needed in the formula for U . This implies that there is a dependency between U and T_s . To solve this, an iterative procedure is used.

3.4.1 Equation for U

The equation to determine the speed of the interface is derived from the continuity equation through a similar procedure to how we determined the Knudsen layer jump conditions. We again assume that the vapor molecules behave according to the following distribution function,

$$f = \begin{cases} \rho_s (2\pi RT_s)^{-3/2} \exp \left[-\frac{\xi_x^2 + \xi_y^2 + \xi_z^2}{2RT_s} \right] & \xi_z > 0 \\ \beta \rho (2\pi RT)^{-3/2} \exp \left[-\frac{\xi_x^2 + \xi_y^2 + (\xi_z - u)^2}{2RT} \right] & \xi_z < 0 \end{cases}, \quad (3.48)$$

where T and ρ are the states of the vapor determined from the Knudsen layer model. By applying the method of moments to this distribution function and using the continuity equation, we get the following equation,

$$U = \sqrt{\frac{RT_s}{2\pi}} - \frac{\rho}{\rho_s} \sqrt{\frac{RT}{2\pi}} \beta(m) F^-(m), \quad (3.49)$$

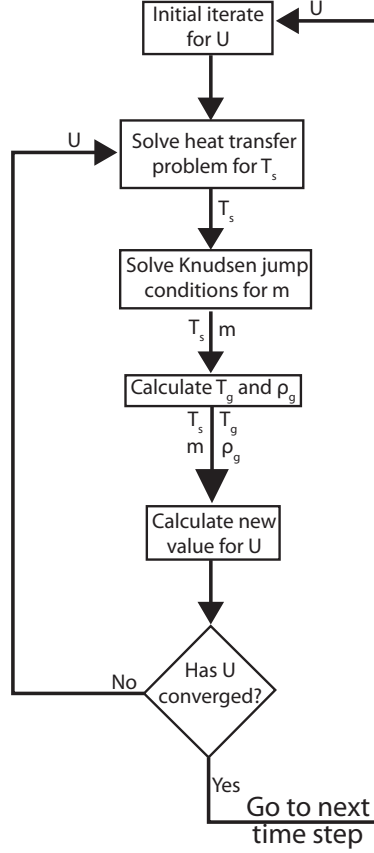


Figure 3.7: Flow of the model.

where $F^-(m)$ is defined by equation (3.38) and $\beta(m)$ is defined by equation (3.36). Notice that equation (3.49) requires information from both the heat transfer model and the Knudsen layer model.

3.4.2 Determining U by iteration

A dependency exists between U and the result of the heat transfer model T_s . We have a method for determining either of these values, should the other one be known. To determine both values, we must use an iterative method. More precisely, we treat the determination of U as a nonlinear function, and solve that function using a numerical solver.

We start by defining $\mathcal{F}(U)$ as the function which takes a value of U and returns an

updated value of U by the following procedure:

Step 1: Given a value for U and a temperature profile T^n , use the heat transfer model (3.13) and (3.17), to solve for the temperature profile at the next time step, T^{n+1} . Average T^{n+1} over the boundary of the hole to determine T_s .

Step 2: Use T_s as a parameter in the Knudsen layer model to compute m , ρ_v , T_v , and p_v .

Step 3: Use T_s , m and the state variables of the vapor in equation (3.49) to determine a new value for U .

Therefore, $\mathcal{F}(U)$ uses the entire model to update the value of U . To determine a value for U , we look for a fixed point of $\mathcal{F}(U)$. This is done by numerically solving the following equation,

$$\mathcal{F}(U) - U = 0 \quad (3.50)$$

using the secant method. Refer to Figure 3.7 to see the flow of the model over one time step.

3.5 Implementation of the Model

A finite difference method is implemented to solve the averaged heat equation in the heat transfer model. The standard second order finite difference discretization is used on the first and second spatial derivatives. When discretizing the temporal derivative a first order implicit-explicit method is used, resulting in the following time step formula,

$$T^{n+1} = (I - \alpha \Delta t D^2)^{-1} \left[T^n - \frac{4ss'}{R^2 - s^2} \left(D^1 T^n - \frac{\partial}{\partial z} T(s, z, t) \right) \right], \quad (3.51)$$

where $\alpha = \frac{k_s}{\rho_s c_s}$, Δt is the time step, T^n is a vector representing the temperature across the spatial nodes, and D^1 and D^2 are the discretization operators for the first and second derivatives respectively. We discretize the temporal derivative in this way for stability purposes. This allows us to choose a time step on the order of Δx as opposed to Δx^2 . The spatial domain, which is given in the z direction is set to 5×10^{-4} m, and the number of nodes used to discretize that domain is $N = 1000$. When calculating the value for T_s ,

we approximate the integral in the numerator of equation (3.18) using the midpoint rule, while the surface area of the hole is calculated analytically.

As stated in Section 3.3, the model of the Knudsen layer is solved by finding the solution to a scalar nonlinear equation for the dimensionless variable m . This is done with Newton's method. This iterative method for solving nonlinear equations is given by the following formula,

$$x^{n+1} = x^n - \frac{f(x^n)}{f'(x^n)}, \quad (3.52)$$

where x^n is the n^{th} iterate, and $f(x)$ is the nonlinear function being solved. The derivative of $f(x)$ was computed exactly using Maple. For termination criteria, an absolute error of $\epsilon = 10^{-7}$ is used, and the value of m at the previous time step is used for the initial iterate. We also must account for the fact that there is different equation for the subsonic and supersonic cases. Our procedure for dealing with this is to solve the subsonic equation if the Mach number $M < 1.5$. If the solution of that equation gives a Mach number greater than unity, we solve the supersonic equations. This allows us to switch well from subsonic to supersonic and vice versa.

To compute the speed of the solid vapor interface U , we find a fixed point to the function $\mathcal{F}(U)$ defined in section 3.4 by the previous steps in the model. Due to the fact that there is no analytical expression for $\mathcal{F}(U)$, we use the secant method to determine this fixed point. The secant method is a derivative free method for determining roots of a function. It is given by the following formula,

$$x^{n+1} = x^n - \frac{x^n - x^{n-1}}{f(x^n) - f(x^{n-1})} f(x^n). \quad (3.53)$$

This method is similar to Newton's method, in that it approximates the derivative with a finite difference between the previous two iterates. A relative error tolerance of $U_{TOL} = 10^{-8}$ is used. Due to the small time step, the value of U changes very little from one time step to the next, this means that the secant method converges in few iterations.

The final step to the implementation of this model is the parameter estimation. Recall from the heat transfer model, the radius of the top of the hole is given by,

$$R(t) = \kappa \xi(t), \quad (3.54)$$

with κ being a free parameter to be determined from experimental data. We have two pieces of experimental data to use for parameter estimation, the hole depth d_{exp} and the hole radius r_{exp} . The hole depth and radius resulting from the model and a parameter value of κ will be denoted $d_{mod}(\kappa)$ and $r_{mod}(\kappa)$ respectively. To perform the parameter estimation, we minimize the following cost functional,

$$J(\kappa) = \left(\frac{d_{mod}(\kappa) - d_{exp}}{d_{exp}} \right)^2 + \left(\frac{r_{mod}(\kappa) - r_{exp}}{r_{exp}} \right)^2. \quad (3.55)$$

We minimize $J(\kappa)$ using the Nelder-Mead method, a symplectic method for minimization, and it requires approximately 15 iterations for this method to converge.

3.6 Results

Following experiments done by our collaborators, led by Dr. Tu, we simulate drilling into a slab of 316 stainless steel. The parameters used to simulate this material are given in Table 3.2 [65].

Table 3.2: Material properties of 316 stainless steel and laser parameters; the "star values" are estimated from measured values for iron, the "dagger" values are estimated from 304 stainless steel [13].

density ρ	7500 kg/m ³	heat capacity c	630 J/kg K
melting temp. T_m	1400 °K	vaporization temp. T_v^*	3134 °K
thermal conductivity k	29 W/m K	latent heat of fusion L_f	2×10^5 J/kg
latent heat of vap. L_v^\dagger	7.6×10^6 J/kg	beam diameter	10 μ m

We obtained the temporal power profile of the laser from Dr. Tu's lab as shown in Figure 3.8(left). Recall that the laser has a spatial profile of a Gaussian curve, so Figure 3.8 shows the power of the laser at the peak of the Gaussian curve as a function of time. While this figure is available to us, the data is not, we therefore visually approximated the profile using the figure as a reference, see Figure 3.8(right). This approximate laser profile was used as input to the heat transfer model.

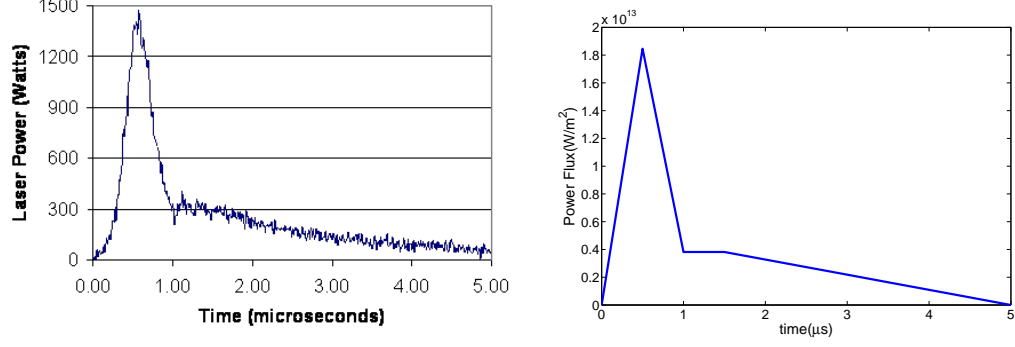


Figure 3.8: (Left) Profile of the peak laser power as a function of time. (Right) Approximate power profile used in computations.

We were able to obtain many results from this model. All the results are given for three cases, depending on the assumed shape of the hole. The cone ($\ell = 1$) and paraboloid ($\ell = 2$) models are shown, as well as a hole with constant radius ($\ell \rightarrow \infty$), which corresponds to a purely one-dimensional heat transfer model. Figure 3.9 shows the temperature at the hole interface, T_s , as a function of time. Notice that the one-dimensional model fails to capture the initial spike in temperature that the other models attain. A time profile of the speed at which the hole is being drilled, U , is shown in Figure 3.10. Again, a spike in the speed is captured by the parabolic and conical models that is missed by the one-dimensional model.

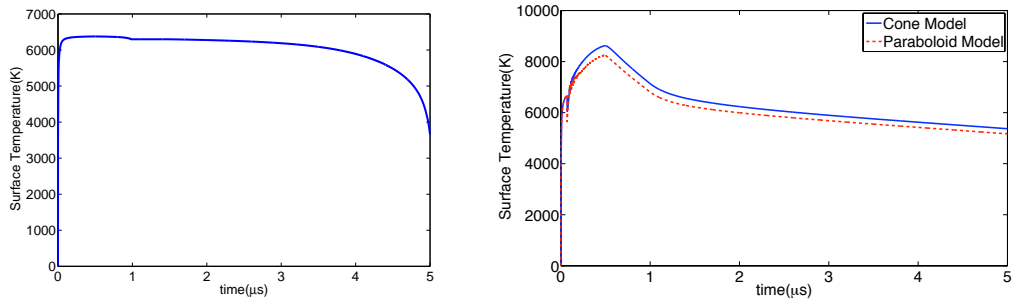


Figure 3.9: Average surface temperature of the dense material as a function of time for the three different hole types.

Table 3.3: Experimental and numerical results.

	Hole Depth	Hole Radius
Experimental Data	185 μm	11.5 μm
One-d. profile ($\ell \rightarrow \infty$)	80 μm	
Conical profile ($\ell = 1$)	109.52 μm	7.31 μm
Parabolic profile ($\ell = 2$)	82.4 μm	7.05 μm

We are able to obtain other data from our model, such as the vapor pressure and temperature as functions of time, however, this data is not helpful to us since we have nothing to compare it against. Due to the violent and rapid nature of the laser drilling process, it is not possible to get dynamic data experimentally. There is no accurate method of reading the state of the gas or solid during the drilling procedure. Given this, the only experimental data we have to validate our model is the hole depth and radius, as this can be determined after the drilling is finished. This data is obtained from Dr. Tu's laboratory, by finely grinding the material until the hole is reached. A measurement of the hole depth and radius can then be taken by looking at the profile. While this method is delicate, it is still much more accurate than any other data from the drilling process. Table 3.3 shows the experimental results as well as the results of our model for the hole depth and top radius.

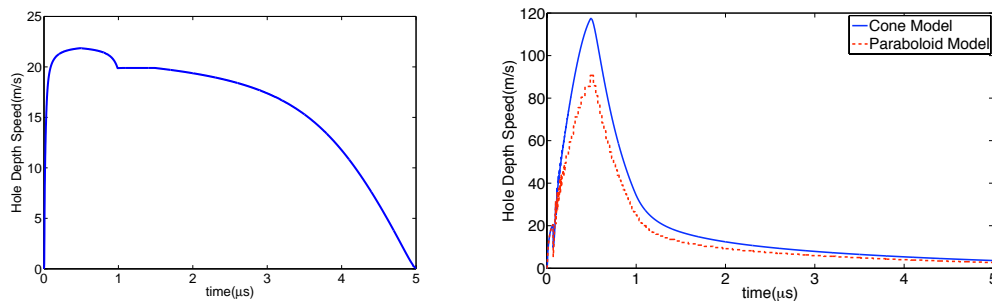


Figure 3.10: Velocity of drilling as a function of time for the three different hole types.

Finally, we consider how our results vary when the power profile is changed. This

Table 3.4: Results due to varying power profiles.

	CONE		PARABOLOID	
Pulse Length	Hole Depth	Hole Top Radius	Hole Depth	Hole Top Radius
Normal Pulse	109.52 μm	7.31 μm	82.4 μm	7.05 μm
1 μs	111.13 μm	7.41 μm	83.78 μm	7.17 μm
2 μs	113.6 μm	7.57 μm	85.92 μm	7.35 μm
3 μs	115.1 μm	7.67 μm	87.25 μm	7.46 μm
4 μs	115.6 μm	7.71 μm	87.73 μm	7.51 μm

was done experimentally by our collaborator Dr. Tu, by increasing the length of the tail in the power profile, that is the portion of the profile that stays at approximately 300 W. Whereas the tail in the profile shown in Figure 3.8 lasts for about .5 μs , we increase it to go to 1, 2, 3, and 4 μs . The same value of κ that was determined earlier is used in these calculations as well. Table 3.4 shows the results of this trial. We see that as the tail is increased, the depth does not change significantly. This is in direct contrast to the experimental results, where the depth increases significantly as the profile tail increases. The reason for this discrepancy is that melt ejection is not taken into account in our model. After the initial spike, the removal of material is due mainly to melt ejection, therefore our simulation would not model this extra removal.

3.7 Conclusions

The model we have created for laser drilling is relatively inexpensive. The computation of the heat transfer problem is one-dimensional, and solving for the states of the vapor is reduced to solving a nonlinear scalar equation. While the iterative method used to calculate U requires the model to be run several time per time step, it is still less computationally intensive than a two-dimensional model. Neglecting the effects of melt ejection limits the ability of our method to accurately approximate the experimental data. In [88] we see laser drilling in a similar power regime. There it is shown that evaporation accounts for approximately 50-60% of the hole depth. We see that this agrees with the results from our model. Therefore, our results approximate the evaporation of the experimental data. This model could be improved by incorporating melt ejection in a way

that does not increase the computational cost significantly.

Chapter 4

Transport on Networks

4.1 Introduction

A network consists of a set of objects that are related to each other. The objects are called vertices or nodes, and the relations between the objects are called edges, see Figure 4.1. This general definition gives a mathematical model for many situations. There are numerous examples of networks. Some of the first real-world networks to be studied were social networks [7, 62, 66, 80]. The vertices of a social network are people or groups of people, and the edges represent connections or interactions between those people. Computer networks such as the Internet show the physical connection between computers. Information networks, such as the World Wide Web, show how sets of data are linked to each other [38]. Technological networks are usually man-made networks used

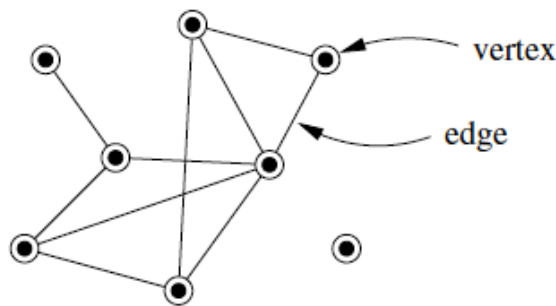


Figure 4.1: A sample network [68].

to transport material or information. Examples of this type of network include roads [31, 37], railways [49], electric power grids [89], and gas pipes [4, 15, 16]. Technological networks can also include naturally made phenomenon such as rivers [25, 63] or blood vessels. Many interesting phenomenon can be classified under biological networks. This would include a food web, a network of metabolic pathways, or protein interactions. Neural networks and vascular network are also examples [68].

A network is also called a graph in mathematical terms. A formal definition is given here.

Definition 3. A **graph** is a pair $\mathcal{G} = (V, E)$, such that $E \subseteq V \times V$. Thus, each element of E is related to two elements of V . Elements of V are called **vertices** or **nodes**, and elements of E are called **edges** [24].

The mathematical theory of graphs has been well studied, dating back to Euler's solution of the Königsberg bridge problem in 1735 [68]. The rich mathematical theory of graphs is helpful for applied problems such as social networks or information networks. Two other definitions are useful when describing properties of networks and problems defined on them [72].

Definition 4. The **restriction** $\mathcal{G}|_v$ of a graph \mathcal{G} to the vertex v is defined by,

$$\mathcal{G}|_v = \{e \in E | e = (w, v) \text{ or } e = (v, w)\}. \quad (4.1)$$

This is the set of all edges connected to the vertex v .

Definition 5. The **index** $\mathcal{G}(v)$ of a vertex v is defined by,

$$\mathcal{G}(v) = |\mathcal{G}|_v|. \quad (4.2)$$

That is, the index of v is equal to the number of edges that are connected to v in the graph.

Recently, due to the invention of computers and rapid, global communication, increasingly larger networks have been considered. This has shifted the focus on networks from classical graph theory toward a statistical viewpoint. With networks whose number of vertices are on the order of millions or billions, see Figure 4.2, the importance of a particular vertex or edge has diminished. Another aspect of networks involves the

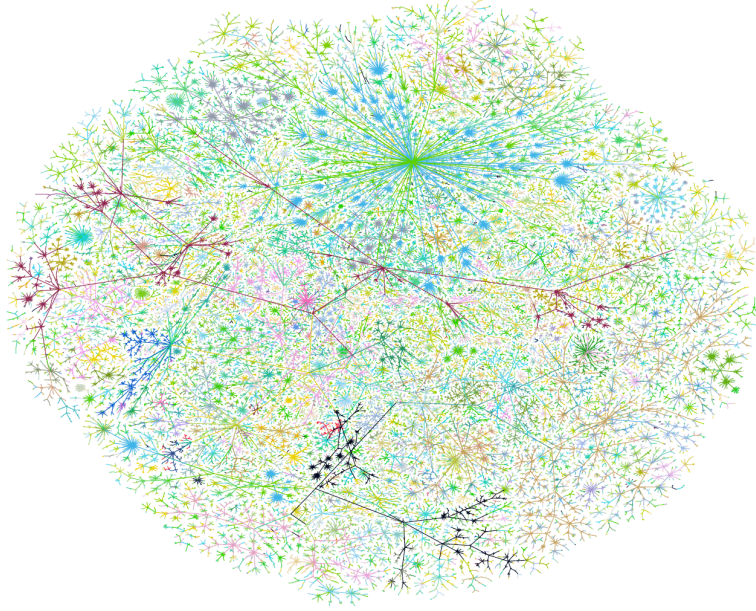


Figure 4.2: Visualization of a portion of the Internet network. Example of a network that is on the upper limit of what is useful to visualize [68].

visualization of them. For smaller networks, much could be learned by drawing them and using the human eye. As network size increase, this becomes impractical. Therefore research is done to examine large networks to determine mathematically what the eye determines naturally [68].

In this work, we consider a particular class of network, one in which material is transported between the vertices. The transport is modeled by a differential equation defined on the edges of the network. When modeling the transport of material, the physics of the problem is certainly multi-dimensional and so the differential equations can also be multi-dimensional. However, the benefit of using a network is to define the edges to represent the portions of the domain that can be well approximated by a one-dimensional equation. The nodes represent the regions of the domain that can not be well approximated in one dimension. When modeling with a network, it is advantageous for the node regions to be small compared with the regions represented by the edges. This can be visualized by considering a network of pipes transporting gas. Along the portions of the network where the pipe runs straight, represented by edges, the gas flow can be modeled by one-dimensional equations. When the pipe geometry changes, by a

bend or split into multiple pipes, these regions would be represented by nodes.

We define the edges of a network to be one-dimensional smooth manifolds in \mathbb{R}^2 or \mathbb{R}^3 (that is curves), and the vertices to be points in the above spaces. The transport is approximated along the edges by one-dimensional differential equations. At the nodes we enforce algebraic conditions that model the multi-dimensional effects. These conditions are called junction conditions, and the vertices will sometimes be called junctions. The junction conditions couple the differential equations defined on the edges. The physics of the material being transported is important when deriving the junction conditions. As in the example of gas flow, the physics of gas flowing through a bend in pipe will determine what junction conditions are implemented. Because of this, determination of junction conditions often offer challenging modeling questions.

The subclass of transport networks we consider are ones where the differential equations defined on the edges are hyperbolic. There are two particular areas of hyperbolic network problems that we study. First, in Chapter 5, we apply the domain decomposition method to linear hyperbolic network problems. This is done to determine if such a solver is beneficial. An *a priori* estimate of the number of iterations needed for convergence is given and compared to numerical experiments. The second area we considered was gas flow through a pipe junction. This can be considered as a two-edge network problem, and as a smaller part of a larger network of gas pipes. These two areas consider the numerical and computational side of network problems, as opposed to the theoretic side considered in much of the previous work.

4.1.1 Previous work

Research on networks began in the 1930's with social networks. These show relationships between people or groups of people. Examples of these relationships include friendship, sexual contact, exchange of emails, and cooperation toward a certain goal. The Internet and World Wide Web are networks of particular importance, and are interesting areas of research. Other information networks such as those representing paper citations have been studied. Many biological networks have also been considered, such as metabolic networks or protein interaction networks. Networks of neural pathways have also been studied [68].

In [2] we see air traffic routes, electric power grids, and the neuronal network of the worm *C. elegans* all represented as networks and their statistical properties analyzed.

In [69], the spread of potential along a tree of dendrites is modeled. The structure of a sexual network of adolescents is described in [7], and in [49] the Boston subway is represented by a network.

Networks can also be used to represent dynamical systems and study their behavior. In [57] we see a system of lasers coupled together in a ring and the stability of the system is determined under certain conditions. A particular class of electrical circuits is studied in [90]. In [56], epidemiology models are discussed, as well as the effect of social and geographical variables on the rate of disease transmission.

The majority of network research involves determining properties of the network. These include determining if the network is “small world”, that is, is it possible to travel from one vertex to another by using few edges relative to the size of the network. Another property involves determining how clustered the network is, and analyzing where those clusters are located. The relative importance of particular vertices and edges have been studied as well. These network properties have been studied both on abstract networks, and to gain greater insight to application represented by networks [68].

Research on transport networks are generally concerned with determining accurate and simple junction conditions to model the physics involved at the vertices. A vascular network is modeled in [22, 23], in particular the Circle of Willis. Traffic models are studied in [31, 37] where junction conditions are defined to maximize the flow of cars through an intersection. Gas flow through a network of pipes is also well studied. In [5, 6, 20] we see models for flow through an engine manifold, where network models are helpful in testing engine designs.

While much research has been done regarding networks, there is surprisingly little literature about numerical implementation of transport network models. Much of the work involves well-posedness of the problem or derivation of junction conditions. Where numerical methods are employed, the work is not viewed from a mathematical standpoint, and so little discussion is given to the methods used. In this work we implement various numerical methods on transport network problems. The effectiveness of these methods is discussed as well as their accuracy in approximating the multi-dimensional physics.

4.2 Linear Transport Problems

We begin our study with linear transport problems. Given a network $\mathcal{G} = (V, E)$, along each edge $e_i \in E$, we define the following linear hyperbolic equation,

$$\frac{\partial}{\partial t} \mathbf{q}_{e_i}(x, t) + A_{e_i} \frac{\partial}{\partial x} \mathbf{q}_{e_i}(x, t) = 0 \quad x \in (a_{e_i}, b_{e_i}), \quad t > 0, \quad (4.3)$$

where $\mathbf{q}_{e_i} \in \mathbb{R}^n$ are the state variables, and $A_{e_i} \in \mathbb{R}^{n \times n}$ is a constant diagonalizable matrix with real distinct eigenvalues, making (4.3) strictly hyperbolic. Each edge is parameterized so that a_{e_i} and b_{e_i} represent the two endpoints of edge e_i . We need at each vertex $v \in V$, a sufficient number of junction conditions. That number depends on the hyperbolic equation, as well as the index of the vertex v . Here we assume the junction conditions are linear in the state variables.

4.2.1 Junction Conditions

The junction conditions are what relate the edges of a network to each other, and couple the differential equations defined on each edge. In general, this can be challenging, as the number and form of the conditions depends not only on the problem, but also on the index of a vertex, that is the number of edges incident upon it. In Chapters 6 and 7, we discuss junction conditions for nonlinear problems.

Let us consider linear junction conditions at a vertex v of index M ,

$$J \begin{bmatrix} \mathbf{q}_{\hat{e}_1} \\ \mathbf{q}_{\hat{e}_2} \\ \vdots \\ \mathbf{q}_{\hat{e}_M} \end{bmatrix} = 0 \quad \hat{e}_i \in \mathcal{G}|_v \quad (4.4)$$

where $J \in \mathbb{R}^{P \times nM}$ is a constant matrix. Equation (4.4) gives P equations relating the state variables \mathbf{q}_{e_i} along all edges connected to vertex v to each other. Since our problem is hyperbolic, we know that not all the variables should be set on every boundary. For some variables we use the characteristic lines to determine them from the previous time step.

Since (4.3) is strictly hyperbolic we can write,

$$A_{\hat{e}_i} = R_{\hat{e}_i} \Lambda_{\hat{e}_i} R_{\hat{e}_i}^{-1}, \quad (4.5)$$

and define the characteristic variable as in (2.20). We convert (4.4) into characteristic variables,

$$0 = J \begin{bmatrix} R_{\hat{e}_1} \mathbf{w}_{\hat{e}_1} \\ R_{\hat{e}_2} \mathbf{w}_{\hat{e}_2} \\ \vdots \\ R_{\hat{e}_M} \mathbf{w}_{\hat{e}_M} \end{bmatrix} = J \operatorname{diag}(R_{\hat{e}_1}, R_{\hat{e}_2}, \dots, R_{\hat{e}_M}) \begin{bmatrix} \mathbf{w}_{\hat{e}_1} \\ \mathbf{w}_{\hat{e}_2} \\ \vdots \\ \mathbf{w}_{\hat{e}_M} \end{bmatrix} = B \begin{bmatrix} \mathbf{w}_{\hat{e}_1} \\ \mathbf{w}_{\hat{e}_2} \\ \vdots \\ \mathbf{w}_{\hat{e}_M} \end{bmatrix}, \quad (4.6)$$

where,

$$B = J \operatorname{diag}(R_{\hat{e}_1}, R_{\hat{e}_2}, \dots, R_{\hat{e}_M}). \quad (4.7)$$

Letting $\mathbf{w}^{(k)}$ denote all the characteristic variables that are determined from the previous time step, and $\mathbf{w}^{(u)}$ denote all unknown characteristics that are set by the junction conditions. By reordering the variables and the corresponding columns of B we get,

$$0 = \tilde{B} \begin{bmatrix} \mathbf{w}^{(k)} \\ \mathbf{w}^{(u)} \end{bmatrix} = \begin{bmatrix} \tilde{B}^{(k)} & \tilde{B}^{(u)} \end{bmatrix} \begin{bmatrix} \mathbf{w}^{(k)} \\ \mathbf{w}^{(u)} \end{bmatrix} = \tilde{B}^{(k)} \mathbf{w}^{(k)} + \tilde{B}^{(u)} \mathbf{w}^{(u)}, \quad (4.8)$$

where $\tilde{B}^{(k)}$ and $\tilde{B}^{(u)}$ are partitions of \tilde{B} such that the multiplication makes sense. Isolating the unknown variables in (4.8),

$$\tilde{B}^{(u)} \mathbf{w}^{(u)} = -\tilde{B}^{(k)} \mathbf{w}^{(k)}. \quad (4.9)$$

Equation (4.9) can be solved for the unknown characteristic variables.

We note two things about junction conditions for linear problems. First, the number of conditions that can be imposed, P , is determined by the characteristic structure of the edges at the vertex. Second, the value of P can differ between vertices. These two facts can make it very difficult to define junction conditions that apply to a general network, even for linear problems. Below we give an example of a linear problem for which it is possible to define junction conditions.

4.2.2 Numerical Procedure for Network Problems

It is worth mentioning briefly the general method used to solve such problems numerically. To update our solution by one time step Δt , we start by updating each edge using a well-known numerical method for one-dimensional hyperbolic equations. This step is no different from solving over any one-dimensional domain. Next, we determine the boundary values of each edge using the junction conditions. This is not a trivial procedure, as seen below, but once the boundary values are determined, they are assigned to the appropriate edges. This procedure is then repeated up to some final time T .

4.2.3 Linear Acoustics Equations

Consider a particular network problem where the linear acoustics equations are defined along each edge. This particular problem is chosen because it is possible to define junction conditions that will apply to any network, as there is one positive and one negative eigenvalue.

The linear acoustics equations along edge e_i are given by [55], p. 26-31,

$$\frac{\partial}{\partial t} \begin{bmatrix} p_{e_i} \\ u_{e_i} \end{bmatrix} + \begin{pmatrix} 0 & K_{e_i} \\ 1/\rho_{e_i} & 0 \end{pmatrix} \frac{\partial}{\partial x} \begin{bmatrix} p_{e_i} \\ u_{e_i} \end{bmatrix} = 0 \quad x \in (0, 1), t > 0 \quad (4.10)$$

$$p_{e_i}(x, 0) = \dot{p}_{e_i}(x) \quad x \in [0, 1] \quad (4.11)$$

$$u_{e_i}(x, 0) = \dot{u}_{e_i}(x) \quad x \in [0, 1] \quad (4.12)$$

where ρ_{e_i} is a parameter describing the average density, and K_{e_i} is another parameter that depends on ρ_{e_i} . The variables p_{e_i} and u_{e_i} are the pressure and velocity on edge e_i , respectively and their initial values are given by $\dot{p}_{e_i}(x)$ and $\dot{u}_{e_i}(x)$. Note that each edge is parameterized by the unit interval.

These are the linearized equations of the isentropic gas dynamics equations. They are linearized about a density $\rho = \rho_{e_i}$ and velocity $u_{e_i} = 0$. They also correspond to the linear wave equation in system form. Examining the coefficient matrix,

$$A_{e_i} = \begin{bmatrix} 0 & K_{e_i} \\ 1/\rho_{e_i} & 0 \end{bmatrix}, \quad (4.13)$$

we see that it has the following eigenvalues,

$$\lambda_1 = -c_{e_i} \quad \lambda_2 = c_{e_i} \quad (4.14)$$

where $c_{e_i} = \sqrt{K_{e_i}/\rho_{e_i}}$ is the speed of sound. Since these are real and distinct we know that equation (4.10) is a strictly hyperbolic problem. Associated with these we have the following eigenvectors,

$$r_1 = \begin{bmatrix} -Z_{e_i} \\ 1 \end{bmatrix} \quad r_2 = \begin{bmatrix} Z_{e_i} \\ 1 \end{bmatrix} \quad (4.15)$$

where $Z_{e_i} = \rho_{e_i} c_{e_i}$ is the impedance.

4.2.4 Junction Conditions for the Linear Acoustics Equations

The junction conditions for the acoustics equations are given from physical considerations. Since there is one positive and one negative eigenvalue on each edge, we know that we will require $\mathcal{G}(v)$ conditions at each vertex v . The first condition is that the pressure p must be continuous from each edge to another across a junction,

$$p_{e_1} = p_{e_i} \quad \forall \ e_i \in \mathcal{G}|_v \setminus \{e_1\} \quad (4.16)$$

The second condition is that momentum must be conserved across a junction, that is the momentum coming into the junction must equal the momentum leaving the junction. There are two ways of writing this condition, depending on how we define the incoming and outgoing edges. In the first definition, we view incoming edges as edges where the fluid is traveling towards v , that is the velocity vector points towards the vertex. Similarly, an outgoing edge would have the velocity vector pointing away from v . The set of incoming and outgoing edges to v under this definition is denoted $I_p(v)$ and $O_p(v)$ respectively. Under this definition, conservation of momentum is written,

$$\sum_{e_i \in I_p(v)} |u_{e_i}| = \sum_{e_j \in O_p(v)} |u_{e_j}|. \quad (4.17)$$

The second way of defining the edges depends on the parameterization assigned to each edge. When solving numerically, it is necessary to assign a parameterization to each

edge. In order to work with a parameterized edge, we introduce the following definition,

Definition 6. Given an edge e_i that is parameterized over the interval (a_{e_i}, b_{e_i}) , we denote by $\mathbf{e}_i(-\infty)$ the vertex at a_{e_i} , and we denote by $\mathbf{e}_i(\infty)$ the vertex at b_{e_i} .

Using this definition, the incoming and outgoing edges are defined by,

$$I_c(v) = \{e_i | e_i(\infty) = v\} \quad (4.18)$$

$$O_c(v) = \{e_i | e_i(-\infty) = v\}. \quad (4.19)$$

Under this definition, conservation of momentum becomes,

$$\sum_{e_i \in I_c(v)} u_{e_i} = \sum_{e_j \in O_c(v)} u_{e_j}. \quad (4.20)$$

It can be shown that the two conditions are equivalent. Let us start with the parameterization definition,

$$\begin{aligned} \sum_{e_i \in I_c(v)} u_{e_i} &= \sum_{e_j \in O_c(v)} u_{e_j} \\ \Rightarrow \sum_{e_i \in I_c^+(v)} |u_{e_i}| - \sum_{e_i \in I_c^-(v)} |u_{e_i}| &= \sum_{e_i \in O_c^+(v)} |u_{e_i}| - \sum_{e_i \in O_c^-(v)} |u_{e_i}| \\ \Rightarrow \sum_{e_i \in I_c^+(v)} |u_{e_i}| + \sum_{e_i \in O_c^-(v)} |u_{e_i}| &= \sum_{e_i \in O_c^+(v)} |u_{e_i}| + \sum_{e_i \in I_c^-(v)} |u_{e_i}| \\ \Rightarrow \sum_{e_i \in I_p(v)} |u_{e_i}| &= \sum_{e_i \in O_p(v)} |u_{e_i}|, \end{aligned}$$

where the superscripts $+$ and $-$ represent the subset of edges where the velocity is positive and negative respectively. Since these two definitions are equivalent, we use the parameterization definition as it is easier to implement numerically.

Finally, we notice that Equations (4.16) and (4.20) give exactly $\mathcal{G}(v)$ conditions at each vertex v , so that the system for solving the junction conditions is well-determined. Since there is one positive and one negative eigenvalue, the parameterization we choose for the network will not affect the number of unknowns at each junction, this is why this problem is ideal for solving over a network.

Chapter 5

Domain Decomposition Applied to Network Problems

5.1 Introduction

The domain decomposition method is an iterative method used to solve differential equations by splitting a domain into smaller subdomains. Assume that we are given a domain $\Omega = \Omega_1 \cup \Omega_2$, as seen in Figure 5.1, and we wish to find a function u such that,

$$Lu = f \quad \text{in } \Omega \quad (5.1)$$

$$u = 0 \quad \text{on } \partial\Omega \quad (5.2)$$

where L is a differential operator and $\partial\Omega$ is the boundary of Ω . We assume Dirichlet boundary conditions for simplicity, but general conditions can be assumed as well. The domain decomposition method works by finding solutions u_i to (5.1) on Ω_i separately. However, when finding these solutions, boundary conditions must be imposed upon the artificial boundary Γ_i created by splitting the domain. It is here where the iterative properties of the method are used. The boundary conditions imposed upon the artificial boundary come from the previous iterate of the other subdomain. We note that it is possible for the subdomains to be overlapping, in which case there exists two artificial boundaries [73].

To state this more formally, we begin the iterative procedure by assuming an initial iterate $u_i^{(0)}$ for the solution to the two subdomain problems. Then, for $n = 1, 2, 3, \dots$, we

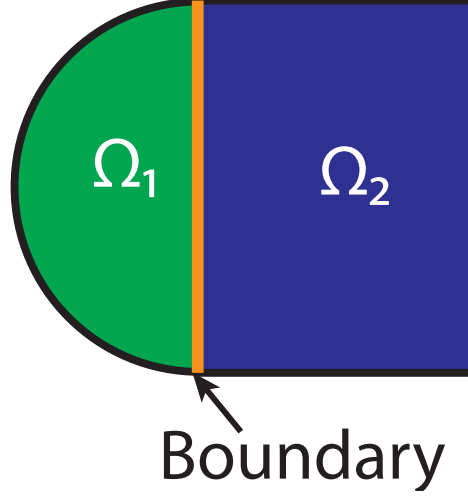


Figure 5.1: General domain split into two subdomains.

find a function $u_i^{(n)}$ that solves the following boundary value problems,

$$Lu_1^{(n)} = f \quad \text{in } \Omega_1 \quad (5.3)$$

$$u_1^{(n)} = 0 \quad \text{in } \partial\Omega_1 \setminus \Gamma_1 \quad (5.4)$$

$$u_1^{(n)} = u_2^{(n-1)} \quad \text{on } \Gamma_1 \quad (5.5)$$

$$Lu_2^{(n)} = f \quad \text{in } \Omega_2 \quad (5.6)$$

$$u_2^{(n)} = 0 \quad \text{in } \partial\Omega_2 \setminus \Gamma_2 \quad (5.7)$$

$$u_2^{(n)} = u_1^{(n-1)} \quad \text{in } \Gamma_2 \quad (5.8)$$

where the artificial boundaries are $\Gamma_1 = \partial\Omega_1 \cap \Omega_2$, $\Gamma_2 = \partial\Omega_2 \cap \Omega_1$. This algorithm is repeated until some termination criterion is reached, usually involving small change from one iteration to the next. The procedure listed above is a Jacobi-like iteration, in that only information from the previous iterate is used. This can be modified in a Gauss-Siedel fashion, so that as a solution is computed, its boundary data will be used for the other subdomain. There are other modifications that have been used to speed up convergence or obtain other desired results; see [73, 83] and references therein.

There are many benefits to using domain decomposition. As seen in Figure 5.1, it

can make dealing with complicated geometries easier. One of the main benefits is the ability to use different methods or discretizations on different parts of the domain. Finally, splitting a problem into smaller subproblems lends itself very well to parallelization. Note that (5.1), the example differential problem used above, was a boundary value problem as opposed to an initial boundary value problem. This is because much of the work done with the domain decomposition method is on elliptic problems with no time-dependence. Domain decomposition methods on these types of problems are well-known and many convergence results have been proved for them; see [73, 83, 91].

When applying the domain decomposition method to time-dependent problems, there are in general two approaches. These approaches differ in when they partition the domain. The first approach applies the temporal discretization, usually with an implicit discretization, and then solves the purely spatial problem remaining at each time step with domain decomposition [58]. An advantage of domain decomposition that is hindered by this approach is parallelization. Since boundary data has to be transferred across subdomains at each time step, many small packets of information must be communicated. There is inherent overhead involved in data transmission independent of the size of the data. Therefore transmission of many small packets takes longer than transmission of one large packet [29].

The second approach partitions the spatial domain first, and then applies the temporal discretization to each subdomain. Each subdomain is then solved to final time T separately, and then boundary data is shared to adjoining subdomains. Therefore communication is only needed after each processor has calculated a solution to final time, instead of at each time step.

As mentioned, much of the research done on domain decomposition has been with elliptic problems on two-dimensional domains. Little work has been done applying it to hyperbolic network problems. In [48, 53, 54], a method called the dynamic domain decomposition method is applied to solve optimal control problems for a network of elastic strings. This is the implementation of the second approach of domain decomposition for time dependent problems listed above. In [28, 29], the domain decomposition method is applied to the one-dimensional wave equation. In this case the subdomains are subintervals. This can be considered a network problem with the network being many edges joined end to end. Junction conditions were developed and calculations were done to determine the number of iterations necessary for convergence. In this work we extend this idea to networks of a more general type.

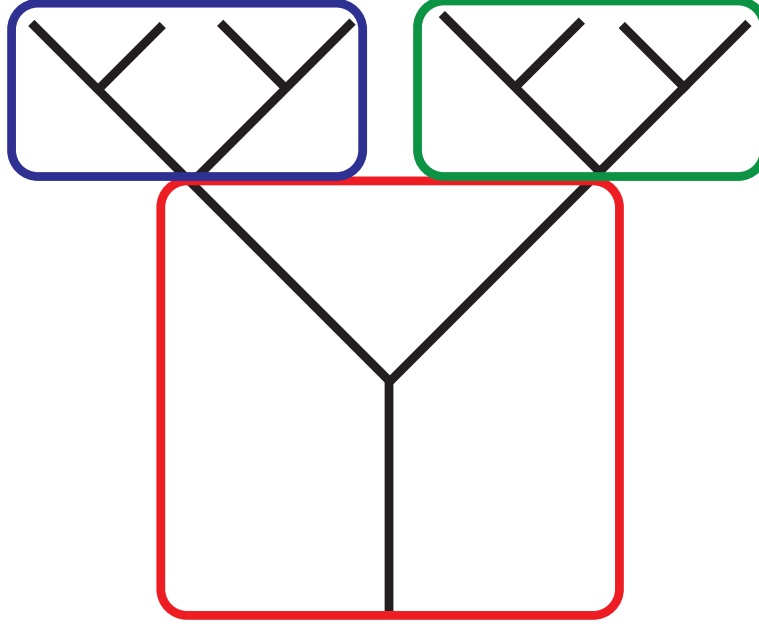


Figure 5.2: A network partitioned into subdomains for application of the domain decomposition method.

5.1.1 Current Work

In this work we consider the domain decomposition method applied to network problems solving the linear acoustics equations on each edge. When considering network problems we decompose the network into connected subnetworks, as in Figure 5.2. We implement the method using the second approach discussed above, that is to partition into subdomains before discretizing in time. The boundary conditions at each junction are determined as described above in Chapter 4. For some simple example problems we will also consider the advection equation, which will have continuity as junction conditions.

We first consider the convergence properties of the domain decomposition method on such problems. We examine the problem and determine intuitively how the method converges. Once this is done, we use this intuition to describe more formally the change of error in the solution from one iteration to the next. All this is done to obtain an estimate on the number of iterations needed for the method to converge for a particular problem. This convergence analysis is done neglecting numerical error. We show that this iteration estimate can be determined analytically for certain problems, and must be

determined computationally for others. This estimate can be used *a priori* to determine the amount of computational time required for the method to converge. This can help to decide if a parallelized version of domain decomposition is faster than solving the problem without domain decomposition.

5.2 Convergence Analysis

Given a network $\mathcal{G} = (V, E)$ and a set of linear hyperbolic differential equations defined on each edge, as described in Chapter 4, we define the following algorithm as the domain decomposition method for network problems.

1. Define an initial iterate for the solution,

$$\mathbf{q}_{e_i}^0(x, t) = \mathbf{h}_{e_i}(x, t) \quad e_i \in E, x \in (a_{e_i}, b_{e_i}), 0 < t < T \quad (5.9)$$

where $[a_{e_i}, b_{e_i}]$ denotes the coordinate system applied to edge e_i . Note that the initial iterate must be defined for all time $t < T$, for some final time T .

2. Partition the network into M connected subgraphs \mathcal{H}_j ,

$$\mathcal{G} = \mathcal{H}_1 \cup \mathcal{H}_2 \cup \dots \cup \mathcal{H}_M \quad (5.10)$$

$$\mathcal{H}_j = (V_j, E_j) \quad \forall j = 1, \dots, M \quad (5.11)$$

$$(5.12)$$

3. For each subgraph \mathcal{H}_j , solve the edges $i \in \mathcal{H}_j$ to final time $t = T$,

$$\frac{\partial}{\partial t} \mathbf{q}_{e_i}^k + A_{e_i} \frac{\partial}{\partial x} \mathbf{q}_{e_i}^k = 0 \quad e_i \in \mathcal{H}_j, x \in (a_{e_i}, b_{e_i}), \quad 0 < t < T \quad (5.13)$$

$$J_v \begin{bmatrix} \mathbf{q}_{\hat{e}_1}^k \\ \vdots \\ \mathbf{q}_{\hat{e}_L}^k \\ \mathbf{q}_{\tilde{e}_1}^{k-1} \\ \vdots \\ \mathbf{q}_{\tilde{e}_N}^{k-1} \end{bmatrix} = 0 \quad \hat{e}_\ell \in \mathcal{G}|_v \cap \mathcal{H}_j, \tilde{e}_\ell \in \mathcal{G}|_v \setminus \mathcal{H}_j \quad (5.14)$$

$$K_w \begin{bmatrix} \mathbf{q}_{\hat{e}_1}^k \\ \vdots \\ \mathbf{q}_{\hat{e}_L}^k \\ \mathbf{q}_{\tilde{e}_1}^{k-1} \\ \vdots \\ \mathbf{q}_{\tilde{e}_N}^{k-1} \end{bmatrix} = 0 \quad \hat{e}_\ell \in \mathcal{G}|_w \cap \mathcal{H}_j, \tilde{e}_\ell \in \mathcal{G}|_w \setminus \mathcal{H}_j \quad (5.15)$$

where v and w are the vertices of edge e_i associated with the points a_{e_i} and b_{e_i} respectively. The matrices J_v and K_w represent the junction conditions at the two ends of edge e_i . We see that they relate edges within the subgraph \mathcal{H}_j at the current iterate k , with edges outside of \mathcal{H}_j at the previous iterate $k - 1$.

4. Repeat until solution converges in some meaningful way.

We first consider a simplified scalar version of the problem on a small network, to gain an intuition of how the method converges from one iteration to the next. This is then formalized using convergence variables, a way of defining how far the solution has converged at the k^{th} iteration. Finally we generalize this to systems of equations so we can apply it to the linear acoustics equations.

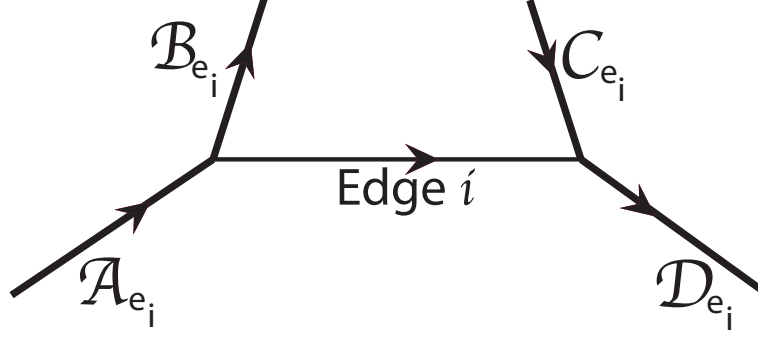


Figure 5.3: Notation used to describe various types of edges connected to edge i .

Let us consider a particular edge $e_i \in E$. Recall Definition 6 which labels the two vertices of an edge e_i . This is used to define the following sets,

$$\mathcal{A}_{e_i} = \{e_j \in E | e_j(\infty) = e_i(-\infty)\} \quad (5.16)$$

$$\mathcal{B}_{e_i} = \{e_j \in E | e_j(-\infty) = e_i(-\infty)\} \quad (5.17)$$

$$\mathcal{C}_{e_i} = \{e_j \in E | e_j(\infty) = e_i(\infty)\} \quad (5.18)$$

$$\mathcal{D}_{e_i} = \{e_j \in E | e_j(-\infty) = e_i(\infty)\} \quad (5.19)$$

such that the union of all four sets is equal to all edges adjacent to e_i . These sets describe the incoming and outgoing edges to e_i according to the parameterization chosen. The sets can be seen in Figure 5.3.

5.2.1 Domain Decomposition Convergence

The simplest nontrivial network is a two-edge loop network shown in Figure 5.4. The edges are defined to have unit length and along each edge we solve the advection equation with unit speed,

$$\frac{\partial}{\partial t} u_{e_i} + \frac{\partial}{\partial x} u_{e_i} = 0 \quad e_i = 1, 2, \quad x \in (0, 1), \quad 0 < t < T. \quad (5.20)$$

Note that both edges have the same length. We also know from the properties of hyperbolic problems, that each edge will only take boundary data from the left boundary, due to the positive speed of propagation. This will be important when considering the

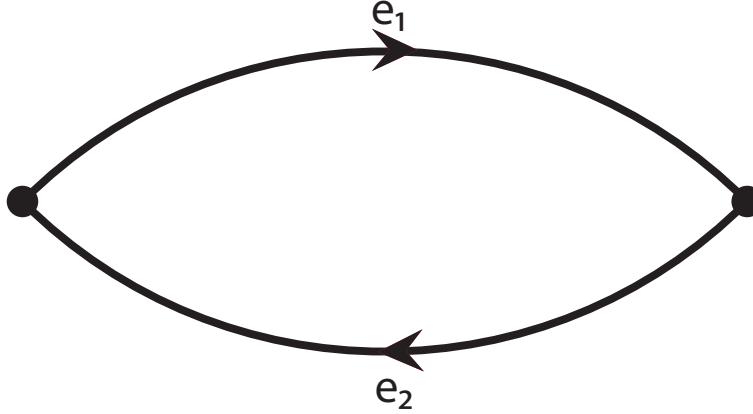


Figure 5.4: A simple two edge loop network.

convergence. Finally, we partition the loop network into two subdomains, with one edge assigned to each subdomain.

When considering the convergence of this problem and every problem hereafter, we make two assumptions. First we assume that the initial iterate of the domain decomposition method is not the solution, that is some error exists for all space and time. Second, we assume that given exact initial and boundary conditions, we obtain the exact solution. Another way of putting this is that we neglect numerical error. This is obviously a problematic assumption, however it is useful in determining the convergence properties of the domain decomposition method itself, without regard to the numerical solver. These two assumptions say that the only error introduced to the system is the error from the initial iterate. Therefore, convergence of the method will involve removing this error as the iterations progress.

To show the convergence, we illustrate the error in the spatio-temporal domain of each edge, using x - t plots. We show how this error decreases from one iteration to the next, under the assumptions made above. First we have the initial iterate, $k = 0$, which has error for all space and time. Next we consider the first iterate, $k = 1$. We note once again that the only place error can be introduced to this iteration is through the boundary from the previous iterate. Since boundary data can only be taken on the left boundary, error will enter in at time $t > 0$ and propagate with finite speed as seen in Figure 5.5.

Note that due to the finite speed of propagation of the error, there exists an interval of

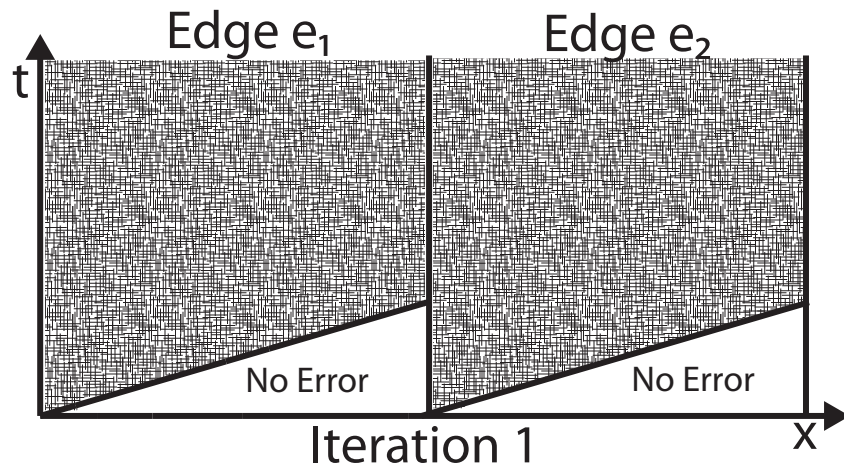


Figure 5.5: Error propagation after the first iteration for the two-edge loop network.

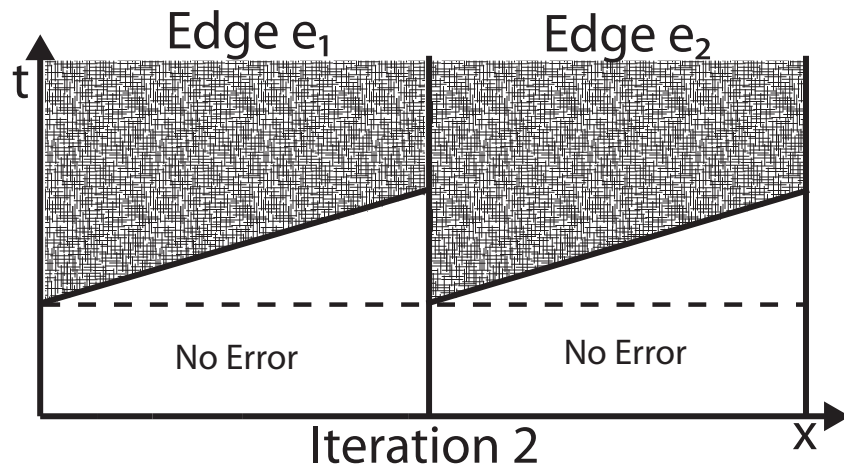


Figure 5.6: Error propagation after second iteration for two-edge loop network. At this iteration a region of exactness exists below the dotted line.



Figure 5.7: Two edge straight network. Domain decomposition will converge in two iterations, regardless of final time T .

time on the right boundary of both edges that has the exact solution. When the second iteration, $k = 2$, is calculated, this exact interval will propagate along with the error, as seen in Figure 5.6. Therefore, since no error enters through the boundary until after this interval of time, there exists a region in the spatio-temporal domain that will be exact. As the method iterates, the height of this region will increase, until eventually the final time T is reached.

Thus we see that, due to the finite speed of propagation and the fact that boundary data is taken from one boundary only, both classic properties of hyperbolic problems, the domain decomposition method will converge in a finite number of iterations. Note that if this were a straight network, see Figure 5.7, the method would converge in two iterations. At the first iteration, no error would exist in the left edge, since there is no edge to the left of it to give incorrect boundary data. Therefore, after the first iteration the left edge would be solved exactly for all time. That edge would then supply exact data to the right edge in the second iteration and it would be solve exactly for all time. This is why a loop network is the simplest network that can be used to see non-trivial convergence of the method.

5.2.2 Convergence Variables

While the above method is helpful in seeing graphically how convergence occurs, following the propagation of error would become increasingly complicated as the network and/or equation increased in complexity. We then need an analytical way of describing what is illustrated above. To do this we introduce convergence variables. We begin with a scalar advection equation.

Definition 7. Given a network $\mathcal{G} = (V, E)$ with the advection equation defined on each

edge,

$$\frac{\partial}{\partial t} u_{e_i}(x, t) + s_{e_i} \frac{\partial}{\partial x} u_{e_i}(x, t) = 0 \quad e_i \in E, x \in (a_{e_i}, b_{e_i}), 0 < t < T \quad (5.21)$$

We define a **convergence variable** $\tau_{e_i}^k$, where $e_i \in E$ and k is the iteration number, to be,

$$\tau_{e_i}^k = \sup\{t > 0 : |u_{e_i}^k(x, t) - u_{e_i}^*(x, t)| = 0 \quad \forall x \in [a_{e_i}, b_{e_i}]\} \quad (5.22)$$

where $u_{e_i}^*(x, t)$ is the exact solution along edge e_i .

So the convergence variables denote the height of the region of exactness as shown in Figure 5.6 above. Another way of defining $\tau_{e_i}^k$ is as the maximum time the method has converged to on edge e_i after iteration k . We then see that to determine an estimate on the number of iterations needed for convergence, we look for a k such that, $\tau_{e_i}^k \geq T$ for all $e_i \in E$.

We now define an update formula for the convergence variables. This formula will determine the value of $\tau_{e_i}^{k+1}$ given the value of $\tau_{e_i}^k$ for all edges $e_i \in E$. Since we know that $\tau_{e_i}^1 = 0$, due to the error in the initial iterate, we can use these update formulas to determine $\tau_{e_i}^k$ iteratively at any k . Multiple versions of these update formulas are given below. The formulas can depend on the form of the equations being solved, and the partitioning of the subdomains in the domain decomposition method. In the following sections we will describe various types of update formulas, as well as iteration estimate results.

5.2.3 Generalization to Systems

While the convergence variables defined above are a very useful method of determining convergence of the domain decomposition method, they are defined for linear scalar hyperbolic network problem. We want to generalize their use to linear systems of hyperbolic network problems. This can be done using characteristic variables.

Given a network $\mathcal{G} = (V, E)$, we define the following system of linear hyperbolic differential equations,

$$\frac{\partial}{\partial t} \mathbf{q}_{e_i}(x, t) + A_{e_i} \frac{\partial}{\partial x} \mathbf{q}_{e_i}(x, t) = 0 \quad e_i \in E, x \in [a_{e_i}, b_{e_i}], 0 < t < T \quad (5.23)$$

where $A_{e_i} \in \mathbb{R}^{n \times n}$ and $q_{e_i}(x, t) \in \mathbb{R}^n$. Since (5.23) is hyperbolic, it can be written in characteristic form,

$$\frac{\partial}{\partial t} \mathbf{w}_{e_i}(x, t) + D_{e_i} \frac{\partial}{\partial x} \mathbf{w}_{e_i}(x, t) = 0 \quad e_i \in E, x \in [a_{e_i}, b_{e_i}], 0 < t < T \quad (5.24)$$

where

$$D_{e_i} = \begin{bmatrix} \lambda_{e_i}^{(1)} & & & \\ & \lambda_{e_i}^{(2)} & & \\ & & \ddots & \\ & & & \lambda_{e_i}^{(n)} \end{bmatrix} \quad (5.25)$$

is a diagonal matrix containing the eigenvalues of A_{e_i} . In characteristic form, (5.23) becomes a decoupled system of advection equations. We can therefore apply our method of convergence variables to each linear scalar equation. This amounts to assigning a different convergence variable to track each characteristic variable,

$$\tau_{e_i,1} \mapsto w_{e_i}^{(1)} \quad \tau_{e_i,2} \mapsto w_{e_i}^{(2)} \quad \dots \quad \tau_{e_i,n} \mapsto w_{e_i}^{(n)}. \quad (5.26)$$

5.2.4 Constant Speed and Constant Length Edges

Given a network $\mathcal{G}(V, E)$, we begin our convergence study by assuming all edges $e_i \in E$ have constant length, and that our hyperbolic problem has constant speed of propagation. We first consider the advection equation,

$$\frac{\partial}{\partial t} u_{e_i}(x, t) + s_0 \frac{\partial}{\partial x} u_{e_i}(x, t) = 0 \quad e_i \in E, x \in (0, 1), 0 < t < T \quad (5.27)$$

where $s_0 \in \mathbb{R}$ is the constant speed of propagation. We partition the subdomains by assigning one edge to each subdomain, and introduce the following notation,

$$s_0^+ = \max\{s_0, 0\} \quad (5.28)$$

$$s_0^- = \min\{s_0, 0\}. \quad (5.29)$$

We now determine the update formula for (5.30) under these conditions. For each

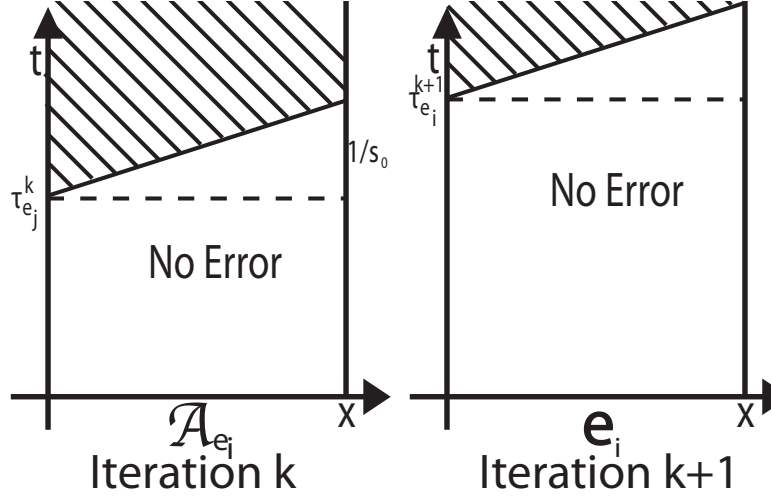


Figure 5.8: Convergence variable $\tau_{e_i}^{k+1}$ depends on convergence variables to the left at iteration k , and speed of propagation.

edge $e_i \in E$, the formula is given by,

$$\tau_{e_i}^{k+1} = \frac{s_0^+}{|s_0|} \min_{e_j \in \mathcal{A}_{e_i}} \{\tau_{e_j}^k\} + \frac{s_0^-}{|s_0|} \min_{e_m \in \mathcal{C}_{e_i}} \{\tau_{e_m}^k\} + \frac{1}{|s_0|}. \quad (5.30)$$

Recall that $\mathcal{A}_{e_i}(\mathcal{C}_{e_i})$ represents all incoming(outgoing) edges to the left(right) of edge e_i . Considering (5.30) we see that if $s_0 > 0$, the formula will depend on the convergence of the edges to the left of edge e_i at the previous iteration, and if $s_0 < 0$, the formula will depend on the convergence of the edges to the right of edge e_i at the previous iteration. The justification for this formula can be seen graphically in Figure 5.8. In these plots it is assumed that $s_0 > 0$, and we see how $\tau_{e_i}^{k+1}$ depends upon $\tau_{e_j}^k$, for $e_j \in \mathcal{A}_{e_i}$. The idea behind this and all update formulas is to consider all edges that affect the boundary of edge e_i , and use the smallest interval of exactness over those edges from the previous iteration. We will see that Equation (5.30) can be simplified greatly due to the fact that s_0 is constant across all edges, but the justification for it can be used for the more complicated cases given in later sections.

We now use formula (5.30) to prove the following theorem.

Theorem 2. *Given a network $\mathcal{G} = (V, E)$, with equation (5.30) defined on each edge. If the problem is solved to final time T with the domain decomposition method, with one edge*

assigned to each subdomain, then neglecting numerical error, the method will converge in at most $\lceil T|s_0| + 1 \rceil$ iterations.

We first simplify formula (5.30) by the following lemma,

Lemma 1. *Equation (5.30) can be rewritten as*

$$\tau_{e_i}^{k+1} = \frac{k}{|s_0|} \quad (5.31)$$

Proof. We prove this by induction. Assuming

$$\tau_{e_i}^1 = 0$$

$\forall e_i \in E$, we see that the lemma holds for $n = 1$. Assume (5.31) holds for $k = n$, then (5.30) gives,

$$\begin{aligned} \tau_{e_i}^{n+1} &= \frac{s_0^+}{|s_0|} \frac{n-1}{|s_0|} + \frac{s_0^-}{|s_0|} \frac{n-1}{|s_0|} + \frac{1}{|s_0|} \\ &= \frac{n-1}{|s_0|} + \frac{1}{|s_0|} \\ &= \frac{n}{|s_0|} \end{aligned}$$

□

Now using equation (5.31) and setting

$$\tau_{e_i}^k = T$$

we solve for k to prove Theorem 2.

When considering the acoustics equations,

$$\frac{\partial}{\partial t} \begin{bmatrix} p_{e_i} \\ u_{e_i} \end{bmatrix} + \begin{pmatrix} 0 & K_0 \\ 1/\rho_0 & 0 \end{pmatrix} \frac{\partial}{\partial x} \begin{bmatrix} p_{e_i} \\ u_{e_i} \end{bmatrix} = 0 \quad e_i \in E, x \in (0, 1), 0 < t < T \quad (5.32)$$

where the speed of sound is $c_0 = \sqrt{K_0/\rho_0}$ along all edges, we will have two convergence

variables,

$$\begin{aligned}\sigma_{e_i}^k &\mapsto \mathbf{w}_{e_i}^k(-c_0) =: w_{e_i}^k \\ \tau_{e_i}^k &\mapsto \mathbf{w}_{e_i}^k(c_0) =: z_{e_i}^k\end{aligned}$$

where $\mathbf{w}_{e_i}^k(-c_0)$ and $\mathbf{w}_{e_i}^k(c_0)$ represents the characteristic variable associated with eigenvalue $-c_0$ and c_0 respectively. By the same reasoning as the scalar case we define the update formulas to be,

$$\sigma_{e_i}^{k+1} = \min_{e_m \in \mathcal{C}_{e_i}, e_n \in \mathcal{D}_{e_i}} \{\tau_{e_m}^k, \sigma_{e_n}^k\} + \frac{1}{c_0} \quad (5.33)$$

$$\tau_{e_i}^{k+1} = \min_{e_j \in \mathcal{A}_{e_i}, e_\ell \in \mathcal{B}_{e_i}} \{\tau_{e_j}^k, \sigma_{e_\ell}^k\} + \frac{1}{c_0}. \quad (5.34)$$

We see that now the update formulas depend upon all the edges adjacent to edge e_i , since the junction conditions depend on all those edges. What is not written in (5.33)-(5.34) is that $\sigma_{e_i}^{k+1}$ depends upon $\tau_{e_i}^{k+1}$ and vice versa. These dependencies are not written because for the constant speed and edge length case, the convergence variables at iteration $k+1$ will always be greater than those at iteration k .

We notice that formulas (5.33) and (5.34) are similar in form to the scalar formula (5.30). Due to this, a similar theorem can be given for the acoustics equations.

Theorem 3. *Given a network $\mathcal{G} = (V, E)$, with equation (5.32) defined on each edge. If the problem is solved to final time T with the domain decomposition method, with the network partitioned along each edge, then neglecting numerical error, the method will converge in at most $\lceil Tc_0 + 1 \rceil$ iterations.*

A simplification similar to equation (5.31) can be shown, and used to prove Theorem 3.

Therefore we see that for the case of a network problem with constant speed of propagation and constant edge length, an analytical estimate can be obtained for the advection equation and the acoustics equations.

5.2.5 Variable Speed and Edge Length

The next case we consider is variable speed and edge length. For the linear acoustics equations, this corresponds to solving the following equation on edge e_i ,

$$\frac{\partial}{\partial t} \begin{bmatrix} p_{e_i} \\ u_{e_i} \end{bmatrix} + \begin{pmatrix} 0 & K_{e_i} \\ 1/\rho_{e_i} & 0 \end{pmatrix} \frac{\partial}{\partial x} \begin{bmatrix} p_{e_i} \\ u_{e_i} \end{bmatrix} = 0 \quad e_i \in E, x \in (a_{e_i}, b_{e_i}), 0 < t < T \quad (5.35)$$

where $c_{e_i} = \sqrt{K_{e_i}/\rho_{e_i}}$ is the speed of sound on edge e_i . This problem implies that the medium through which the sound propagates is different in each edge. We also consider the length of the edges to be nonuniform, however; we can transform this into a network with unit edge length.

Consider an edge e_i with length L_{e_i} . We introduce the following transformation of coordinates,

$$\hat{x} = \frac{x - a_{e_i}}{L_{e_i}}. \quad (5.36)$$

Rewriting equation (5.35) in terms of \hat{x} , we obtain,

$$\frac{\partial}{\partial t} \begin{bmatrix} p_{e_i} \\ u_{e_i} \end{bmatrix} + \frac{1}{L_{e_i}} \begin{pmatrix} 0 & K_{e_i} \\ 1/\rho_{e_i} & 0 \end{pmatrix} \frac{\partial}{\partial \hat{x}} \begin{bmatrix} p_{e_i} \\ u_{e_i} \end{bmatrix} = 0 \quad e_i \in E, x \in (0, 1), 0 < t < T. \quad (5.37)$$

This transforms the eigenvalues from c_{e_i} to $\frac{c_{e_i}}{L_{e_i}}$. When deriving an update formula, we assume unit edge length and modify the eigenvalues accordingly.

Here we give the update formula for the acoustics equations with variable speed of sound. As with the constant speed case, we partition a general network by assigning one edge to each subdomain. The same technique of minimum interval of exactness will be used to derive the update formulas. By considering the known variables at each junction we obtain,

$$\sigma_{e_i}^{k+1} = \min_{e_m \in \mathcal{C}_{e_i}, e_n \in \mathcal{D}_{e_i}} \left\{ \tau_{e_m}^k + \frac{1}{c_{e_m}}, \sigma_{e_n}^k + \frac{1}{c_{e_n}}, \tau_{e_i}^{k+1} + \frac{1}{c_{e_i}} \right\} \quad (5.38)$$

$$\tau_{e_i}^{k+1} = \min_{e_j \in \mathcal{A}_{e_i}, e_\ell \in \mathcal{B}_{e_i}} \left\{ \tau_{e_j}^k + \frac{1}{c_{e_j}}, \sigma_{e_\ell}^k + \frac{1}{c_{e_\ell}}, \sigma_{e_i}^{k+1} + \frac{1}{c_{e_i}} \right\}. \quad (5.39)$$

Note that we now include the dependency of $\sigma_{e_i}^{k+1}$ and $\tau_{e_i}^{k+1}$. This is because with variable

speed, it is possible for the convergence variables on the adjacent edges to be greater than the ones on edge e_i . Substituting equations (5.38) and (5.39) into each other, we get,

$$\sigma_{e_i}^{k+1} = \min_{\substack{e_j \in \mathcal{A}_{e_i}, e_\ell \in \mathcal{B}_{e_i} \\ e_m \in \mathcal{C}_{e_i}, e_n \in \mathcal{D}_{e_i}}} \left\{ \tau_{e_m}^k + \frac{1}{c_{e_m}}, \sigma_{e_n}^k + \frac{1}{c_{e_n}}, \tau_{e_j}^k + \frac{1}{c_{e_j}} + \frac{1}{c_{e_i}}, \sigma_{e_\ell}^k + \frac{1}{c_{e_\ell}} + \frac{1}{c_{e_i}}, \sigma_{e_i}^{k+1} + \frac{2}{c_{e_i}} \right\} \quad (5.40)$$

$$\tau_{e_i}^{k+1} = \min_{\substack{e_j \in \mathcal{A}_{e_i}, e_\ell \in \mathcal{B}_{e_i} \\ e_m \in \mathcal{C}_{e_i}, e_n \in \mathcal{D}_{e_i}}} \left\{ \tau_{e_j}^k + \frac{1}{c_{e_j}}, \sigma_{e_\ell}^k + \frac{1}{c_{e_\ell}}, \tau_{e_m}^k + \frac{1}{c_{e_m}} + \frac{1}{c_{e_i}}, \sigma_{e_n}^k + \frac{1}{c_{e_n}} + \frac{1}{c_{e_i}}, \tau_{e_i}^{k+1} + \frac{2}{c_{e_i}} \right\}. \quad (5.41)$$

We see that the $k+1$ term in both equations will never be chosen, since that would imply $0 = \frac{2}{c_{e_i}}$, which is only true if the speed of sound is infinite. Removing these terms we get our final update formulas,

$$\sigma_{e_i}^{k+1} = \min_{\substack{e_j \in \mathcal{A}_{e_i}, e_\ell \in \mathcal{B}_{e_i} \\ e_m \in \mathcal{C}_{e_i}, e_n \in \mathcal{D}_{e_i}}} \left\{ \tau_{e_m}^k + \frac{1}{c_{e_m}}, \sigma_{e_n}^k + \frac{1}{c_{e_n}}, \tau_{e_j}^k + \frac{1}{c_{e_j}} + \frac{1}{c_{e_i}}, \sigma_{e_\ell}^k + \frac{1}{c_{e_\ell}} + \frac{1}{c_{e_i}} \right\} \quad (5.42)$$

$$\tau_{e_i}^{k+1} = \min_{\substack{e_j \in \mathcal{A}_{e_i}, e_\ell \in \mathcal{B}_{e_i} \\ e_m \in \mathcal{C}_{e_i}, e_n \in \mathcal{D}_{e_i}}} \left\{ \tau_{e_j}^k + \frac{1}{c_{e_j}}, \sigma_{e_\ell}^k + \frac{1}{c_{e_\ell}}, \tau_{e_m}^k + \frac{1}{c_{e_m}} + \frac{1}{c_{e_i}}, \sigma_{e_n}^k + \frac{1}{c_{e_n}} + \frac{1}{c_{e_i}} \right\}. \quad (5.43)$$

5.2.6 Multi-Edge Subdomains

For our final case we again consider a network with constant speed c_0 and constant edge length. However, we partition the subdomains in a more useful way. Whereas previously we assigned one edge to each subdomain, we now allow the subdomains to contain multiple edges. While this complicates the analysis, it is a more realistic way of implementing the domain decomposition method. Very often, networks will have clusters, or regions of high intraconnectivity, and low interconnectivity with the rest of the network. Partitioning the network around these clusters makes efficient use of the method.

With larger subdomains, a similar convergence analysis technique can be used, with some differences. First, each edge is longer directly affected by the previous iterate of the adjacent edges. Instead, each subdomain will be affected by the previous iterate of the edges in adjacent subdomains. This will require a change in notation. We must modify our sets $\mathcal{A}_{e_i}, \mathcal{B}_{e_i}, \mathcal{C}_{e_i}$ and \mathcal{D}_{e_i} . Given an edge $e_i \in \mathcal{H}_{e_i} \subset E$, where \mathcal{H}_{e_i} is the subdomain

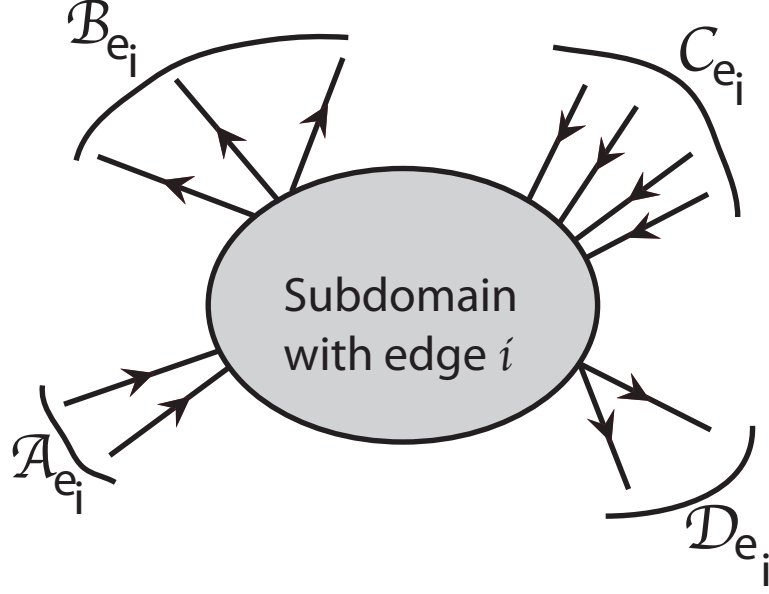


Figure 5.9: Sets defining the incoming and outgoing edges adjacent to a multi-edge subdomain.

containing e_i , we define,

$$\mathcal{A}_{e_i}^O = \{e_j \in E \setminus \mathcal{H}_{e_i} | e_j(\infty) = e_\ell(-\infty) \text{ for some } e_\ell \in \mathcal{H}_{e_i}\} \quad (5.44)$$

$$\mathcal{B}_{e_i}^O = \{e_j \in E \setminus \mathcal{H}_{e_i} | e_j(-\infty) = e_\ell(-\infty) \text{ for some } e_\ell \in \mathcal{H}_{e_i}\} \quad (5.45)$$

$$\mathcal{C}_{e_i}^O = \{e_j \in E \setminus \mathcal{H}_{e_i} | e_j(\infty) = e_\ell(\infty) \text{ for some } e_\ell \in \mathcal{H}_{e_i}\} \quad (5.46)$$

$$\mathcal{D}_{e_i}^O = \{e_j \in E \setminus \mathcal{H}_{e_i} | e_j(-\infty) = e_\ell(\infty) \text{ for some } e_\ell \in \mathcal{H}_{e_i}\}. \quad (5.47)$$

These sets are essentially the same as their counterparts, except for multi-edge subdomains. See Figure 5.9 for a graphical representation.

A second consequence of partitioning the network in this way is that there now exist interior edges. These are edges that are not directly affected by the previous iterate of the adjacent subdomains. This is because they do not touch the boundary of the subdomain in which they are contained. While these edges are not directly affected, there is still an indirect effect, which depends on their distance from the boundary of the subdomain, and must be taken into account in the update formula.

We define the update formula for multi-edge subdomains with constant speed for the

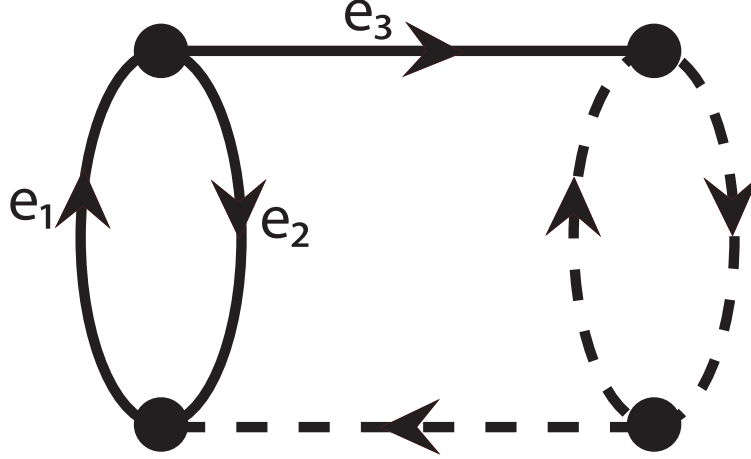


Figure 5.10: Network partitioned into two subdomains, each containing three edges.

acoustics equations.

$$\sigma_{e_i}^{k+1} = \min_{\substack{e_j \in \mathcal{A}_{e_i}^O, e_\ell \in \mathcal{B}_{e_i}^O \\ e_m \in \mathcal{C}_{e_i}^O, e_n \in \mathcal{D}_{e_i}^O}} \left\{ \tau_{e_m}^k + \frac{N_{im} + 1}{c_0}, \sigma_{e_n}^k + \frac{N_{in} + 1}{c_0}, \tau_{e_j}^k + \frac{L_{ij} + 2}{c_0}, \sigma_{e_\ell}^k + \frac{L_{i\ell} + 2}{c_0} \right\} \quad (5.48)$$

$$\tau_{e_i}^{k+1} = \min_{\substack{e_j \in \mathcal{A}_{e_i}^O, e_\ell \in \mathcal{B}_{e_i}^O \\ e_m \in \mathcal{C}_{e_i}^O, e_n \in \mathcal{D}_{e_i}^O}} \left\{ \tau_{e_j}^k + \frac{L_{ij} + 1}{c_0}, \sigma_{e_\ell}^k + \frac{L_{i\ell} + 1}{c_0}, \tau_{e_m}^k + \frac{N_{im} + 2}{c_0}, \sigma_{e_n}^k + \frac{N_{in} + 2}{c_0} \right\}. \quad (5.49)$$

We introduce the notation $L_{ij}(N_{ij})$ to represent the number of edges in the shortest path from where edge e_j connects to \mathcal{H}_{e_i} at the beginning(end) of edge e_i . This accounts for the indirect effect felt by the interior edges of a subdomain.

There is an interesting property of the convergence of the method under this type of partitioning of the network. Depending on how the partitioning is done, the number of iterations is reduced from the single edge subdomain case. To see this, we consider the network shown in Figure 5.10, and apply the update formulas to determine the convergence of this network.

Note that the network is split into two symmetric subdomains, each with three edges in them. Because of this, we will examine the convergence of edges e_1, e_2 , and e_3 only, as

the convergence of one side will be the same as the convergence of the other. We begin by initializing our convergence variables,

$$\sigma_{e_i}^1 = \tau_{e_i}^1 = 0 \quad , i = 1, 2, 3. \quad (5.50)$$

Next, by using the update formulas (5.48) and (5.49) we get the convergence variables at $k = 2$ to be,

$$\sigma_{e_1}^2 = \tau_{e_2}^2 = \tau_{e_3}^2 = \frac{2}{c_0} \quad (5.51)$$

$$\tau_{e_1}^2 = \sigma_{e_2}^2 = \sigma_{e_3}^2 = \frac{1}{c_0} \quad (5.52)$$

Continuing this process and using induction we can show that for iteration $k + 1$,

$$\sigma_{e_1}^{k+1} = \tau_{e_2}^{k+1} = \tau_{e_3}^{k+1} = \frac{2k}{c_0} \quad (5.53)$$

$$\tau_{e_1}^{k+1} = \sigma_{e_2}^{k+1} = \sigma_{e_3}^{k+1} = \frac{2k - 1}{c_0}. \quad (5.54)$$

Therefore if we solve our problem to time T , the domain decomposition method will converge in at most

$$k = \left\lceil \frac{Tc_0 + 3}{2} \right\rceil \quad (5.55)$$

iterations. Recall from Section 5.2.4 that when the network is partitioned into single edge subdomains, the method will converge in at most

$$k = \lceil Tc_0 + 1 \rceil \quad (5.56)$$

iterations. So we see that by partitioning into larger subdomains, the number of iterations for this network is cut roughly in half. While this is not true in general, it is shown often in numerical experiments presented below.

5.3 Numerical Results

Here we compare the convergence analysis above with numerical results. We solve the linear acoustics equations across various networks using domain decomposition. While for the constant speed and constant edge length case, Theorem 3 gives us an estimate on the number of iterations on any network, for the more complicated cases it is not possible to obtain such a closed form solution. In these cases, we have only the update formulas that describe how the convergence variables change from one iteration to the next. This update formula can be used to determine an estimate for a specific problem defined on a specific network. This is done relatively quickly with a computer program.

For the numerical results, the Kurganov-Tadmor method is used to solve along each edge, and the domain decomposition method described above is implemented to solve the entire network. Finally, our termination criterion for the domain decomposition method is small absolute change between iterations in the following norm,

$$\|q\|_{L_1, L_1} = \max_{e_i \in E} \|q_{e_i}(x, t)\|_{L_1, L_1}. \quad (5.57)$$

where the norm over a particular edge is given by,

$$\|q_{e_i}(x, t)\|_{L_1, L_1} = \int_0^T \int_{a_{e_i}}^{b_{e_i}} q_{e_i}(x, t) dx. \quad (5.58)$$

Therefore the termination criterion can be written as,

$$\|q^k - q^{k-1}\|_{L_1, L_1} < 10^{-3}. \quad (5.59)$$

5.3.1 Justification of the Update Formula

Before we compare the analytical and numerical results, we first want to graphically justify the update formulas (5.30) by recreating Figures 5.5 - 5.6 numerically. We do this

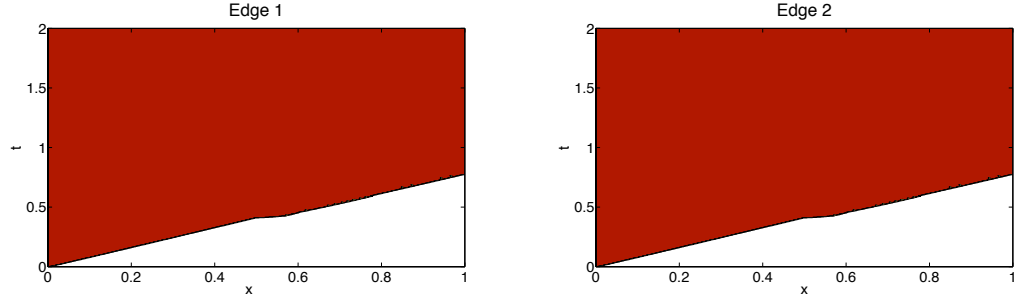


Figure 5.11: Numerical plot of error propagation for two-edge loop network after first iteration. Nodes used are 300.

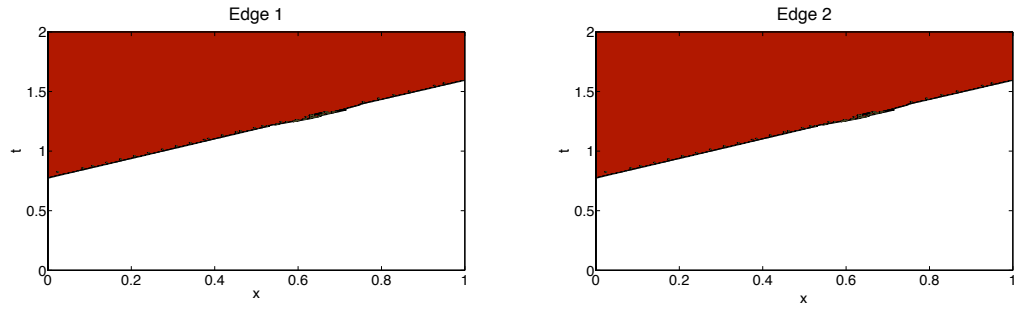


Figure 5.12: Numerical plot of error propagation for two-edge loop network after second iteration. Nodes used are 300.

by solving the linear acoustic equations,

$$\frac{\partial}{\partial t} \begin{bmatrix} p_{e_i} \\ u_{e_i} \end{bmatrix} + \begin{pmatrix} 0 & K_{e_i} \\ 1/\rho_{e_i} & 0 \end{pmatrix} \frac{\partial}{\partial x} \begin{bmatrix} p_{e_i} \\ u_{e_i} \end{bmatrix} = 0 \quad x \in (0, 1), t > 0 \quad (5.60)$$

$$p_{e_i}(x, 0) = 0 \quad x \in (0, 1) \quad (5.61)$$

$$u_{e_i}(x, 0) = 0 \quad x \in (0, 1) \quad (5.62)$$

over the loop network represented in Figure 5.4 with our domain decomposition code described above. To compare our results with Figures 5.5-5.6, we consider the characteristic variable associated with $\lambda = c_{e_i}$. This variable will behave similarly to the solution to the linear advection equation.

Note that we use zero initial conditions for this problem. This is to reduce the numerical error generated by solving the problem. Since the initial conditions are solutions to the differential equations, there should be less numerical error. This also can be thought of as representing the error of the solution with general initial conditions, by the superposition principle. Therefore it is easy to determine where error exists in the solutions and where it does not exist.

Finally, we use the following initial iterate,

$$p_{e_i}^0(x, t) = 10 \quad x \in (0, 1), \quad t > 0 \quad (5.63)$$

$$u_{e_i}^0(x, t) = 20 \quad x \in (0, 1), \quad t > 0. \quad (5.64)$$

Constant Speed Constant Length

First we consider the constant speed and edge length case. We choose ρ_0 and K_0 such that the speed of sound is $c_0 \approx 1.1832$. The results of the first two iterations of the domains decomposition method are shown in Figures 5.11-5.12 in an x - t plot. The shaded region represents points where the error is greater than 10^{-5} , and the light region is where the error is less than that tolerance. We see that error flows from the left boundary and propagates with a finite constant speed.

Variable Speed

We now consider the same loop network and acoustics equations, with different speeds of propagation defined on each edge. The speeds of propagation on edge 1 and edge 2 are

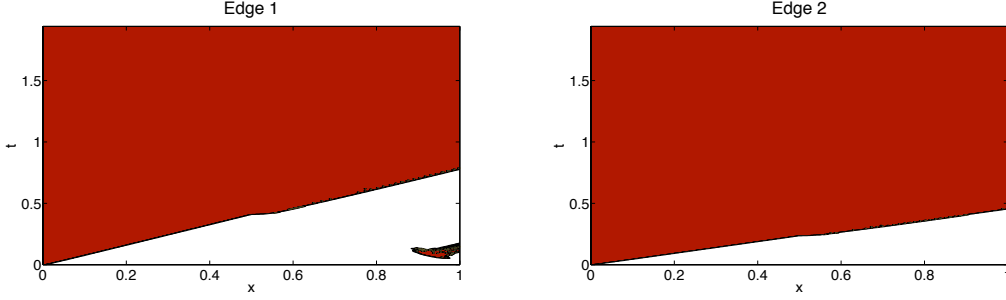


Figure 5.13: Numerical plot of error propagation for two-edge loop network with variable speed of propagation after first iteration. Nodes used are 300.

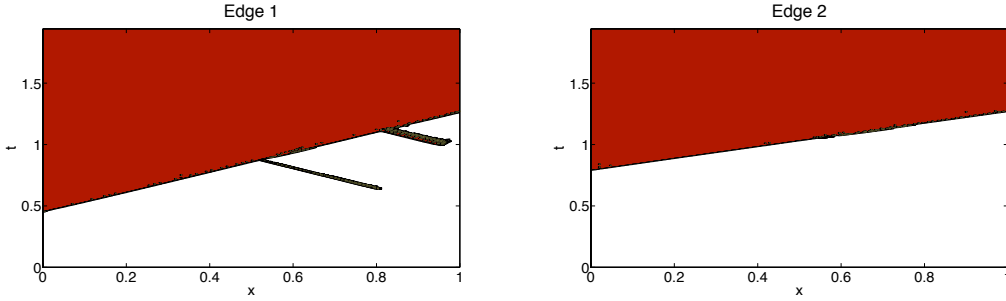


Figure 5.14: Numerical plot of error propagation for two-edge loop network with variable speed of propagation after second iteration. Nodes used are 300.

$c_{e_1} \approx 1.1832$ and $c_{e_2} \approx 2.0601$ respectively. Similar plots of the error propagation within the x - t plane are shown in Figures 5.13-5.14.

We see that the error propagates with finite speed, and is constant on each edge, but different between the two edges. We also see the interval of exactness at $x = 1$ after the first iteration is equal to the interval of exactness at $x = 0$ after the second iteration on the opposite edge.

5.3.2 Comparison of Iteration Estimates with Numerical Results

We now compare the iteration count obtained through our numerical results with the iteration estimates determined through the analysis presented above. For these results, we

will be using the linear acoustics equations (4.10), with the junction conditions continuity of pressure (4.16) and conservation of momentum (4.20).

The following initial conditions are implemented on each edge,

$$p_{e_i}(x, 0) = 10e^{-20(x-\frac{1}{2})^2} \quad e_i \in E, x \in (0, 1) \quad (5.65)$$

$$u_{e_i}(x, 0) = 0 \quad e_i \in E, x \in (0, 1). \quad (5.66)$$

These initial conditions are infinitely smooth, thus reducing any error introduced from discontinuities, and they are such that they satisfy the junction conditions at each node. The initial iterate for the domain decomposition method is chosen to be,

$$p_{e_i}^0(x, t) = 10 \quad e_i \in E, x \in (0, 1), t > 0 \quad (5.67)$$

$$u_{e_i}^0(x, t) = 20 \quad e_i \in E, x \in (0, 1), t > 0. \quad (5.68)$$

One quickly sees that this is by far not the optimal initial iterate for the method. A much better initial iterate would be a projection of the initial conditions $p_{e_i}(x, 0), u_{e_i}(x, 0)$ to all time. However, (5.67) and (5.68) are chosen to illustrate that the amount of error in the initial iterate does not greatly affect the convergence of the method, as our only assumption was that error existed, and nothing was assumed about the magnitude of the error.

We present our results below for four different networks. Two of the networks are small scale and the other two are on a larger scale to demonstrate that the above analysis still holds. We compare results for the three different cases listed above, constant speed and edge length, variable speed, and multi-edge subdomains. For the constant speed case, a sound speed of $c_0 \approx 1.1832$ was used. The first three networks are solved to final time $T = \frac{6}{\max_{e_i \in E} \{c_{e_i}\}}$. We also show results demonstrating the affect of how the subdomains are chosen, when multi-edge subdomains are used.

Three-Generation Binary Tree

In Table 5.1 we see the results from the three-generation binary tree network, shown in Figure 5.15. In an attempt to reduce the numerical error, we use 160 nodes on each edge. This is a typical example of a non-cyclic network. By comparing the analytical estimate with the iteration count obtained from the numerical experiment, we see that two more

Table 5.1: Comparison of analytical estimates to iteration count for the 3 generation binary tree.

	Uniform Speed	Variable Speed	Multi Edge Subdomain
Analytical Estimate	7	5	3
Actual Iteration Count	9	7	5

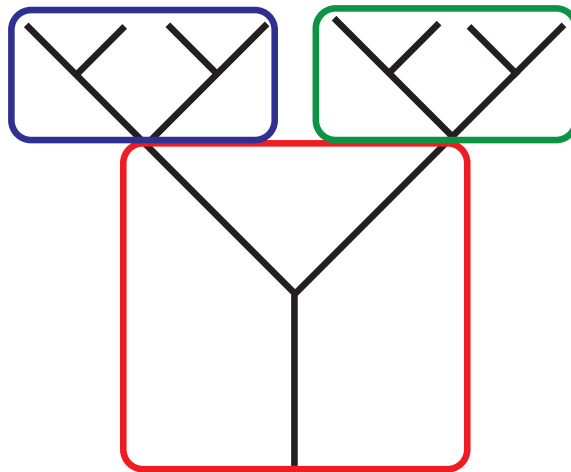


Figure 5.15: The three-generation binary tree. The multi-edge subdomains are shown.

iterations are needed than is predicted from the analysis. Recall that in the analysis we neglect numerical error. Due to the discretization of the problem, numerical error will always be introduced. The extra iterations that we see in the results are needed to filter out the numerical error in the problem.

The analytical estimates listed in Table 5.1 are determined via a computer program that iterates over the update formulas. Due to the random nature of the speed of propagation along the edges for the variable speed case, there is no expected value for the iteration estimate. For the multi-edge subdomain case, we partition the network as shown in Figure 5.15. It is interesting to note that the estimate for the multi-edge subdomain case is roughly half of the estimate for the constant speed case. This is what was determined for the cluster network in Equation (5.55).

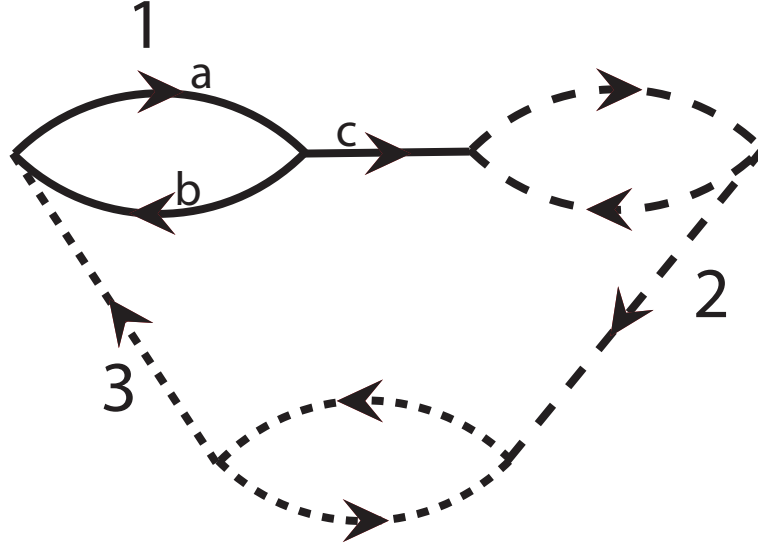


Figure 5.16: The three cluster network with partitioning.

Three-Clusters Network

The next network we consider is a three-cluster network, as seen in Figure 5.16. This network is very similar to the network in Figure 5.10. We again use 160 nodes on each edge. We list the comparison of the analytical iteration estimate with the actual iteration count in Table 5.2. Again we see that between one and three extra iterations are needed to filter out the numerical error.

Table 5.2: Comparison of analytical estimates to iteration count for the 3 Clusters Network.

	Uniform Speed	Variable Speed	Multi Edge Subdomain
Analytical Estimate	7	7	5
Actual Iteration Count	10	9	6

This network is analyzed above, only with two clusters instead of three. Our analysis stated that the domain decomposition method would converge in at most $\left\lceil \frac{Tc_0 + 3}{2} \right\rceil = 5$

iterations when $T = \frac{6}{c_0}$, which we see is supported by the results.

Bird Island Road Network

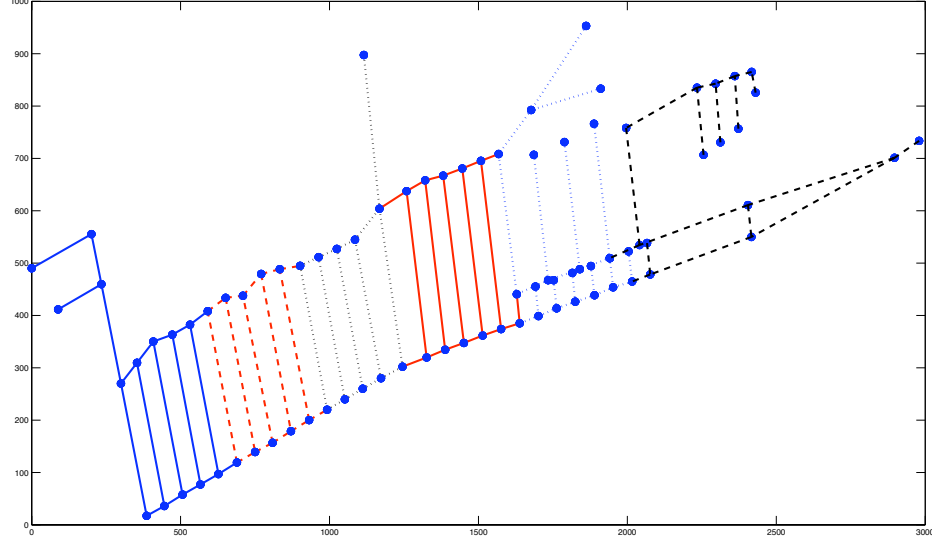


Figure 5.17: The traffic network on Bird Island, NC. The six subdomain are shown, three on each side of the main street.

We next consider a larger network, to show that these iteration estimates continue to hold as the network grows. To demonstrate this we use the traffic network of Bird Island, NC, see Figure 5.17. We continue to solve the acoustics equations along this network, taking advantage of its size and complexity. For the variable sound speed, we use constant sound speed and set the lengths of the edges based upon the road lengths. The results are shown in Table 5.3. For the multi-edge subdomain case, the network is split into 6 subdomains, separated by vertical roads. Finally, we note that for reasons of limited memory, 40 nodes were used in these calculations. Because of this, extra iterations are needed to resolve the numerical error, however we see that the iteration counts are still near the estimates.

Table 5.3: Comparison of analytical estimates to iteration count for the Bird Island Network.

	Uniform Speed	Variable Speed	Multi Edge Subdomain
Analytical Estimates	7	6	6
Actual Iteration Count	11	8	8

Caveman Network

The final network we consider is the Caveman network, shown in Figure 5.18. We do not examine this network to test the accuracy of the update formula, but to use the update formulas to demonstrate how different partitions of the network affect the iteration count. This type of network is a classical example of a clustered network. We show here that partitioning the subdomains around highly clustered nodes, that is nodes with high intraconnectivity, will decrease the iteration count.

We first state that for this example we solve the linear acoustics equations with constant speed and edge length, and to final time $T = \frac{9.8}{c_0}$, in order to fully demonstrate the effectiveness of proper partitioning. Also, as for the Bird Island network, 40 nodes were used on each edge for limited memory purposes. We partition the network three different ways, to demonstrate that how the subdomains are partitions affects the iteration count. The first method is the standard partitioning of one edge per subdomain. In the second partitioning, we create three subdomains about the clusters of the network, as shown in Figure 5.18. The final partitioning creates three subdomains, but do not take advantage of the clustering feature of the network, as shown in Figure 5.19. Table 5.4 shows our results.

Table 5.4: Comparison of various partitioning of the caveman network.

	Single Edge	Clustering	Non-clustering
Analytical Estimates	11	8	11
Actual Iteration Count	18	9	11

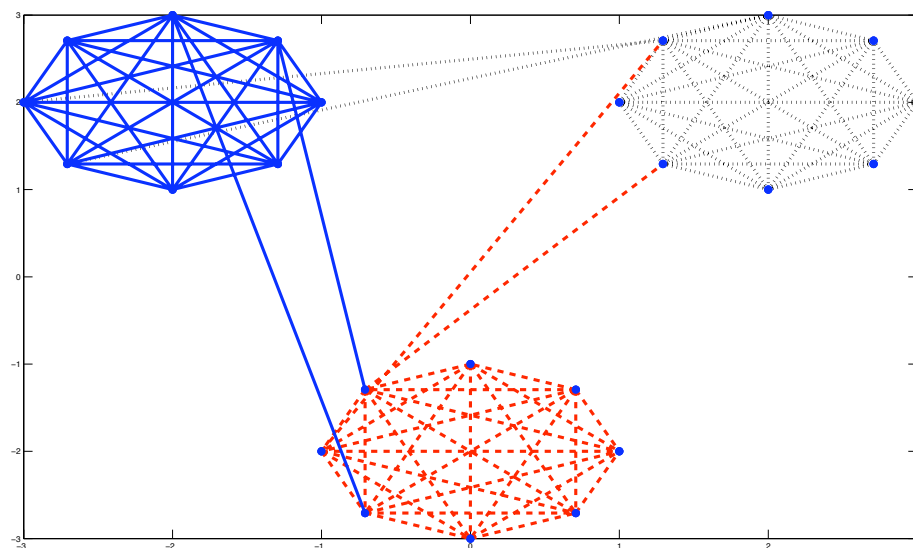


Figure 5.18: Caveman network with three "caves" and 8 nodes per cave. Subdomains are defined to take advantage of the clustering inherent to the network.

So we see that it is not simply the number of subdomains that affects the iteration count, but also how those subdomains are defined. Three subdomains is significantly less than the number of edges in the caveman network, however, the non-clustered partitioning has the same theoretical iteration estimate as the single edge partitioning. However, we see that three subdomains that take advantage of the network clustering has a lower iteration estimate.

5.4 Conclusions

So we see that the iteration estimates have very interesting and useful results. An immediate result we notice about them is that the number of iterations required for convergence depends upon the final time T as well as the speed of propagation along the edges. It also seems that the partitioning of the subdomains plays a role in the number of iterations for the method. Knowing how each of these variables affect the iterations can be useful in determining how a particular problem should be solved.

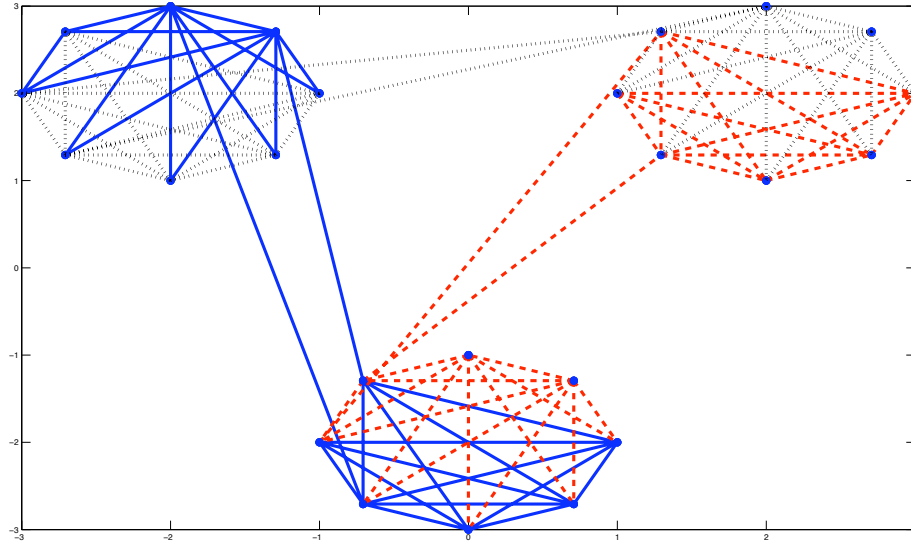


Figure 5.19: Caveman network with three "caves" and 8 nodes per cave. Partitioning does not take advantage of clustering within the network.

A network problem can be solved in essentially two ways, serially or in parallel. By solving a problem serially, we mean that each edge is solved one after another without domain decomposition. When solving a problem in parallel, we use domain decomposition and split up the computation of the subdomains between multiple processors and have them all solve their particular problems simultaneously. Solving in parallel is not necessarily faster, since there is a balance between the number of iterations and the time saved by solving multiple parts of the network simultaneously.

The iteration estimates can be useful in determining which way this balance falls. Let us consider a simplified calculation of the computational time required to solve a network problem both ways. First, we ignore all communication time between processors. While it is known that this is usually the bottleneck of any parallel processing computation, this assumption is adequate for our problem. Since we partition our network first, and then solve across the entire spatio-temporal cylinder, as described above, there is relatively little communication between processors, simply the communication of the junction values at the end of each iteration. Also, as the size of the network increases to large-scale, the

computational time of solving the network will be much larger than the communication time between processors. Therefore, under this assumption, let us assume that solving the entire network, that is solving the problem serially, costs $O(1)$ work. If we then have P processors, and the domain decomposition method takes N iterations, we say that the cost of solving the problem in parallel is $O\left(\frac{N}{P}\right)$. So under these assumption, we say that it is more efficient to solve the problem in parallel if,

$$N < P. \tag{5.69}$$

Using our estimates for the iteration count, we can use Equation (5.69) to determine for a particular problem, if solving it in parallel is the most efficient method.

As seen in the results above, the partitioning of the network also has an effect on iteration count of the domain decomposition method. The program used to estimate the iteration count can be used to determine *a priori* the optimal partitioning of the network.

Chapter 6

Numerical Investigation of Gas Flow through a Nozzle

6.1 Introduction

In the next two chapters we continue to consider network problems, but in a local sense. While previously we considered relatively simple problems across a full network, we now move to considering complex problems over a small portion of the network. In particular, the complex problem of gas flow, modeled by the Euler gas dynamics equations. This system of nonlinear conservation laws makes modeling over a network considerably more complicated than the linear acoustics equations studied above.

First we recall that a network problem modeling a physical phenomenon is a one-dimensional approximation of a multi-dimensional model. Along the straight portions of the network, it is typical to apply some sort of dimensional averaging to reduce the multi-dimensional equations to a system of one-dimensional equations. Since the geometry of this region is assumed to not change along its length, these averaged equations are assumed to approximate the multi-dimensional equations. These regions are approximated by the edges of the network. In regions where the geometry is not straight, the domain is reduced to a vertex and algebraic relations are used to approximate the solution. We call these regions junctions. In this chapter we will look more closely at junctions, and consider how well their algebraic relations approximate the multi-dimensional solution.

Here we consider a nozzle junction. This is where the area of the pipe changes across the junction in some way, see Figure 6.1. This is perhaps the simplest type, as

only two edges are involved and there is a minimal change in the geometry between the two straight pipes. When determining the junction conditions for the nozzle, we apply the same dimensional averaging used on the straight pipe, to the region in which the area changes. This creates an extra term in the averaged one-dimensional differential equations. By doing this we see that the algebraic junction conditions are incorporated within the differential equations. We will compare the results of this network model to the multi-dimensional solution to determine how well it is approximated by the network model.

6.1.1 Previous Work

Much work has been done studying the one-dimensional formulation of nozzle flow. One of the earliest set of papers was by Liu in [32, 59, 60]. He examined the asymptotic solutions of the polytropic Euler equations in both a converging and diverging nozzle. The one-dimensional formulation was used to study stability properties of flow through a nozzle. Similar results were obtained in [27] for the isentropic equations. The two-dimensional nozzle was studied in [96] and similar properties were determined.

In more recent papers, a detailed analysis of the one-dimensional equations has been performed. In [17, 18, 19] we see a general junction between two pipes modeled using various junction conditions, the motivation being a nozzle junction. In [3, 45, 52, 85], a full description of the solution to the Riemann problem for the one-dimensional nozzle equations is given. It is a summary of this work that is presented at the beginning of this chapter. In [3, 85] a way of constructing solutions to the Riemann problem for the polytropic equations is given, which is used in our results. A main property of this problem is that multiple entropy satisfying solutions are possible for certain initial conditions, thus making modeling with these equations difficult.

6.2 Analysis of Nozzle flow equations

Gas flow through a nozzle has been studied by many, as seen above. However, there are two works, [3, 85] that are of particular importance to our research. They provide the analytical background for the equations of gas flow through a nozzle and help us understand properties of the solution. This section gives the derivation of the one-dimensional equations, as well as the analysis of those equations done by Thanh in [85].

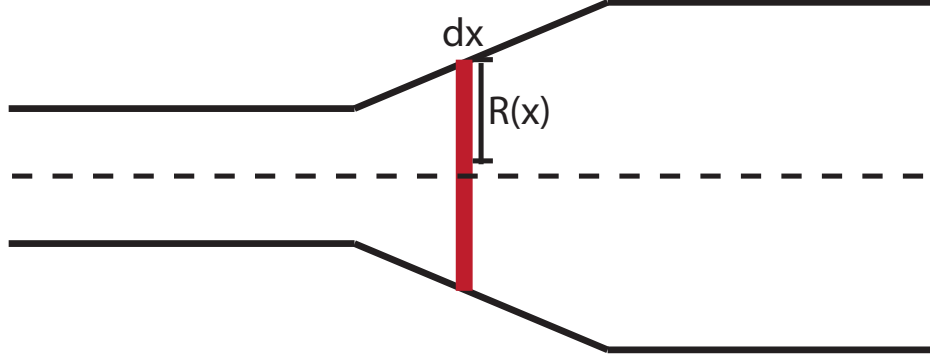


Figure 6.1: The cross section of the nozzle over which the radial averaging takes place.

6.2.1 Derivation

We begin our discussion of the nozzle equations by deriving them in their one-dimensional form from first principles, noting various assumptions made along the way. We start with the full three-dimensional equations for gas flow through a pipe.

$$\frac{\partial}{\partial t} \rho + \nabla \cdot (\rho \mathbf{u}) = 0 \quad (6.1)$$

$$\frac{\partial}{\partial t} (\rho \mathbf{u}) + \nabla \cdot (\rho \mathbf{u} \otimes \mathbf{u} + p \mathbf{I}) = 0 \quad (6.2)$$

$$\frac{\partial}{\partial t} E + \nabla \cdot ((E + p) \mathbf{u}) = 0 \quad (6.3)$$

in $\Omega \times \mathbb{R}^+$, where ρ , \mathbf{u} and E are the density, velocity, and energy respectively, and Ω is the interior of the pipe. The pressure p is chosen as a function of the other state variables depending on the gas being modeled. We are modeling ideal polytropic gas, so we take,

$$p = (\gamma - 1)E - \frac{\gamma - 1}{2} \rho \|\mathbf{u}\|^2 \quad (6.4)$$

where $\gamma = 1.4$ and $\|\mathbf{u}\|$ is the Euclidean norm. Note the geometry of the pipe, i.e. the change in area, does not enter into the equations themselves, only in the domain Ω .

The next step is to assume that the geometry of the pipe is axisymmetric. This is a natural assumption for most pipes. In doing this we write (6.1)-(6.3) in cylindrical coordinates with the axial coordinate aligned with the axis of the pipe. By assuming

$\partial_\theta q = 0$ for each state variable q we reduce the dimension of our equations to two.

$$\partial_t \rho + \partial_x(\rho u) + \partial_r(\rho v) = -\frac{\rho v}{r} \quad (6.5)$$

$$\partial_t(\rho u) + \partial_x(\rho u^2 + p) + \partial_r(\rho uv) = -\frac{\rho uv}{r} \quad (6.6)$$

$$\partial_t(\rho v) + \partial_x(\rho uv) + \partial_r(\rho v^2 + p) = -\frac{\rho v^2}{r} \quad (6.7)$$

$$\partial_t E + \partial_x(u(E + p)) + \partial_r(v(E + p)) = -\frac{v(E + p)}{r} \quad (6.8)$$

for $x \in \mathbb{R}$, $r \in (0, R(x))$, $t \in \mathbb{R}^+$ and $u = \mathbf{u}_x$ and $v = \mathbf{u}_r$ are the radial and axial velocities. The source terms arise from the angular terms in the three-dimensional system, by eliminating the dependence on r in the flux terms. Solid wall boundary conditions are give at the nozzle wall $r = R(x)$ by,

$$v(R) = u(R) \frac{dR}{dx}, \quad (6.9)$$

which states that the velocity vector is tangent to the wall.

Finally we reduce the two-dimensional system to one dimension via radial averaging, similar to what was done in Chapter 3. We begin by defining the radially averaged variables to be,

$$\frac{2\pi}{a(x)} \int_0^R q r dr = \bar{q} \quad (6.10)$$

where q is some state variable, and $a(x) = \pi R^2(x)$ is the area of the pipe at x ; see Figure 6.1. Next, we integrate Equations (6.5)-(6.8) across this cross sectional area to eliminate the radial derivative and rewrite the equations in terms of the averaged variables. There are multiple terms, so we demonstrate the averaging technique with the axial momentum equation (6.6). Starting with the time derivative term we get,

$$\int_0^R \partial_t \rho u r dr = \partial_t \int_0^R \rho u r dr = \partial_t \left(\frac{a(x)}{2\pi} \bar{\rho u} \right). \quad (6.11)$$

Here we make note of an assumption used in the averaging technique, namely that for

two quantities p and q ,

$$\overline{pq} = \bar{p}\bar{q}. \quad (6.12)$$

This says that average of the product is equal to the product of the averages. This is not true in general, however if we assume the solution has small variation in the radial direction we can make this assumption. When averaging the radial term, we must first use the product rule to move all factors inside of the derivative,

$$\int_0^R \partial_r(\rho uv) r dr = \int_0^R \partial_r(\rho uvr) dr - \int_0^R \rho uvd r \quad (6.13)$$

$$= \rho(R)u(R)v(R)R - \int_0^R \rho uvd r. \quad (6.14)$$

Note that the last term in the averaged radial derivative cancels directly with the averaged source term in equation (6.6). Finally, averaging the axial derivative, we get,

$$\int_0^R \partial_x(\rho u^2 + p) r dr = \partial_x \int_0^R (\rho u^2 + p) r dr - (\rho(R)u(R)^2 + p(R))RR' \quad (6.15)$$

$$= \partial_x \left[\frac{a}{2\pi} (\bar{\rho}\bar{u}^2 + \bar{p}) \right] - \rho(R)u(R)v(R)R - p(R)RR' \quad (6.16)$$

where in the last step we used the boundary condition (6.9). Putting all of our averaged terms together we get,

$$\partial_t(a\bar{\rho}\bar{u}) + \partial_x[a(\bar{\rho}\bar{u}^2 + \bar{p})] = p(R)2\pi RR'. \quad (6.17)$$

Our last assumption is that the pressure at the nozzle wall $p(R)$ is equal to the average pressure \bar{p} . This procedure and assumptions are applied similarly to the other two-dimensional equations to obtain the following one-dimensional equations for gas flow through a nozzle.

$$\partial_t(a\rho) + \partial_x(a\rho u) = 0 \quad (6.18)$$

$$\partial_t(a\rho u) + \partial_x(a(\rho u^2 + p)) = p \frac{d}{dx} a \quad (6.19)$$

$$\partial_t(aE) + \partial_x(au(E + p)) = 0, \quad (6.20)$$

in $\mathbb{R} \times \mathbb{R}^+$. Note that these equations look very similar to the usual one-dimensional Euler gas dynamics equations. The only differences being the factor of a , and the source term in the momentum equation. The factor of a does not change the behavior of the equations much, as shown below, however the source term gives many changes to the behavior and is in fact the focus of the analysis.

6.2.2 Augmented System

The presence of a right hand term in the nozzle equations (6.18)-(6.20) introduces two complications to the system. The source term implies that the (6.18)-(6.20) is a system of balance laws as opposed to conservation laws. The factor of $a(x, t)$ in each term introduces a dependency on x into the equations. There is a simple fix to remove these complication, we let $a(x, t)$ be one of the state variables, i.e. one of the unknowns. We then augment the equations with,

$$\partial_t a = 0. \quad (6.21)$$

Therefore, a can be determined completely from initial conditions.

When a is considered as a state variable, the nozzle equations (6.18)-(6.20) have no explicit x dependence. For smooth solutions, we can rewrite them in nonconservative form,

$$\partial_t \mathbf{w} + B \partial_x \mathbf{w} = 0, \quad (6.22)$$

where,

$$\mathbf{w} = \begin{pmatrix} \rho \\ u \\ p \\ a \end{pmatrix} \quad B = \begin{pmatrix} u & \rho & 0 & \frac{\rho u}{a} \\ 0 & u & \frac{1}{\rho} & 0 \\ 0 & \gamma p & u & \frac{\gamma u p}{a} \\ 0 & 0 & 0 & 0 \end{pmatrix}. \quad (6.23)$$

The eigenvectors of the matrix B are,

$$\mathbf{v}_0 = \begin{bmatrix} \frac{\rho u^2}{a(c^2 - u^2)} \\ \frac{-cu}{a(c^2 - u^2)} \\ \frac{\rho u^2 c^2}{a(c^2 - u^2)} \\ 1 \end{bmatrix} \quad \mathbf{v}_1 = \begin{bmatrix} \frac{1}{c^2} \\ \frac{-1}{\rho c} \\ 1 \\ 0 \end{bmatrix} \quad \mathbf{v}_2 = \begin{bmatrix} 1 \\ 0 \\ 0 \\ 0 \end{bmatrix} \quad \mathbf{v}_3 = \begin{bmatrix} \frac{1}{c^2} \\ \frac{1}{\rho c} \\ 1 \\ 0 \end{bmatrix} \quad (6.24)$$

and the eigenvalues of B are,

$$\lambda_0 = 0, \quad \lambda_1 = u - c, \quad \lambda_2 = u, \quad \lambda_3 = u + c \quad (6.25)$$

where $c = \sqrt{\gamma p / \rho}$ is the speed of sound. Notice that the same eigenvalues found in the Euler gas dynamics equations are here, as well as a zero eigenvalue. It is useful to introduce the following sets,

$$\mathcal{G}_1 = \{\mathbf{w} = (\rho, u, p, a) | \lambda_0(\mathbf{w}) < \lambda_1(\mathbf{w})\} \quad (6.26)$$

$$\mathcal{G}_2 = \{\mathbf{w} = (\rho, u, p, a) | \lambda_1(\mathbf{w}) < \lambda_0(\mathbf{w}) < \lambda_2(\mathbf{w})\} \quad (6.27)$$

$$\mathcal{G}_3 = \{\mathbf{w} = (\rho, u, p, a) | \lambda_2(\mathbf{w}) < \lambda_0(\mathbf{w}) < \lambda_3(\mathbf{w})\} \quad (6.28)$$

$$\mathcal{G}_4 = \{\mathbf{w} = (\rho, u, p, a) | \lambda_3(\mathbf{w}) < \lambda_0(\mathbf{w})\}. \quad (6.29)$$

These sets partition state space into regions with the same characteristic structure.

This augmented system of equations has many of the same properties as the original gas dynamics equations, the difference coming from the zero eigenvalue.

6.2.3 Analysis of the Riemann Problem

To analyze this new system of equations, we start with the simplest problem, the Riemann problem, that is piecewise constant initial conditions,

$$\mathbf{w}(x, 0) = \begin{cases} \mathbf{w}_L & , \quad x \leq x_0 \\ \mathbf{w}_R & \quad x > x_0 \end{cases}. \quad (6.30)$$

Since the area of the nozzle is now a state variable, considering Riemann initial conditions implies that we are considering a nozzle with a discontinuous jump in area. This approximates a nozzle with a steep change in area.

The solution to the Riemann problem consists of a set of elementary waves emanating from the jump in initial conditions. We know, since the equations are so similar to the Euler equations, that shocks and rarefactions associated with λ_1 and λ_3 are part of these elementary waves, as well as a contact discontinuity associated with λ_2 . We also have a contact discontinuity associated with λ_0 . As the other types of waves have been well analyzed, it is this wave that we describe here.

The 0-characteristic field is linearly degenerate. Therefore in the solution to the Riemann problem, there will be a stationary contact discontinuity associated with it. By examining the Riemann invariants, we see that the following quantities must be constant across this contact discontinuity [85],

$$a\rho u, \quad \frac{u^2}{2} + \frac{\gamma}{\gamma-1} \frac{p}{\rho}, \quad S \quad (6.31)$$

where S is the entropy. If we then fix the states ρ_0, u_0, p_0 on one side of the discontinuity and assume the areas are known on both sides, we get the following relations that must hold across the contact discontinuity,

$$a_0\rho_0u_0 = a_1\rho u \quad (6.32)$$

$$\frac{u_0^2}{2} + \frac{\gamma}{\gamma-1} \frac{p_0}{\rho_0} = \frac{u^2}{2} + \frac{\gamma}{\gamma-1} \frac{p}{\rho} \quad (6.33)$$

$$\frac{p_0}{\rho_0^\gamma} = \frac{p}{\rho^\gamma} \quad (6.34)$$

By some simple algebra, we can rewrite Equations (6.32)-(6.34) as one equation for ρ [85],

$$\Phi(\rho) := -\frac{2\kappa\gamma}{\gamma-1}\rho^{\gamma+1} + \left(u_0^2 + \frac{2\kappa\gamma}{\gamma-1}\rho_0^{\gamma-1}\right)\rho^2 - \left(\frac{a_0u_0\rho_0}{a_1}\right)^2 = 0 \quad (6.35)$$

where $\kappa = p_0/\rho_0^\gamma$. If a solution ρ to (6.35) can be found, relations (6.32) and (6.34) can be used to determine the full state variable $\mathbf{w} = (\rho, u, p, a)^T$. It is shown in detail in [85] and summarized in Appendix A, that Equation (6.35) has at most two solutions. A selection criterion is given in [3] which states that if $\mathbf{w}_0 = (\rho_0, u_0, p_0, a_0)^T \in \mathcal{G}_i$ then the correct solution to (6.35) lies in \mathcal{G}_i .

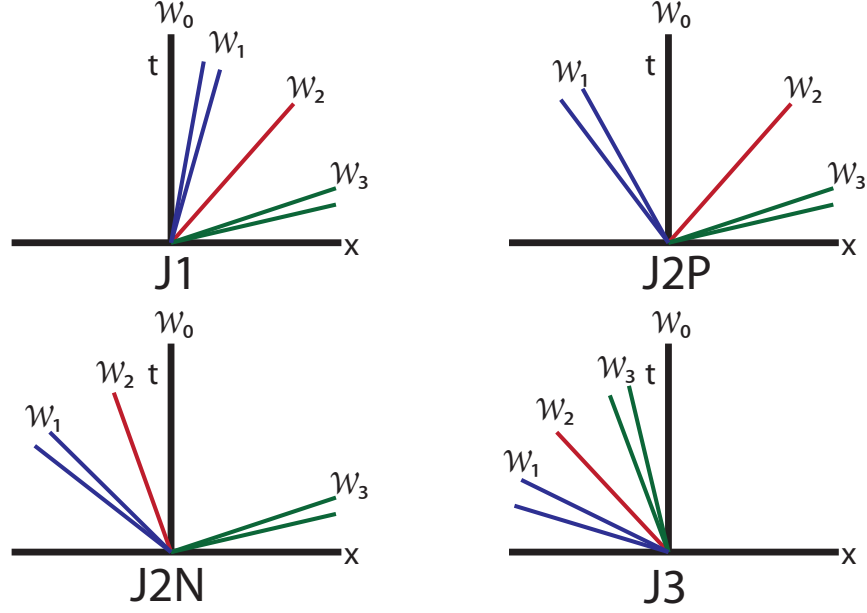


Figure 6.2: Four main constructions possible with the augmented system of equations.

6.2.4 Solutions to the Riemann Problem

Once we have a good understanding of the contact discontinuity associated with the 0-eigenvalue, we can begin constructing solutions to the Riemann problem of our augmented system. We start by defining the elementary waves that make up the solution.

Definition 8. The **elementary waves** that make up the solution to the Riemann problem of the augmented system (6.22) are:

- The standard entropy satisfying shocks, rarefactions and contact discontinuities associated with the usual Euler gas dynamics equations.
- The stationary contact discontinuity associated with the 0-eigenvalue.

Hence, solutions to the augmented system will be similar to solutions of the usual gas dynamics equations, with the addition of the stationary 0-wave at the discontinuity in the nozzle area. This wave is of great importance, as it fundamentally changes the solution. Where in the usual gas dynamics equations, the wave speeds always have the same order, due to the definition of the eigenvalues, the 0-wave has constant speed. Due to this constant speed, multiple different ordering of the waves, or constructions are

possible; see Figure 6.2. These different constructions must be treated independently, as they each give a different solution.

We now introduce some notations used in [85] to help in describing the different types of constructions.

- Let $\mathcal{W}_i(\mathbf{w}_L, \mathbf{w}_R)$ denote an i -wave connecting a state \mathbf{w}_L on the left with a state \mathbf{w}_R on the right.
- We denote by $\mathcal{W}_i(\mathbf{w}_L, \mathbf{w}_m) \oplus \mathcal{W}_j(\mathbf{w}_m, \mathbf{w}_R)$, two waves connecting a left state \mathbf{w}_L to a right state \mathbf{w}_R via an intermediate state \mathbf{w}_m , using first an i -wave, then a j -wave.
- Let $s(\mathbf{w}_L, \mathbf{w}_R)$ denote the speed of a shock connecting the states \mathbf{w}_L on the left with \mathbf{w}_R on the right.

Using this notation, various constructions were described by Thanh in [85]. We describe the four basic constructions that can exist as seen in Figure 6.2. We assume that we start with Riemann initial conditions (6.30).

Construction J1 For this construction to exist we require $\mathbf{w}_L \in \mathcal{G}_1$, so that it is possible for the 1-wave to have positive speed. The ordering of the waves for this construction is the following,

$$\mathcal{W}_0(\mathbf{w}_L, \mathbf{w}_1) \oplus \mathcal{W}_1(\mathbf{w}_1, \mathbf{w}_2) \oplus \mathcal{W}_2(\mathbf{w}_2, \mathbf{w}_3) \oplus \mathcal{W}_3(\mathbf{w}_3, \mathbf{w}_R). \quad (6.36)$$

This construction makes sense when the shock speed of the 1-wave, $s(\mathbf{w}_1, \mathbf{w}_2) > 0$.

Construction J3 This construction is the opposite of Construction J1. For this solution to exist we require $\mathbf{w}_R \in \mathcal{G}_4$, so that it is possible for the 3-wave to have negative speed. The ordering of the waves will be,

$$\mathcal{W}_1(\mathbf{w}_L, \mathbf{w}_1) \oplus \mathcal{W}_2(\mathbf{w}_1, \mathbf{w}_2) \oplus \mathcal{W}_3(\mathbf{w}_2, \mathbf{w}_3) \oplus \mathcal{W}_0(\mathbf{w}_3, \mathbf{w}_R) \quad (6.37)$$

and this solution will make sense when the 3-shock speed $s(\mathbf{w}_2, \mathbf{w}_3) < 0$.

Construction J2P, J2N In the final two constructions, the left and right states can be in any region of state space. The difference between Construction J2P and J2N

is the direction of the 2-wave, and so depends on the intermediate velocity. So we see that the ordering of the waves,

$$\mathcal{W}_1(\mathbf{w}_L, \mathbf{w}_1) \oplus \mathcal{W}_0(\mathbf{w}_1, \mathbf{w}_2) \oplus \mathcal{W}_2(\mathbf{w}_2, \mathbf{w}_3) \oplus \mathcal{W}_3(\mathbf{w}_3, \mathbf{w}_R) \quad (6.38)$$

makes sense if the velocity $u_2 = u_3 > 0$, and the ordering,

$$\mathcal{W}_1(\mathbf{w}_L, \mathbf{w}_1) \oplus \mathcal{W}_2(\mathbf{w}_1, \mathbf{w}_2) \oplus \mathcal{W}_0(\mathbf{w}_2, \mathbf{w}_3) \oplus \mathcal{W}_3(\mathbf{w}_3, \mathbf{w}_R) \quad (6.39)$$

makes sense if the velocity $u_1 = u_2 < 0$.

These are the four basic constructions. There are more complicated constructions that can exist [85]. One of them allows a J1 type construction when the left state is not in \mathcal{G}_1 . This is done by introducing an extra 1-wave to the left of the 0-wave, which transfers the left state to \mathcal{G}_1 . A similar construction can be made for type J3 when the right state is not in \mathcal{G}_4 . These, and other extraordinary types of solutions will not be considered in this work.

When considering the four basic constructions, the intermediate states can be determined in a similar manner to determining the intermediate states for the usual gas dynamics equations. The equations describing the 1-wave and 3-wave in p - u space can still be used, and we know the relation across the 0-wave. Using these conditions, it is possible to determine all intermediate states as long as a particular construction is assumed.

6.2.5 Non-Unique Solutions

We briefly note a property of the nozzle equations, that they do not always have a unique entropy satisfying solution. This is due to the fact that there are multiple constructions as listed above. Therefore, there exist initial conditions to the Riemann problem that admit two different constructions. One such example is,

$$\begin{aligned} \rho_L &= .2 & \rho_R &= .2 \\ p_L &= 1 & p_R &= .07 \\ u_L &= 3.3 & u_R &= -4 \\ a_L &= .3 & a_R &= .8. \end{aligned}$$

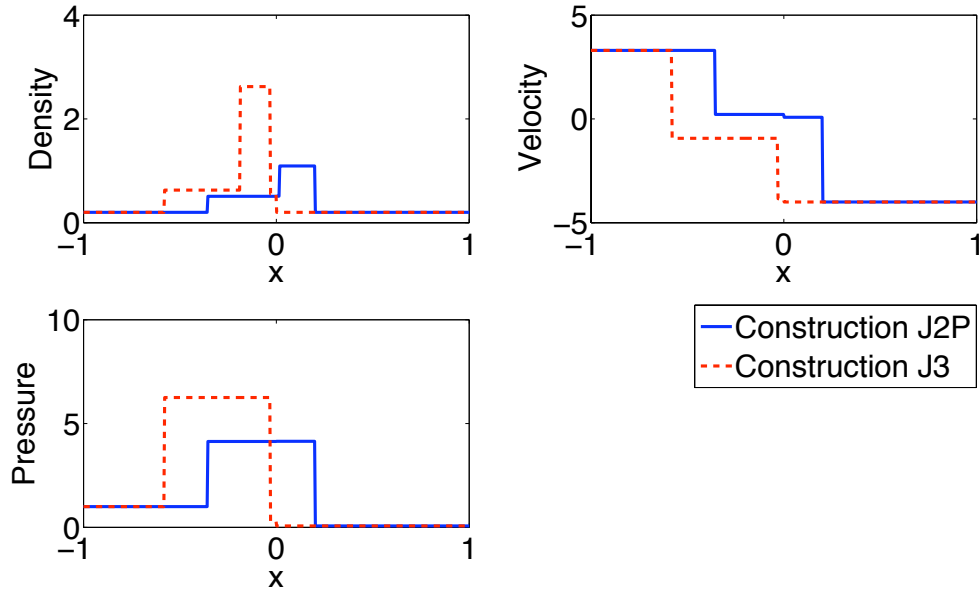


Figure 6.3: Two entropy satisfying solutions to the nozzle equations.

With these initial conditions, Constructions J2P and J3 are both possible. Both solutions are plotted in Figure 6.3.

This extra level of non-uniqueness can be explained in a way similar to how usual non-uniqueness arises in conservation laws. The usual gas dynamics equations approximate the Navier-Stokes equations by eliminating the viscous effects. This ignores some of the physics of the problem and so introduces non-unique solutions that must be dealt with using the entropy selection criterion. A similar phenomenon occurs when we consider the nozzle problem. The one-dimensional nozzle equations approximate the three-dimensional Euler equations by radial averaging, once again reducing some of the physics of the problem. In the results presented below, we consider only initial conditions that give unique solutions.

6.3 Properties of Constructions J2P/J2N

In [3], Andrianov and Warnecke prove some general properties about the 0-wave curve representing the stationary discontinuity. They also proof existence criterion for the J2P

and J2N constructions shown above. While an existence theorem is not immediately important for our results, some intermediate results used in the proof will be helpful in developing criterion for when the one-dimensional model approximates the multi-dimensional solution.

We begin by stating a lemma from [3], that gives some properties of the 0-wave curve under particular circumstances.

Lemma 2. *Consider the stationary contact discontinuity wave described by (6.32)-(6.34). Denote the states connected by this wave by \mathbf{w}_0 and \mathbf{w}_1 . We assume that $u_1 \neq 0$ and $|u_1| \neq c$. If the discontinuity is evolutionary, then the following statements hold,*

1. *The 0-wave curve is strictly decreasing (increasing) in p if $u_1 > 0$ ($u_1 < 0$).*
2. *For increasing (decreasing) velocities and pressures u_0 and p_0 , the velocities and pressures u_1 and p_1 also increase (decrease) and vice versa.*
3. *Given constant states $\bar{\rho}, \bar{p} > 0$, we have that*

$$\begin{cases} \rho_0 \rightarrow \bar{\rho} \\ u_0 \rightarrow 0 \\ p_0 \rightarrow \bar{p} \end{cases} \Rightarrow \begin{cases} \rho_1 \rightarrow \bar{\rho} \\ u_1 \rightarrow 0 \\ p_1 \rightarrow \bar{p} \end{cases} \quad (6.40)$$

A proof of this lemma is given in [3] and summarized in Appendix B.

This lemma is now used to prove a theorem stating conditions on the left and right states that guarantee construction J2P to exist. We start with a definition given in [3].

Definition 9. Consider the Riemann problem for (6.18)-(6.20) with left and right states \mathbf{w}_L and \mathbf{w}_R . Let $\mathcal{W}_1(\mathbf{w}_L)$ denote the 1-curve fixed by the left state \mathbf{w}_L . We define the **left bounding 3-curve** to be the 3-curve that intersects $\mathcal{W}_1(\mathbf{w}_L)$ at $u = 0$. Further,

1. If $a_L < a_R$, let $\mathbf{w}_0 \in \mathcal{W}_1(\mathbf{w}_L)$ be such that $M_0 = 1$. Let \mathbf{w}_1 be the state with $M_1 < 1$ connected to \mathbf{w}_0 by the 0-wave. We define the 3-curve passing through \mathbf{w}_1 to be the **right bounding 3-curve**.
2. If $a_L > a_R$, we define U_1 to be the state with $M_1 = 1$ connected by a 0-wave to $\mathbf{w}_0 \in \mathcal{W}_1(\mathbf{w}_L)$ with $M_0 < 1$. We define the 3-curve passing through \mathbf{w}_1 to be the **right bounding 3-curve**.

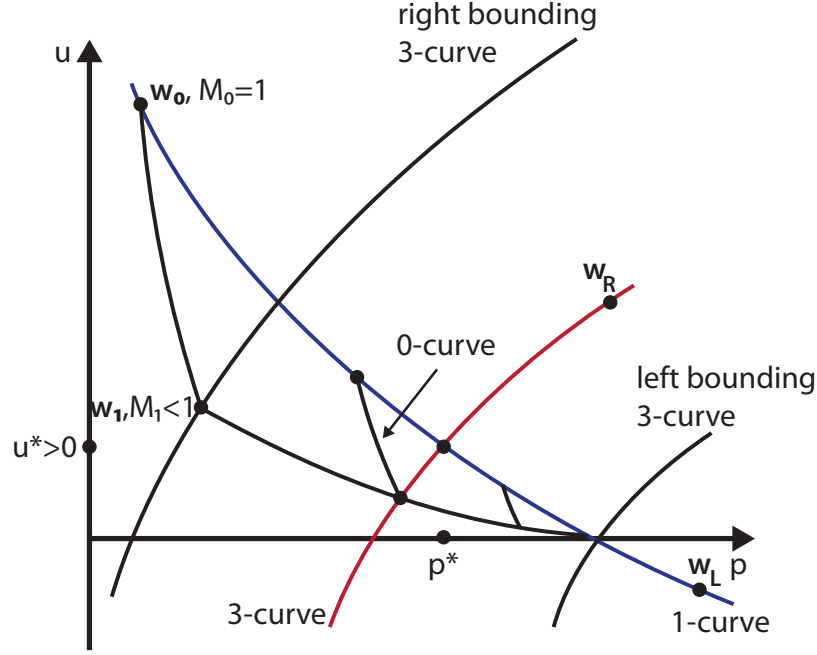


Figure 6.4: The left and right bounding curves for construction J2P and $a_L < a_R$.

These bounding curves are illustrated in Figure 6.4. The following theorem from [3] gives conditions for the existence of Construction J2P.

Theorem 4. *Consider the Riemann problem for (6.18)-(6.20) with left and right states w_L and w_R . Let (p^*, u^*) be the point of intersection between the 1-curve and 3-curve fixed at w_L and w_R respectively. If (p^*, u^*) lies between the left and right bounding 3-curve, and $u^* > 0$, then a solution of type J2P is possible.*

Proof. We begin by defining the curve,

$$S_1 = \{(p_1, u_1) | (p_1, u_1) \text{ are connected by 0-wave to } (p_0, u_0), \forall (p_0, u_0) \in \mathcal{W}_1(U_L)\}. \quad (6.41)$$

Note that all points on S_1 are defined implicitly by the following system,

$$\Gamma_1 := a_0 \rho_0 u_0 - a_1 \rho_1 u_1 = 0 \quad (6.42)$$

$$\Gamma_2 := \frac{p_0}{\rho_0^\gamma} - \frac{p_1}{\rho_1^\gamma} = 0 \quad (6.43)$$

$$\Gamma_3 := \frac{u_0^2}{2} + \frac{\gamma}{\gamma-1} \frac{p_0}{\rho_0} - \frac{u_1^2}{2} + \frac{\gamma}{\gamma-1} \frac{p_1}{\rho_1} = 0 \quad (6.44)$$

Since we assume that the state \mathbf{w}_0 lies on the differentiable curve $\mathcal{W}_1(\mathbf{w}_L)$, and $\rho > 0$, all Γ_i are differentiable with respect to their arguments $(\rho_1, u_1, p_1)^T$. By taking the Jacobian determinant of the system we find,

$$J = \left| \frac{\partial(\Gamma_1, \Gamma_2, \Gamma_3)}{\partial(\rho_1, u_1, p_1)} \right| = \frac{a_1}{\rho_1^\gamma} (c_1^2 - v_1^2). \quad (6.45)$$

Therefore, $J \neq 0$, except when \mathbf{w}_1 lies on the right bounding 3-curve, which is excluded by the assumption of the theorem. So S_1 will be a locally differentiable curve at every point (p_1, u_1) .

From Lemma 2, we see that the mapping $(p_0, u_0) \mapsto (p_1, u_1)$ is one-to-one. Since (p_0, u_0) lies on the 1-curve, which is strictly decreasing, S_1 will be strictly decreasing. Also, as the 1-curve approaches $(\bar{p}, 0)$, S_1 will approach $(\bar{p}, 0)$. The 3-curve is strictly increasing, so there will be a unique intersection point between the 3-curve and S_1 . Therefore we have constructed a solution of type J2P. \square

This theorem gives us a way to definitely know whether Construction J2P is possible, which is helpful when running numerical experiments. As shown below, the bounding curves will also be used to determine conditions on \mathbf{w}_L and \mathbf{w}_R for good approximation with the multi-dimensional solution. A similar theorem exists for Construction J2N.

Definition 10. Consider the Riemann problem for (6.18)-(6.20) with left and right states \mathbf{w}_L and \mathbf{w}_R . Let $\mathcal{W}_3(\mathbf{w}_R)$ denote the 3-curve fixed by the left state \mathbf{w}_R . We define the **right bounding 1-curve** to be the 1-curve that intersects $\mathcal{W}_3(\mathbf{w}_R)$ at $u = 0$. Further,

1. If $a_L < a_R$, let $\mathbf{w}_1 \in \mathcal{W}_3(\mathbf{w}_R)$ be such that $|M_1| < 1$. Let \mathbf{w}_0 be the state with $M_0 = -1$ connected to \mathbf{w}_1 by the 0-wave. We define the 1-curve passing through \mathbf{w}_0 to be the **left bounding 1-curve**.
2. If $a_L > a_R$, we define $\mathbf{w}_1 \in \mathcal{W}_3(\mathbf{w}_R)$ such that $M_1 = 1$. We define \mathbf{w}_0 to be the

state connected to \mathbf{w}_0 such that $|M_0| < 1$. We define the 1-curve passing through \mathbf{w}_0 to be the **left bounding 1-curve**.

Theorem 5. *Consider the Riemann problem for (6.18)-(6.20) with left and right states \mathbf{w}_L and \mathbf{w}_R . Let (p^*, u^*) be the point of intersection between the 1-curve and 3-curve fixed at \mathbf{w}_L and \mathbf{w}_R respectively. If (p^*, u^*) lies between the left and right bounding 3-curve, and $u^* < 0$, then a solution of type J2N is possible.*

Proof. The proof is analogous to the proof of Theorem 4. □

6.4 Results

Here we compare the one-dimensional approximation of the nozzle, with the multi-dimensional solution. It is important to note that we are not determining how well the junction conditions approximate the true physical solution, but how well they approximate the solution of the multi-dimensional equations. We assume that the solution of the multi-dimensional equations approximates the physical situation as much as desired. What we are trying to determine is under what conditions, the one-dimensional approximation matches with the multi-dimensional solution.

6.4.1 Numerical Methods

To determine the multi-dimensional solution for the nozzle, we use a conservation law package called CLAWPACK, developed by Randy LeVeque [55]. This package uses a second-order Godunov solver to solve two-dimensional problems in various geometries. For the nozzle problem, we use the fact that the pipe geometry is axisymmetric to consider the full three-dimensional problem in a two-dimensional domain by solving Equations (6.5)-(6.8). We consider the discontinuous nozzle geometry whose radius is described by,

$$R(x) = \begin{cases} R_L & x \leq 0 \\ R_R & x > 0 \end{cases}, \quad (6.46)$$

where R_L and R_R represent the constant radius on the left and right of the discontinuity. The discontinuous nozzle geometry is shown in Figure 6.5, for our main results. We also

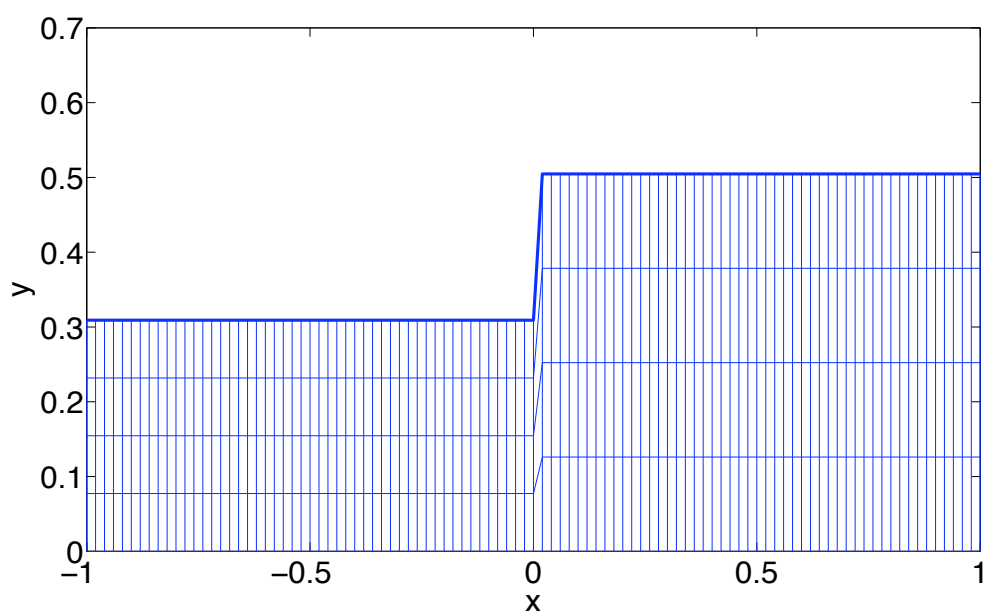


Figure 6.5: The discontinuous nozzle geometry.

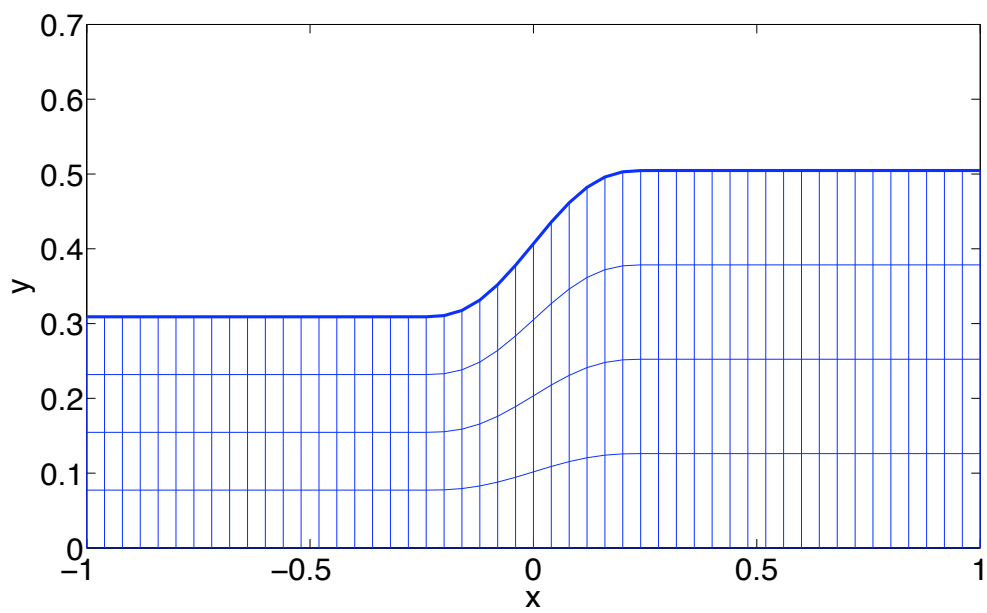


Figure 6.6: A smooth nozzle of width $\epsilon = .25$.

consider a nozzle of small width ϵ whose radius is described by,

$$R(x) = \begin{cases} R_L & x \leq -\epsilon \\ p(x; \epsilon, R_L, R_R) & -\epsilon < x \leq \epsilon, \\ R_R & x > \epsilon \end{cases} \quad (6.47)$$

where $p(x, \epsilon, R_L, R_R)$ is a fifth order polynomial in x that makes $R(x)$ twice differentiable. A smooth nozzle of width ϵ is shown in Figure 6.6. This geometry is used to show that the discontinuous nozzle solution is the limiting case as $\epsilon \rightarrow 0$. In the horizontal direction, $N = 200$ nodes were used, and in the vertical direction $M = 100$ nodes were used. A CFL number of .94 was also used.

To obtain the solution to the one-dimensional approximation, the constructive theory of Thanh [85] was implemented to determine the exact solution of the Riemann problem. We obtain the exact solution for the nozzle problem in a similar manner as for the usual Euler equations, with the addition of the stationary wave.

6.4.2 Nozzle Results

We begin by showing that the solution obtained by the discontinuous nozzle geometry is the limiting solution of a nozzle of width ϵ as $\epsilon \rightarrow 0$. We do this by examining the multi-dimensional solution with the geometry seen in Figure 6.6, for decreasing values of ϵ . We then compare this solution to the solution with the discontinuous geometry seen in Figure 6.5.

To run this comparison, we use Riemann initial conditions,

$$\begin{aligned} \rho_L &= 3 & \rho_R &= 1 \\ u_L &= 0 & u_R &= 0 \\ p_L &= 1 & p_R &= 1 \\ a_L &= 1 & a_R &= 1.5 \end{aligned}$$

and determine the solution at final time $T = 0.2$. We then radially average the axisymmetric solution to obtain one-dimensional result for ease of comparison. We see that as the width gets thinner, the solution approaches the discontinuous solution. Therefore, the discontinuous geometry is a limiting case of a physically realistic nozzle. For the

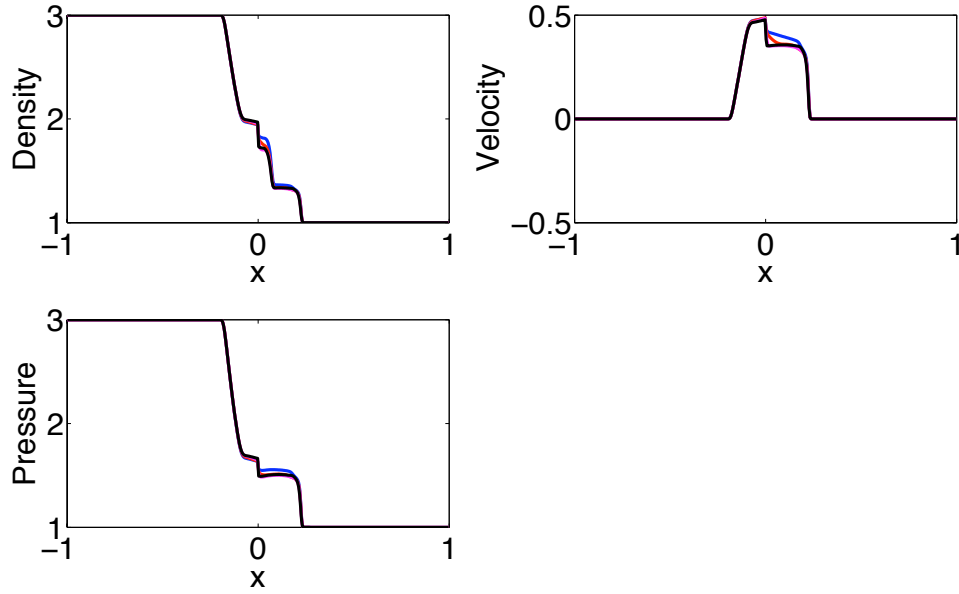


Figure 6.7: A comparison of the solution of the Riemann problem for nozzles of various widths ϵ . As $\epsilon \rightarrow 0$, the solutions converge to the discontinuous geometry solution.

results shown below we use the discontinuous geometry, as it lines up well with the one-dimensional equations. Figure 6.8 shows the error between the smooth nozzle and the discontinuous nozzle geometry for various values of ϵ .

We now compare the results of the one-dimensional approximation to the axisymmetric solution. In order to compare the solutions, we again take the axisymmetric solution and radially average it at each point x along the pipe. This gives a function of the axial direction only that can be compared with the one-dimensional solution. We desire to determine constraints for the initial conditions so that the one-dimensional solution approximates the axisymmetric solution well. We continue to use Riemann initial conditions.

Through numerical experimentation, we notice patterns when the solution is of type J2P or J2N. Recall the results from [3] that give conditions for the existence of such constructions, in terms of left and right bounding curves for either the 1-curve or 3-curve, depending on the construction. We look at two examples with solutions of type J2P, and vary the initial conditions so that the 1-curve and 3-curve intersect close and

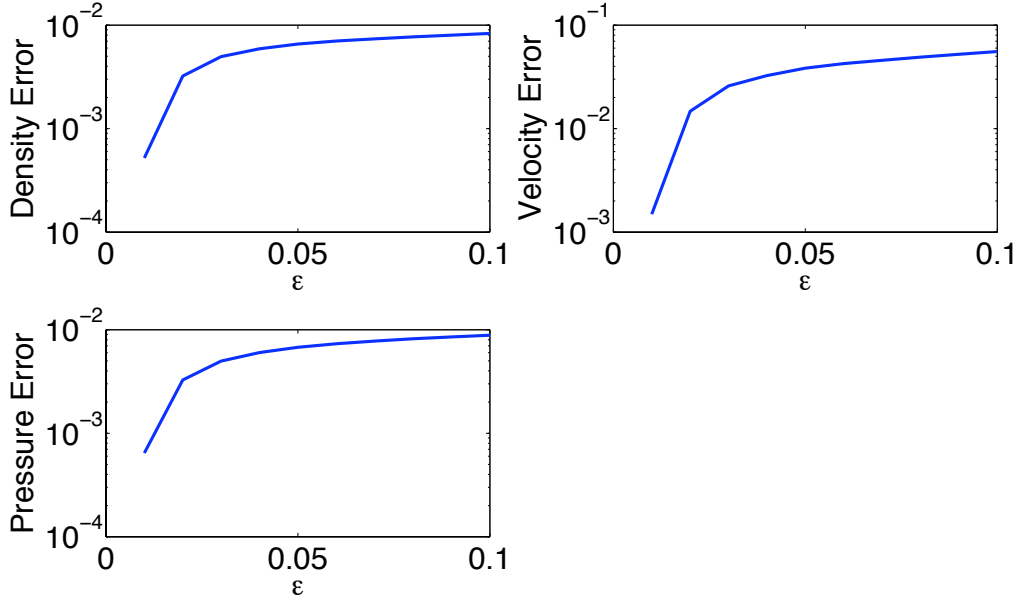


Figure 6.8: The relative error between the smooth nozzle and discontinuous nozzle for $\epsilon \in [.01, .1]$.

far away from the left bounding 3-curve.

We see in Figure 6.9 that the initial conditions are such that the intersection of the 1-curve and the 3-curve lie within the 3-bounding curves with $u^* > 0$. From the theory presented above, this tells us that construction J2P will be possible. We also see that the intersection is close to the left bounding curve. In Figure 6.9 at the bottom, we compare the one-dimensional and axisymmetric solutions. Since we know the construction type, we can obtain the exact solution to the one-dimensional problem. We can see that for these initial conditions, there is very good agreement between the one-dimensional and axisymmetric solutions. The intermediate states agree, as well as the shock speeds.

Next we consider a different set of initial conditions, whose results are shown in Figure 6.10. We see that the intersection of the 1-curve and 3-curve are far away from the left bounding curve for these initial conditions, but that construction J2P is still possible, since the intersection is between the left and right bounding curves. When we consider the comparison between the one-dimensional and radially averaged axisymmetric solution, we see that they do not agree well. Both the intermediate states and the shock speeds

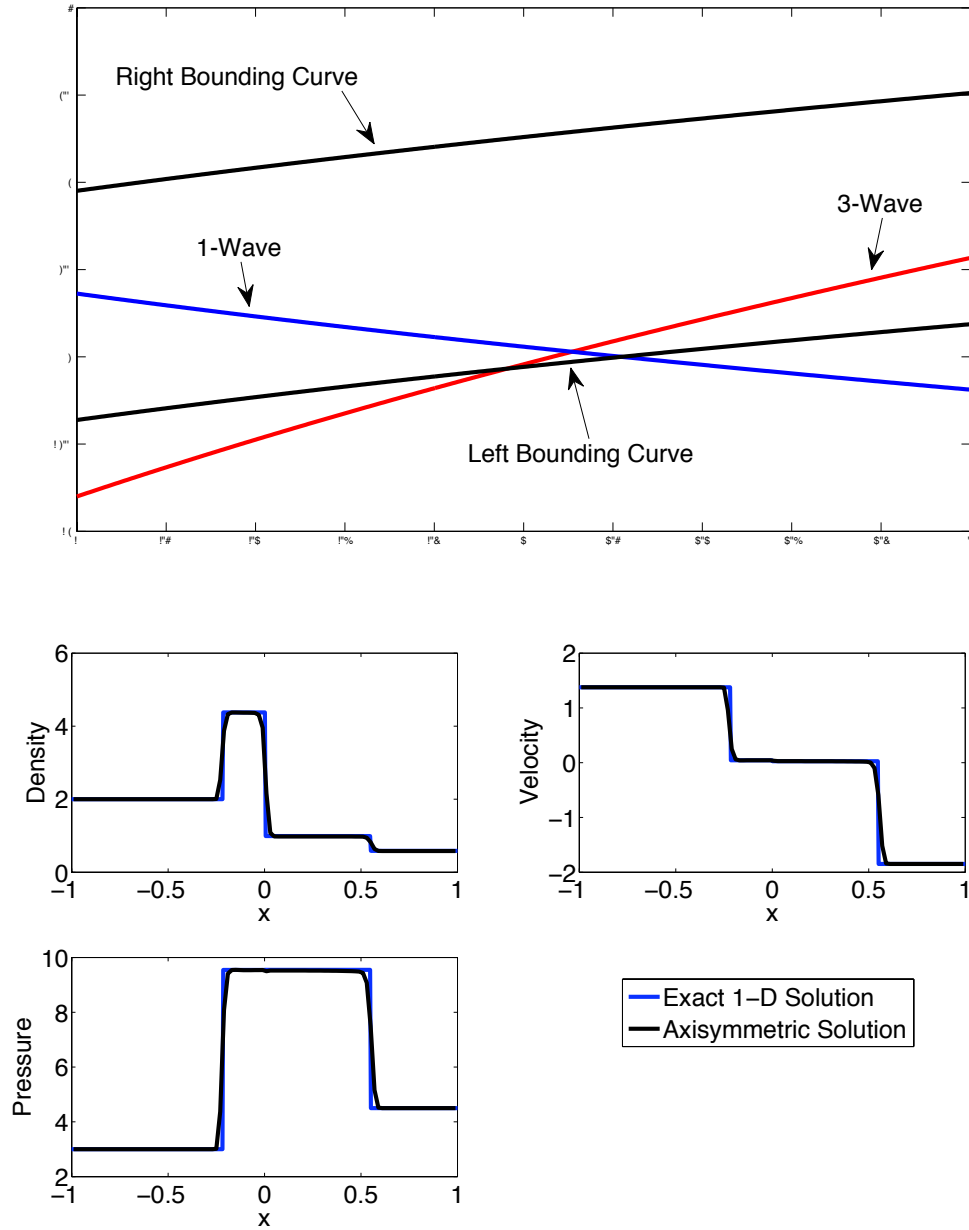


Figure 6.9: Result of initial conditions that give good agreement with multi-dimensional solution. Intersection of the 1- and 3- curves relative to the 3-bounding curves (Top). The exact solution to the one-dimensional problem is compared with the radially averaged solution of the multi-dimensional problem at time $T = .2$ (Bottom).

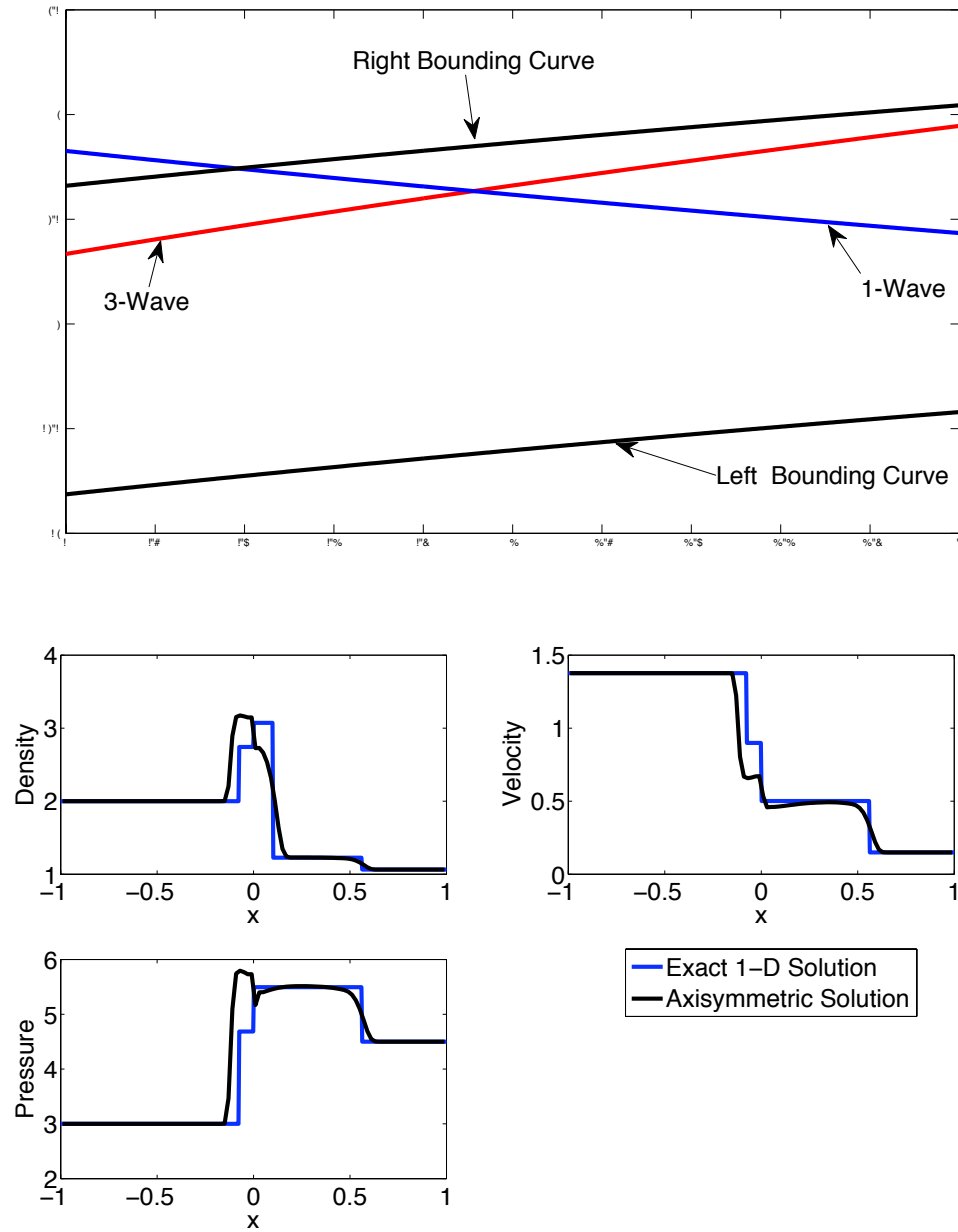


Figure 6.10: Result of initial conditions that give poor agreement with multi-dimensional solution. Intersection of the 1- and 3- curves relative to the 3-bounding curves(Top). The exact solution to the one-dimensional problem is compared with the radially averaged solution of the multi-dimensional problem at time $T = .2$ (Bottom).

Table 6.1: Results from varying the initial condition of the J2P construction. Average error can be bounded below the threshold error by setting initial conditions sufficiently close to the left bounding curve.

% between bounding curves	Average Relative Error
10%	6.09×10^{-2}
25%	5.52×10^{-2}
50%	8.21×10^{-2}
75%	1.05×10^{-1}
90%	1.33×10^{-1}

are different. Similar results hold for constructions of type J2N, using the corresponding bounding curves.

These results are used to determine if a set of initial conditions gives good agreement with the axisymmetric solution. This is demonstrated by testing multiple initial conditions and calculating the error in the solutions. We use the J2P construction for these trials. The left state and geometry are fixed at,

$$\rho_L = 1 \tag{6.48}$$

$$u_L = 1.25 \tag{6.49}$$

$$p_L = 2 \tag{6.50}$$

$$a_L = 1 \quad a_R = 1.5, \tag{6.51}$$

and the right state is varied such that the intersection of the 1-curve and 3-curve are a certain percentage of the distance between the left and right bounding curves. These results are shown in Table 6.1, listing from near the left bounding curve to far from the left bounding curve.

The L_1 error is calculated between the exact one-dimensional solution and the radially averaged axisymmetric solution at final time $T = .4$. Table 6.1 shows the average of the relative errors for the density, velocity and pressure. We have highlighted the error at 50%. This is designated as the threshold error, to show that closer to the left bounding curve the error is less, and farther from the left bounding curve the error is greater than the threshold. This threshold error is analogous to the minimum acceptable error for a

given problem.

We next examine the dependence of the solution on the geometry of the nozzle. Since the only degree of freedom for the discontinuous nozzle is the jump in area, we vary the magnitude of that jump and show how the solutions change. We consider only diverging nozzles, and keep the area of the left side equal to $a_L = 1$ and use the following initial conditions,

$$\begin{aligned}\rho_L &= 2 & \rho_R &= 1 \\ u_L &= -.17 & u_R &= .8\end{aligned}\tag{6.52}$$

$$\begin{aligned}p_L &= .5 & p_R &= 2\end{aligned}\tag{6.53}$$

which admits a solution of type J2N.

We begin with a control case of a constant area nozzle, that is a straight pipe, as seen in Figure 6.11. We see that the one-dimensional code agrees well with the multi-dimensional solution, as we expect. Next we consider a 20% jump in area, shown in Figure 6.12. We begin to see deviations, but there is still good agreement. Finally we consider a 200% jump in area, Figure 6.13. We now once again see large discrepancies between the two solutions.

We list the average relative errors for various nozzle geometries in Table 6.2. Initial conditions (6.52) are used and the right area is varied. A right area of $a_R = 1.5$ is set as the threshold. For all area jumps greater than 50% we see that the error is greater than the threshold error, and for jumps less than 50%, the error is less than the threshold.

Finally we briefly examine the results of the other two construction types not yet mentioned, J1 and J3. These constructions require the data to be supersonic in some way. The initial conditions for the J1 construction are,

$$\begin{aligned}\rho_L &= 2 & \rho_R &= 1 \\ u_L &= 1.25 & u_R &= 1.2 \\ p_L &= 1 & p_R &= 2 \\ a_L &= 1 & a_R &= 1.5,\end{aligned}$$

and the results are plotted in Figure 6.14. The initial conditions for the J3 construction

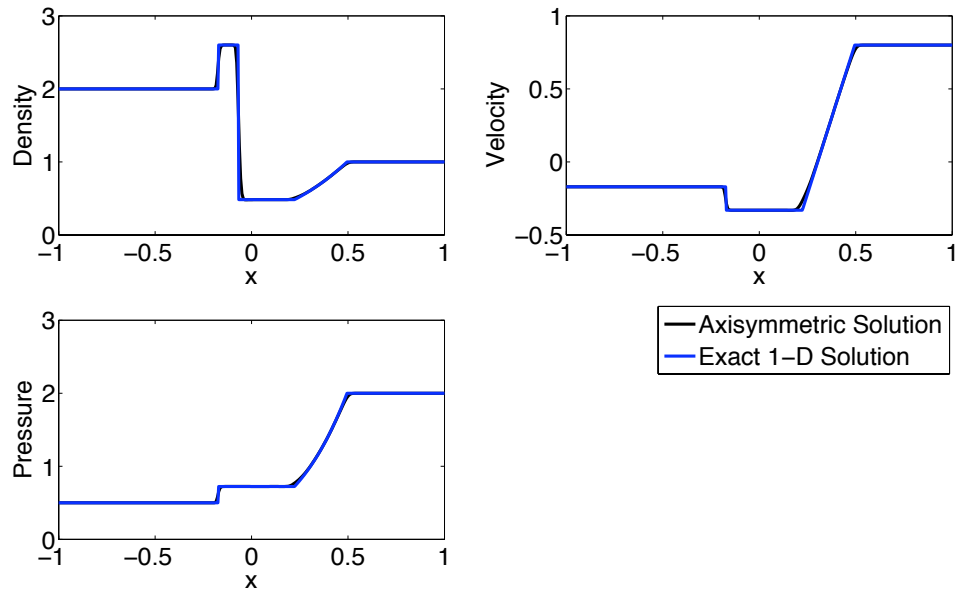


Figure 6.11: Results of the straight pipe geometry, $a_L = a_R$.

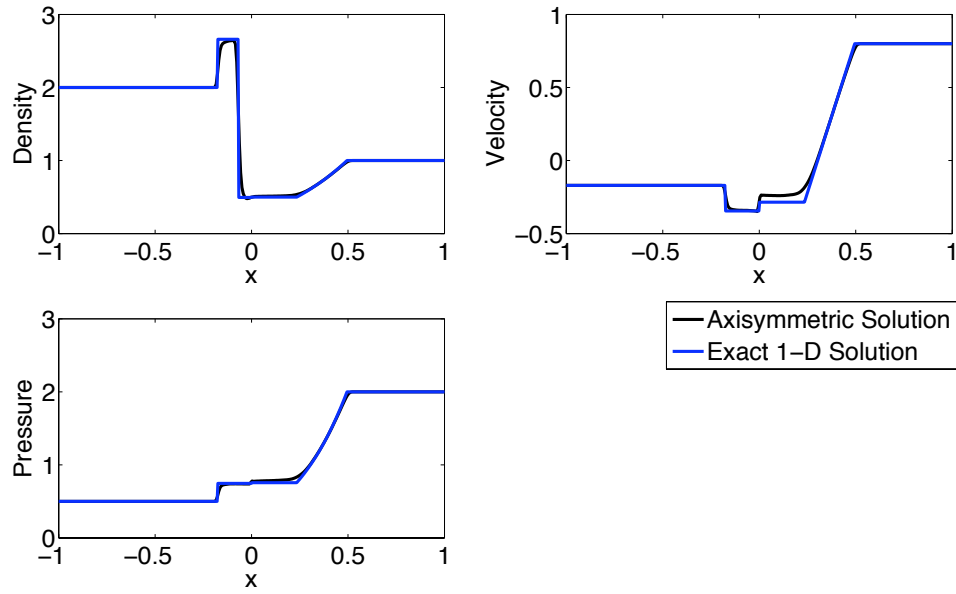


Figure 6.12: Results of a discontinuous nozzle with 20% jump in area.

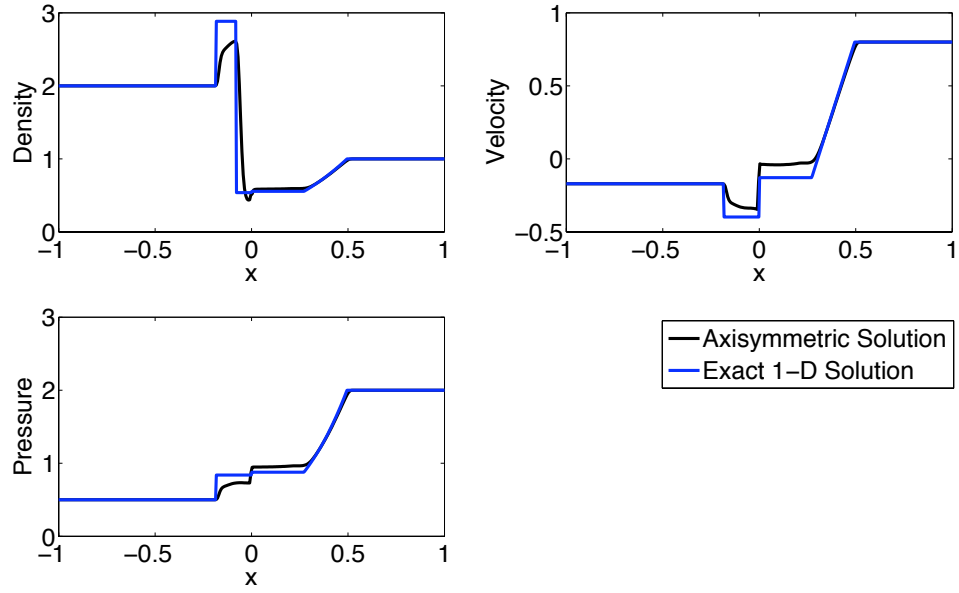


Figure 6.13: Results of a discontinuous nozzle with a 200% jump in area.

Table 6.2: Results from varying the geometry of the nozzle. Average error can be bounded below the threshold error by setting the jump in area sufficiently small.

Area Jump	Average Relative Error
10%	3.12×10^{-2}
20%	4.57×10^{-2}
50%	6.31×10^{-2}
100%	9.19×10^{-2}
200%	1.22×10^{-1}
400%	1.67×10^{-1}

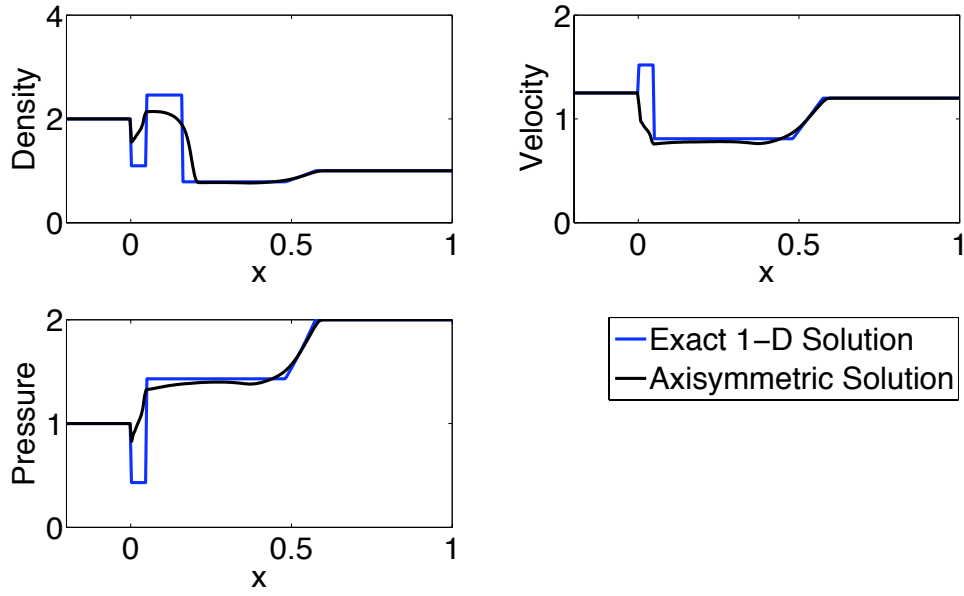


Figure 6.14: Results for J1 construction.

are,

$$\begin{aligned}
 \rho_L &= 1 & \rho_R &= 2 \\
 u_L &= 1.25 & u_R &= -3 \\
 p_L &= 2 & p_R &= 3 \\
 a_L &= 1 & a_R &= 1.5,
 \end{aligned}$$

and the results are plotted in Figure 6.15.

We see from the results that there is large disagreement between the one-dimensional and axisymmetric solutions when considering the J1 and J3 constructions. This holds true for all initial conditions that result in those construction types, as far as we have observed.

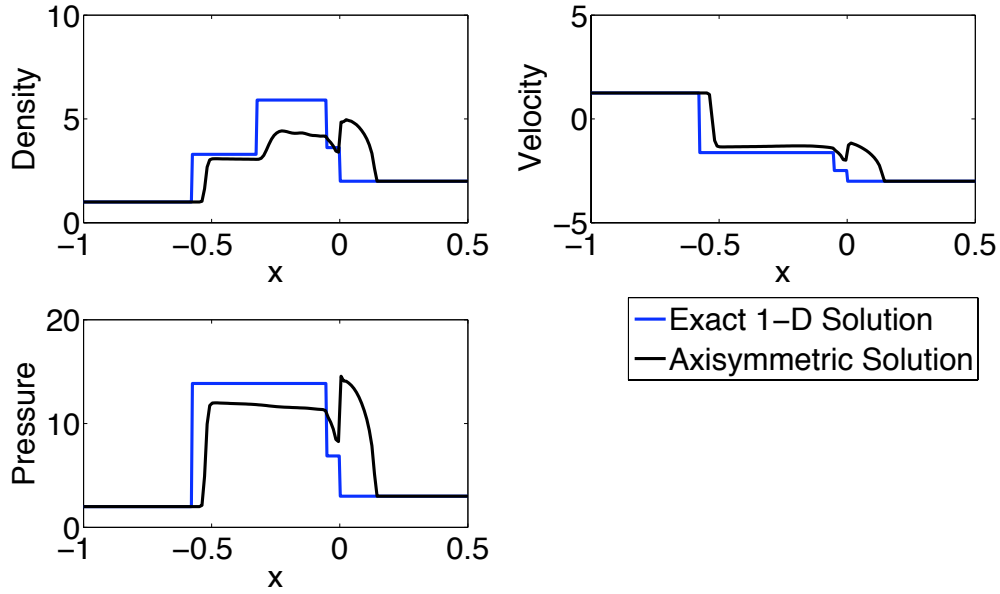


Figure 6.15: Results for J3 construction.

6.5 Conclusions

We see from the work done in [3, 85] which is reiterated above, that the nozzle junction can be analyzed from a mathematical viewpoint. This is not true of most junction types. As we see below, for other junctions many approximations derived from empirical data must be employed to model the junction. These approximation limit the amount of pure analysis that can be done to the model. With the nozzle model we can, and in fact do, determine the exact solution of the one-dimensional equations. We use this solution to determine under what conditions the one-dimensional equations approximate the axisymmetric solution well. The theory developed in [3] is employed to determine what initial conditions give a good approximation. Also, through numerical experiments, we see that the approximation gets worse as the jump in the nozzle increases. This makes intuitive sense, since as the jump in the nozzle increases, there exists more multi-dimensional geometry that is not fully taken into account by the one-dimensional equations. These trends can help in determining if the one-dimensional approximation gives sufficient accuracy for the needs of the problem. If a threshold error is given, once the initial conditions

and geometry are found that attain that error, the observations above can be used to determine if a set of initial conditions and geometry give error less than the threshold. This works for the J2P and J2N constructions only. From results we see that the J1 and J3 constructions do not give a good approximation to the axisymmetric solution. However, certain applications such as engine manifold assume subsonic flow [6], and so solution are of J2P or J2N type.

Chapter 7

Numerical Investigation of Gas Flow through a Splitting Junction

7.1 Introduction

In this chapter we study a junction of the form shown in Figure 7.1. In its most general case, there can be any number of edges coming into or going out of the junction, and the angles between edges can vary as well. There are many applications for such a junction. Some of the main ones studied are traffic flow, blood flow and the case studied here, gas flow. Traffic flow is a unique case among the three, as it is a true one-dimensional, hyperbolic model. In the case of blood or gas flow, the one-dimensional models approximate multi-dimensional effects. Also in those models, their multi-dimensional counterparts are hyperbolic approximations of more complicated models which involve viscous terms.

The application we study here is separating gas flow in a three pipe junction. Such a junction is shown in Figure 7.2. This type of junction offers many degrees of freedom for the geometry. We see that we can modify the angle of the two outlet pipes with the horizontal, as well as all the pipe areas. These degrees of freedom, as well as the fact that the geometry is no longer axisymmetric, make this junction much more difficult to model than the nozzle, both in the multi-dimensional and in the one-dimensional sense. Generic junctions such as this are studied in [5]. Multi-pipe junctions, such as seen in Figure 7.1 can also be modeled. This is done by Bassett in [6]. Here we focus on the three pipe junction as the majority of the modeling problems can be seen in this situation, while simplifying the computation.

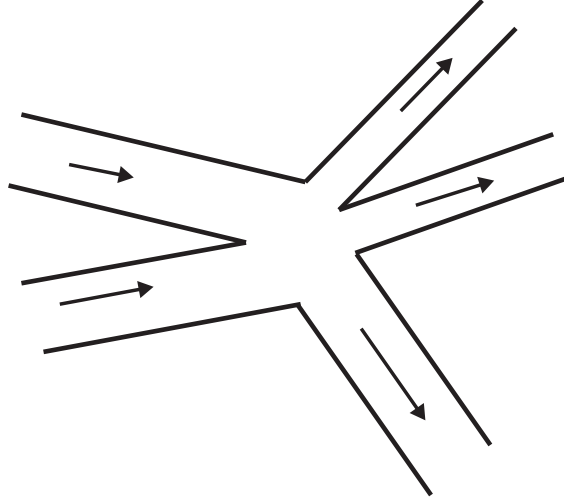


Figure 7.1: A generic multi-edge pipe junction with inflow and outflow.

We make certain simplifying assumptions on our geometry, such as assuming that the bifurcation angles and areas of both outlet pipes are the same, that is,

$$\theta_2 = \theta_1 \quad a_3 = a_2. \quad (7.1)$$

This simplified geometry is helpful when computing the multi-dimensional solution, as the problem domain is easy to model computationally. Many of the results in this work can be applied to a junction such as Figure 7.2, if a multi-dimensional solution could be easily calculated for that geometry. While junction conditions for the nozzle were determined neatly from the dimensional averaging of the multi-dimensional equations, this can not be done here, as the geometry is not axisymmetric. We therefore use junction conditions that are determined from physical considerations and experimental data. As done for the nozzle, we compare the results of the one-dimensional solution with the multi-dimensional solution, to determine how well the junction conditions approximate the effects of the geometry.

7.1.1 Previous Work

Much work has been done for junctions of this type. In [31, 37], a traffic model is introduced and analyzed for such a junction. This application is a good example of

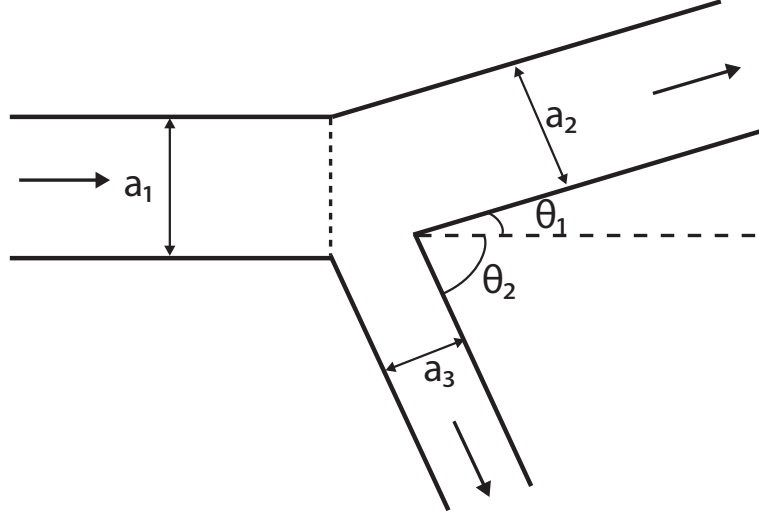


Figure 7.2: A generic splitting junction with three pipes. All pipe areas can be different and two angles made by outflow pipes can be different.

a purely one-dimensional hyperbolic model. That is, there is not higher dimensional traffic flow model that is approximated by a network using dimensional averaging. The junction conditions for such models involve maximizing a function of the flow across the junction, and assuming that all shocks propagate away from the junction. Under the given junction conditions, a solution to the Riemann problem is shown to exist and its properties are analyzed. In [22, 23], the Circle of Willis is modeled as a blood flow network. Dimensional averaging techniques are used on the incompressible Navier-Stokes equations to obtain the governing equations within the vessels. For junction conditions, continuity of pressure and conservation of flow are used.

For gas flow through a junction, the work has been done in two different veins, analytical and physical. The purpose of both directions is the same, however; to determine suitable junction conditions where the pipes meet. In [15, 16], a general framework is developed to define the Riemann and Cauchy problem for a general multi-junction. Well-posedness is then proved for the Cauchy problem. The junction conditions used in this model are derived from physical principles. In [4], conditions are imposed at the junction such that shocks propagate away from the junction, and the flow is maximal at the junction. Using these conditions, existence of solutions to the Riemann problem is shown. In these more analytical works, junction conditions are chosen such that suitable

mathematical properties of the solution can be proved. However, those junction conditions are difficult to implement in practice, and no validation against experimental or multi-dimensional data is given.

In the physical or modeling based works, junction conditions are chosen based upon their agreement with experimental data. An application of pipe junction models that makes great use of one-dimensional network approximations is engine manifold modeling. One-dimensional approximations are particularly important as the testing of engine manifolds require running multiple different designs for long times to attain the desired data. One of the first works considering junction conditions was Benson [8], where the constant pressure conditions described below was presented. In [5, 6, 20], more complicated pipe junction models are considered. The junction conditions are based purely on physical considerations. Particularly, in [5] a pressure loss condition is implemented that depends upon many assumptions of the flow which are derived through experimental observation. The model is then compared with experimental junction data. In this work we will use junction conditions from both approaches to the problem, and compare them.

7.1.2 Overview

Here, we consider simple separating flow through a three-pipe junction. We simulate this flow with both one-dimensional and two-dimensional code. For the network code, we use junction conditions common to all network models of gas flow, conservation of mass and energy. We also use various pressure conditions from different works. The solution of the two-dimensional model is considered, and data from its solution is used to modify the junction conditions to obtain a better fit.

We then compare the various one-dimensional models with the two-dimensional solution. The initial conditions and the geometry of the problem are varied to determine their affect on the error in the one-dimensional model.

7.2 Split Junction Conditions

We now consider the junction conditions for a splitting junction between three pipe sections. Recall that in the fully general case, there are many geometric parameters that can be changed, and that we make certain assumptions to simplify the calculations and reduce the number of geometric parameters. Because of these assumption, we know

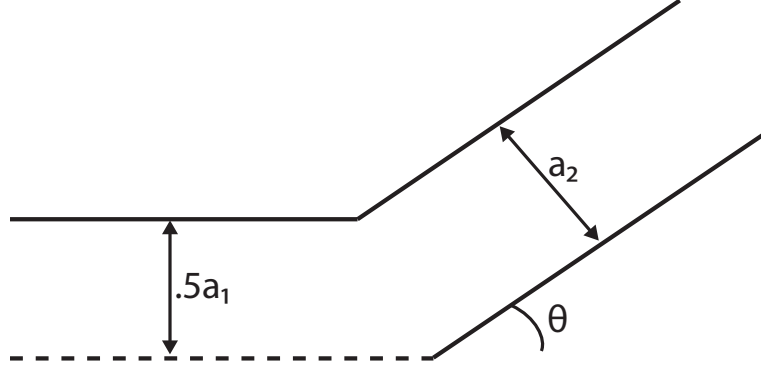


Figure 7.3: Top portion of the splitting junction domain.

that the geometry is symmetric across the center line of the left pipe. This allows us to simplify our model by considering only the geometry above that center line, assuming that all state variable are symmetric about it, except for the vertical velocity v , which is skew-symmetric. The geometry that we model after these assumptions are made is shown in Figure 7.3.

Unlike the nozzle, where junction conditions are incorporated into the differential equations by dimensional averaging, the junction conditions for a split must be imposed as boundary conditions at the edge of each pipe. The computation is thus separated into two separate domains, one for each pipe in our calculations, and boundary conditions are imposed where those pipes meet. As mentioned, one-dimensional approximation of pipes is used often in engine modeling. Therefore, two of the pressure conditions we use are those developed for engine models. A third conditions is used which is shown in [15, 16] to give well-posedness to the problem. An assumption used in engine models that we adopt here is that the flow is always positive subsonic through the junction. This makes physical sense for engine models, as it is expected that gas flows in one direction only, and should never be supersonic. This also helps numerically when setting boundary conditions, as it allows us to know *a priori* how many conditions are needed and which characteristics need to be set.

7.2.1 Splitting Pipe Junction Conditions

From the assumption made above, we know that three junction conditions are needed. There are two conditions that are generally imposed for a split junction in such models [6], the first is conservation of mass,

$$\rho_1 u_1 a_1 = 2\rho_2 u_2 a_2 \quad (7.2)$$

where a_i is the area of the pipe. The second condition, introduced by Corberàn [20], says that the total enthalpy of each outgoing pipe must be equal to the mass-averaged total enthalpy of the incoming pipes. For our three pipe junction, this reduced to,

$$\frac{E_1 + p_1}{\rho_1} = \frac{E_2 + p_2}{\rho_2}. \quad (7.3)$$

It is interesting to note that condition (7.2) combined with condition (7.3), gives conservation of energy for our junction,

$$a_1 u_1 (E_1 + p_1) = 2a_2 u_2 (E_2 + p_2). \quad (7.4)$$

The final condition that is imposed relates to the pressure in each pipe, and depends upon the model. There are three models used in this work.

Constant Static Pressure

The first pressure condition was proposed by Benson [8], and imposes continuity of pressure throughout the junction, that is, the static pressure is equal in all pipes at the point where they meet,

$$p_1 = p_2. \quad (7.5)$$

For the three pipe junction we consider here, this is equivalent to imposing that the static pressure at the junction is equal to the average of the static pressures in all three pipes. While this model has the obvious disadvantage of not incorporating any information about the geometry of the junction, it has been proved to work reasonably well when compared to experimental data [20].

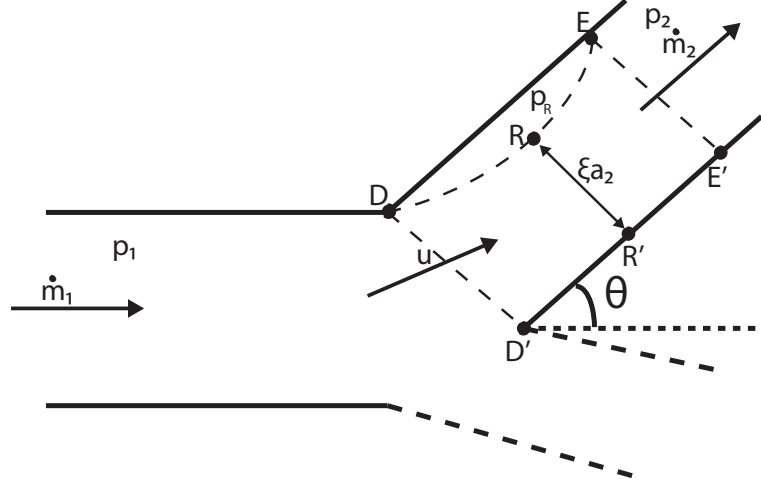


Figure 7.4: Diagram of the physics modeled by the pressure loss junction condition.

Pressure-Loss Model

The second pressure model is called the pressure-loss junction model. This name is used for many different variations, however, the idea is to incorporate some information from the junction, either through experimental steady state data or through analysis, to determine the drop in pressure across the junction. The model we implement was developed in [5], and uses analytical techniques to relate the pressure loss to the mass flow rate and geometrical properties of the pipe. There are multiple different formulas, depending on the flow situation.

We begin by considering the flow through our particular geometry, as seen in Figure 7.4. The assumptions and derivation for this model are obtained from [5]. The first and most inaccurate assumption for gas flow is that the flow is incompressible. This assumption is necessary to obtain a simple relationship between the pressure loss and the geometry of our junction, and it is shown in [5] that this junction condition works well when compared to experimental data. We also note that the incompressibility assumption holds relatively well for gas flow with low Mach number.

It is further assumed that as the flow enters the pipe junction, it separates from the pipe wall, as seen in Figure 7.4. As the flow separates it effectively restricts the area in the outgoing pipe. The final assumption has to do with the direction and magnitude of the velocity entering the outgoing pipe. Following [5], the magnitude of the velocity is

assumed to be equal to the velocity of the incoming pipe, u_1 . According to experimental observations noted in [35], the direction of the velocity has an angle of $\theta/4$ with the horizontal.

The derivation for this model is done in [5, 6] and is summarized in Appendix C. The relationship between the pressures on either side of the junction is given by,

$$\frac{p_1 + \frac{1}{2}\rho_1 u_1^2 - (p_2 + \frac{1}{2}\rho_2 u_2^2)}{\frac{1}{2}\rho_1 u_1^2} = q^2 \psi^2 + 1 - 2q\psi \cos \left[\frac{3}{4}(\theta) \right]. \quad (7.6)$$

where $q = \frac{a_2 \rho_2 u_2}{a_1 \rho_1 u_1}$ is the ratio of mass fluxes, and $\psi = \frac{a_1}{a_2}$ is the ratio of pipe areas. Equation (7.6) can be simplified by including the assumption of mass conservation, giving,

$$\frac{p_1 + \frac{1}{2}\rho_1 u_1^2 - (p_2 + \frac{1}{2}\rho_2 u_2^2)}{\frac{1}{2}\rho_1 u_1^2} = \frac{1}{4}\psi^2 + 1 - \psi \cos \left[\frac{3}{4}(\theta) \right]. \quad (7.7)$$

This model obviously makes many assumptions that do not hold exactly for all situations, however it is proven to work well in experimental cases, for both steady and unsteady flows [5, 6]. Also, as we see below, this model does a better job of approximating the two-dimensional solution under certain geometries.

Continuity of Total Pressure

The final junction condition considered is continuity of total pressure, or stagnation pressure. This is given by the following equation,

$$p_1 + \frac{1}{2}\rho_1 u_1^2 = p_2 + \frac{1}{2}\rho_2 u_2^2. \quad (7.8)$$

This junction condition is used because it is determined for purely mathematical reasons. In [15], an example is given where the constant static pressure condition leads to ill-posedness. Therefore, a junction condition was developed that incorporated some of the geometrical features of the split. While it is obvious that linear momentum is not conserved across this junction, the condition proposed to conserve a component of the linear momentum, and the choice of the component would depend on the geometry of the pipes. Let $\hat{\nu}_i$ be the unit vector point along each of the three pipes away from the junction. The junction condition is chosen by letting the component of the linear

momentum orthogonal to $\hat{\nu}_1 + \hat{\nu}_2 + \hat{\nu}_3$ be conserved, that is,

$$\sum_{i=1}^3 (p_i + \frac{1}{2} \rho_i u_i^2) \hat{\nu}_i \cdot \left(\alpha \sum_{i=1}^3 \hat{\nu}_i \right)^\perp = 0 \quad \forall \alpha \in \mathbb{R}. \quad (7.9)$$

It is shown in [16] that condition (7.9) along with conservation of mass and energy, and certain other technical conditions, gives a well-posed solution to the Cauchy problem.

To simplify condition (7.9), in [16], the following conditions is introduced; for some positive total pressure P_* ,

$$p_i + \frac{1}{2} \rho_i u_i^2 = P_* \quad , i = 1, 2, 3. \quad (7.10)$$

It was then shown that condition (7.10) implies condition (7.9). This is where we see that the conditions developed from an analytical standpoint are difficult to implement, as we have no value for P_* . For our purposes we set P_* equal to the average of the total pressures of all three pipes, which gives our original condition (7.8).

7.3 Results

We consider the Riemann problem defined on a splitting junction geometry. The discontinuity in the initial conditions is set in the incoming pipe, thus creating a wave that travels towards the junction. This is done for both the one-dimensional and two-dimensional problems. Since it is difficult to compare data within the junction itself, as the geometries will not line up perfectly between the one and two-dimensional case, we compare the results at the outlet of the outgoing pipe.

In addition to considering the accuracy of the one-dimensional solution at the pipe outlet, we also consider the accuracy of the junction conditions. We use the two-dimensional solution to determine how accurate the junction conditions are in approximating the true solution.

7.3.1 Numerical Considerations

When implementing the one-dimensional network code, no special considerations are necessary. The normal one-dimensional Euler gas dynamics equations are solved on two domains, each representing a pipe in the junction. The domain of the one-dimensional

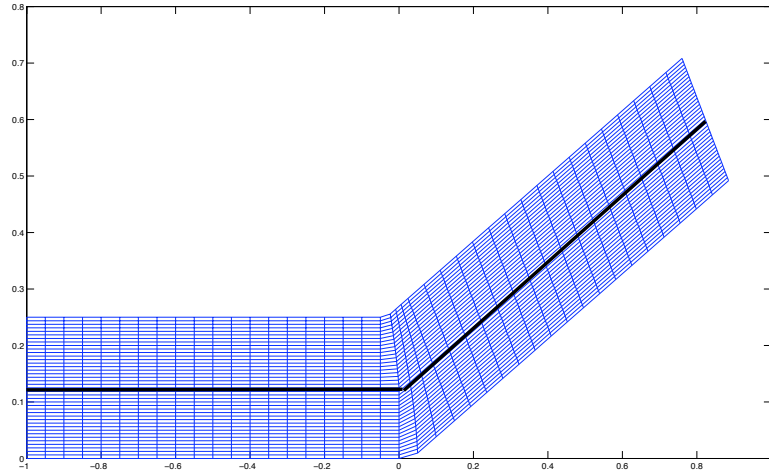


Figure 7.5: Mesh used to simulate a splitting junction for the two-dimensional solution. Black line denotes where one-dimensional domains lies on the mesh.

model represents the center line of each pipe, as shown in Figure 7.5. Standard zeroth order boundary conditions are imposed on the non-junction boundaries. At the junction, the various junction conditions are imposed using the typical method of determining the known characteristics from previous data and setting the unknown characteristics from the junction conditions. Since we choose our initial conditions such that the flow is positive subsonic, we know that there are three characteristic variables that must be set at the junction, giving a well-posed system. On each edge $N = 200$ nodes are used, and a CFL number of 0.75 is given.

To determine the two-dimensional solution, we use the package CLAWPACK. Special boundary conditions at the junction are not needed since the geometry models the junction itself, however; care must be taken in setting the mesh to correctly model the geometry. Figure 7.5 shows the mesh that is used in this model. Across the entire domain, 100 nodes are used in both the horizontal and vertical directions, and a CFL number of 0.94 is given.

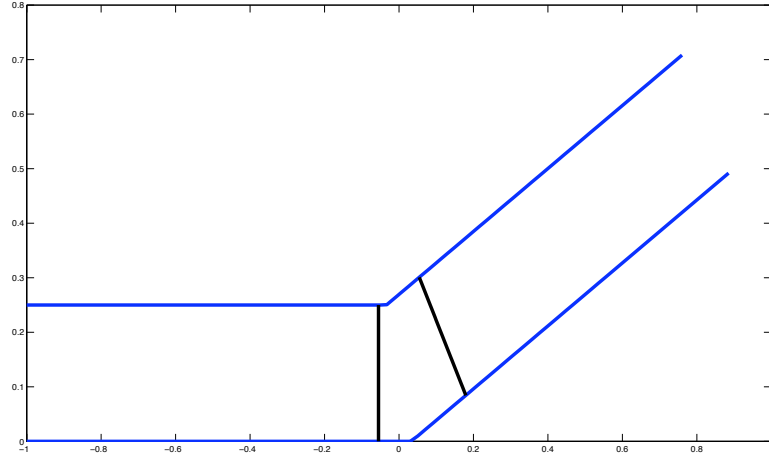


Figure 7.6: Lines used to denote where the junction is in the two-dimensional domain. State variables are averaged over these lines and compared.

7.3.2 Error Computation

There are two kinds of error computations presented below, ones for verifying junction conditions, and ones for comparing the one and two-dimensional models with each other. When verifying the junction conditions, we consider the two-dimensional solution to see how well it satisfies the junction conditions used in the network model. To check this, we look at the solution along the two lines shown in Figure 7.6. These lines represent the left and right side of the junction. The state variables are averaged along these lines so that their values at either end of the junction can be compared.

The second type of error is for when we compare the various network models with the two-dimensional solution. When comparing these solutions, we look only at the solution at the outlet, that is at the right boundary of the right pipe. We radially average the two-dimensional solution at the outlet of the right-hand pipe, and compare it with the value of the one-dimensional solution at the right boundary. We compute the relative error by,

$$E(t) = \frac{|\mathbf{q}_{1D} - \mathbf{q}_{2D}|}{|\mathbf{q}_{2D} + \epsilon|} \quad (7.11)$$

The term of ϵ is a small value inserted to avoid dividing by zero.

Finally, there are situations when, for simplicity, we wish to calculate a single number to represent the error over a span of time. To do this, we take the average of the error data over that time. So that the time dependent information is not totally lost, the standard deviation of the error data is also calculated in these cases, and shown in the plot as error bars.

7.3.3 Split Results

The first results we present in this section involve the accuracy of the junction conditions. We consider how well the following five quantities or conditions are satisfied by the two-dimensional solution:

$$a_1 \rho_1 u_1 = 2a_2 \rho_2 u_2 \quad (\text{Conservation of mass}) \quad (7.12)$$

$$a_1 u_1 (E_1 + p_1) = 2a_2 u_2 (E_2 + p_2) \quad (\text{Conservation of energy}) \quad (7.13)$$

$$\frac{E_1 + p_1}{\rho_1} = \frac{E_2 + p_2}{\rho_2} \quad (\text{Continuity of enthalpy}) \quad (7.14)$$

$$p_1 = p_2 \quad (\text{Continuity of pressure}) \quad (7.15)$$

$$p_1 + \frac{1}{2} \rho_1 u_1^2 = p_2 + \frac{1}{2} \rho_2 u_2^2. \quad (\text{Continuity of total pressure}) \quad (7.16)$$

The subscripts 1 and 2 represent the left and right pipes respectively and Figure 7.6 shows exactly where on the left and right pipe these quantities were measured. We consider the following Riemann initial conditions and geometry,

$$\rho_L = 1 \quad \rho_R = 1 \quad (7.17)$$

$$u_L = .5c_L \quad u_R = 0$$

$$p_L = 1 \quad p_R = 1$$

$$\theta = 30^\circ \quad \psi = 2,$$

where $\psi = \frac{a_1}{a_2}$. Figure 7.7 shows a plot of the relative error of the five conditions (7.12)-(7.16). We first note that the pressure conditions (7.15)-(7.16) are satisfied in the two-dimensional solution. We also see that the continuity of enthalpy is satisfied. However, the conservation of mass and energy conditions do not hold well in the two-

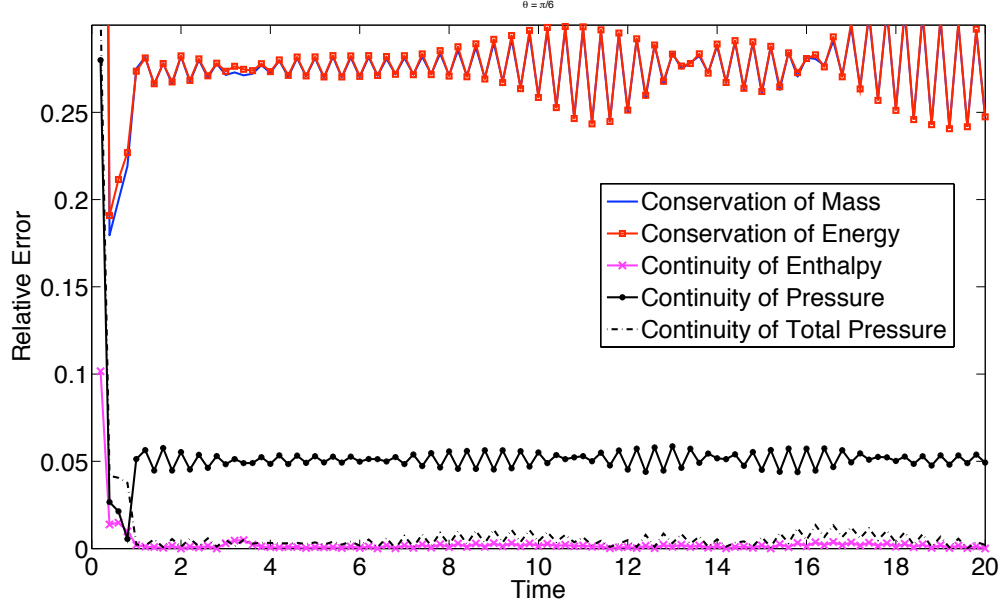


Figure 7.7: Plot of the error in junction conditions for the two-dimensional solution using initial conditions and geometry (7.17).

dimensional solution. These two conditions are fundamental to all the junction conditions listed above.

It might seem unusual that mass is not conserved throughout the junction. This can be explained by Figure 7.8. This is a plot of the full two-dimensional solution at a fixed time. The two ends of the junction are denoted by the black lines. We can see that there is a change in the density within the junction. This shock is stationary throughout the solution time, and is what gives rise to the lack of mass conservation in our calculations. If we were to take a smaller area for our junction, we would conserve mass better. As the junction reduces to a point, such as it does in the one-dimensional model, mass would be conserved exactly. Thus the reason why conservation of mass is often used as a condition for network models.

It can be readily seen by numerical experiment that under no conditions or geometries is mass conserved by the two-dimensional solution. Therefore, we consider a modified method for the network model, where the conservation of mass condition is replaced by a condition that better models the two-dimensional solution. We use a condition of the

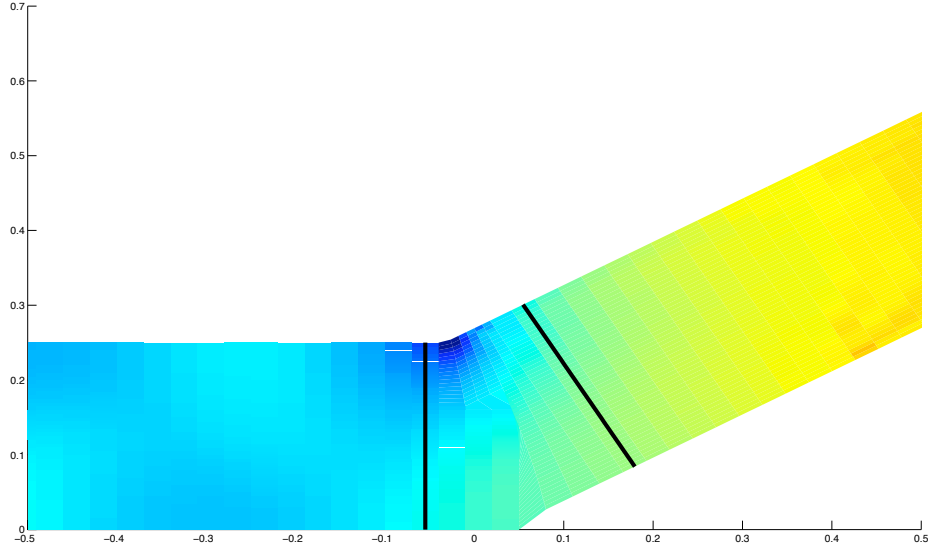


Figure 7.8: Full two-dimensional solution of the density at the junction.

following form:

$$a_1 \rho_1 u_1 = \frac{1}{\alpha} a_2 \rho_2 u_2 \quad (7.18)$$

where α must be determined approximately from the two-dimensional solution, our version of “experimental” data.

We first note that the value of α is roughly independent of the initial conditions of the problem. This is determined through multiple trials with various initial conditions. Therefore, α is determined mainly by the geometry of the junction. Furthermore, for simplicity we assume that α does not depend on the area ratio ψ . So we have that $\alpha = \alpha(\theta)$ is a function of the angle alone.

To determine the function $\alpha(\theta)$, we consider a problem with the initial conditions (7.17), but vary the angle θ from 10° to 75° . We run this problem to final time $T = 20$ and calculate the mass flow ratio of the junction,

$$\varphi(t) = \frac{a_1 \rho_1 u_1}{a_2 \rho_2 u_2} \quad (7.19)$$

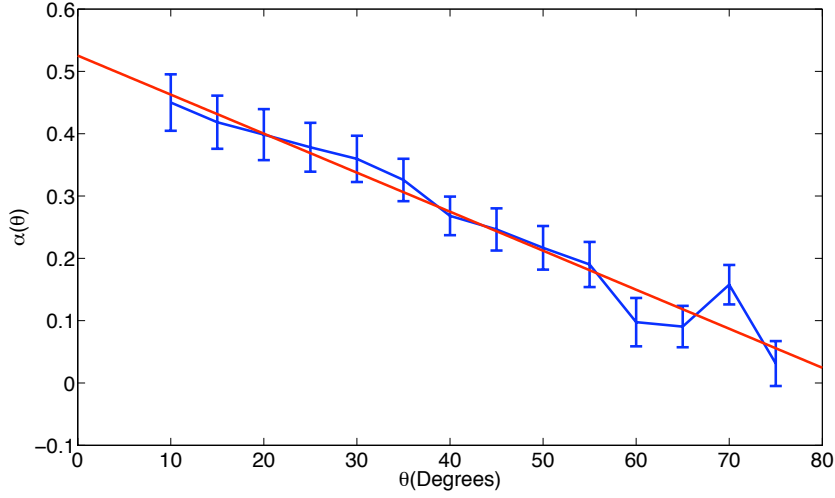


Figure 7.9: Plot of the average mass flow ratio over time with error bars determined by standard deviation. Linear fit is used to determine function $\alpha(\theta)$.

where the state variables at the ends of the junction are calculated as above. The ratio $\varphi(t)$ gives a time dependent function which approximates $\alpha(\theta)$. Figure 7.9 shows the average value over time of this ratio as a function of θ , along with the standard deviation represented by error bars. We see that the standard deviation is approximately $\sigma = .05$ for each point. We then use a linear fit on this data to determine the function,

$$\beta(\theta) = -.35877\theta + .52535, \quad (7.20)$$

for θ in radians. We note that as $\theta \rightarrow 0$, $\beta(\theta) \approx .5$, which gives conservation of mass. Conservation of mass is then replaced by condition (7.18) with (7.20) used to approximate α , and we see below how it compares with the other junction models presented.

As before, we consider Riemann initial conditions, and determine the effect of those conditions and the geometry of the junction on the error between the one and two-dimensional solutions. For simplicity and to attempt to model physically relevant situations, all initial conditions fix the right state to be,

$$\rho_R = 1 \quad u_R = 0 \quad p_R = 1. \quad (7.21)$$

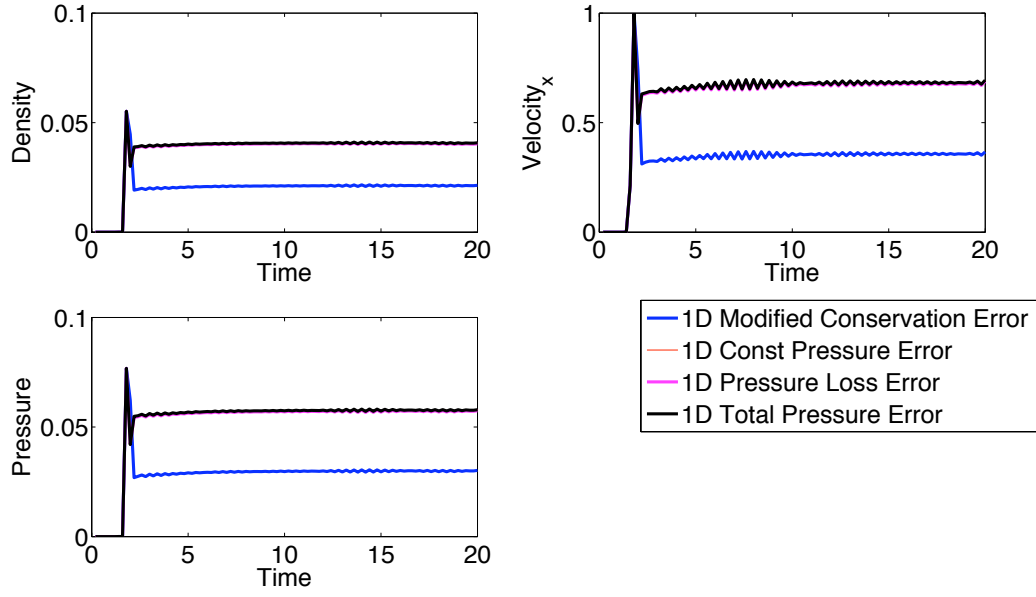


Figure 7.10: Relative error results for the density, velocity and pressure for initial conditions (7.22) and junction geometry $\theta = \frac{\pi}{6}, \psi = 2$.

Fixing the velocity to be zero in the right-hand pipe makes sense since we are simulating flow from left to right. There are two degrees of freedom in our geometry, the angle θ and the pipe area ratio ψ . Both of these will be varied and their effects noted.

We begin by fixing the geometry to be $\theta = 30^\circ$ and $\psi = 2$ and consider the affect of the initial conditions. The following left states are considered,

$$\rho_L = 1 \quad u_L = .2c_L \quad p_L = 1 \quad (7.22)$$

$$\rho_L = 1 \quad u_L = .5c_L \quad p_L = 1 \quad (7.23)$$

$$\rho_L = 1 \quad u_L = .8c_L \quad p_L = 1. \quad (7.24)$$

The relative error at the outlet between the one and two-dimensional solutions for these initial conditions is shown in Figures 7.10-7.12. . We see that as the velocity of the flow into the junction increases the error also increases. This says that as the inflow velocity increases, the two-dimensional effects increase as well.

We next fix the initial conditions and study the affect of the geometry on the error.

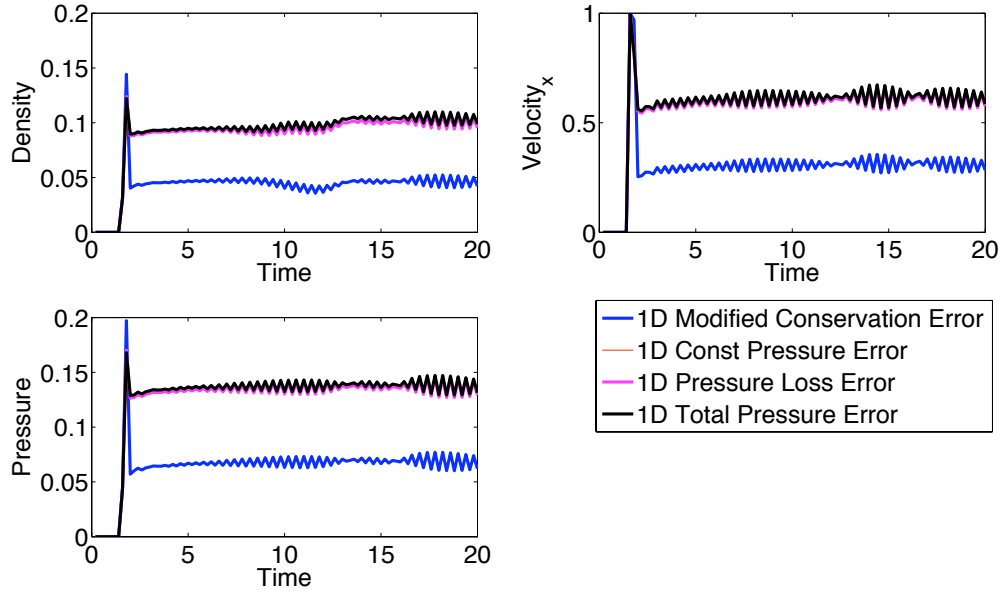


Figure 7.11: Relative error results for the density, velocity and pressure for initial conditions (7.23) and junction geometry $\theta = \frac{\pi}{6}, \psi = 2$.

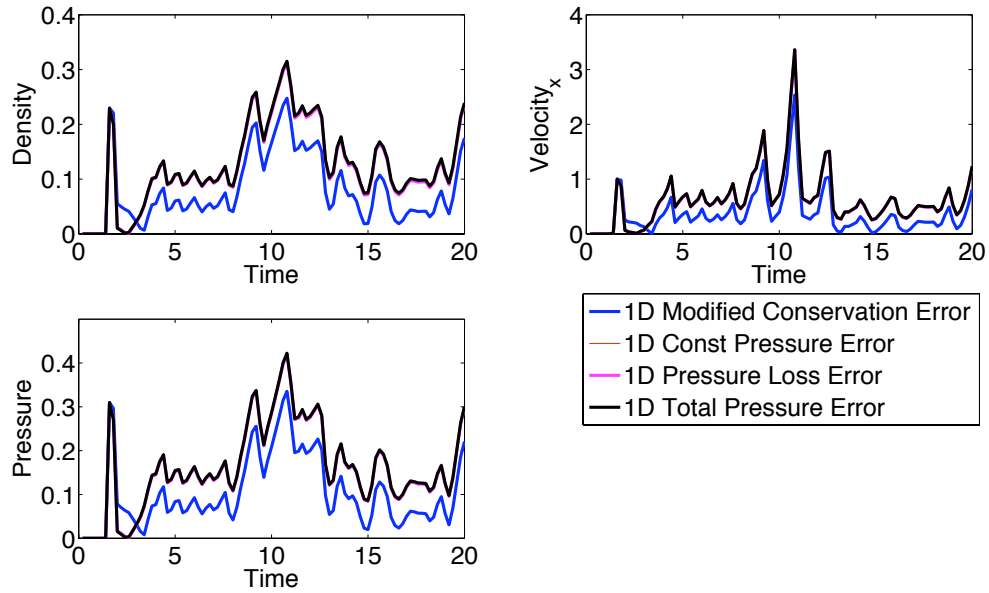


Figure 7.12: Relative error results for the density, velocity and pressure for initial conditions (7.24) and junction geometry $\theta = \frac{\pi}{6}, \psi = 2$.

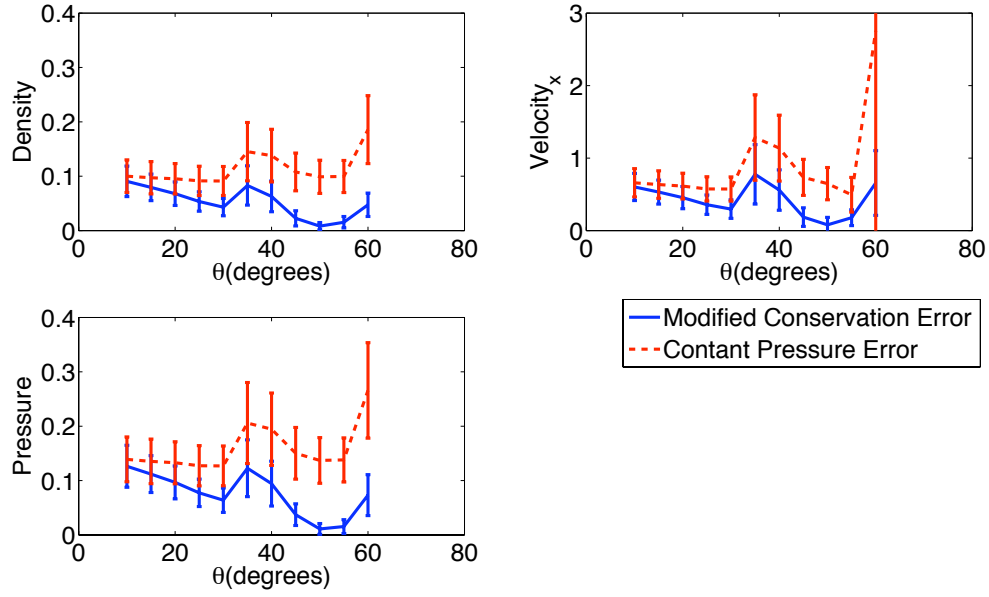


Figure 7.13: Plot of average error for each variable vs angle.

For initial conditions, we use (7.23). The pipe area ratio is fixed at $\psi = 2$ and we vary the angle of the junction. We look at results for the constant pressure model and the modified model described above. To better visualize the dependency on the angle, we again consider the average error over time, as done above. These results are plotted in Figure 7.13. We see that the error does not depend monotonically on the angle of the junction, there are minimums at approximately 30° and 50° .

We also consider how the error changes as the pipe area ratio ψ changes. For this trial, we again use the initial conditions (7.23), and fix the junction angle to be $\theta = 30^\circ$. We vary the area ratio from $\psi = 1$ to $\psi = 2$, and calculate the average result in the same way as above. Figure 7.14 shows the results. We see that as a function of ψ the error is roughly monotonic, with the exception of $\psi = 1$.

Finally, for all the examples given above, we see that the error in the velocity variable is significantly larger than for the density or pressure. This can be explained by examining the two-dimensional solution along the entire domain. Figure 7.15 shows the horizontal velocity for the junction. As we can see, a separation region forms for the horizontal velocity. This type of multi-dimensional effect can not be modeled by the one-dimensional

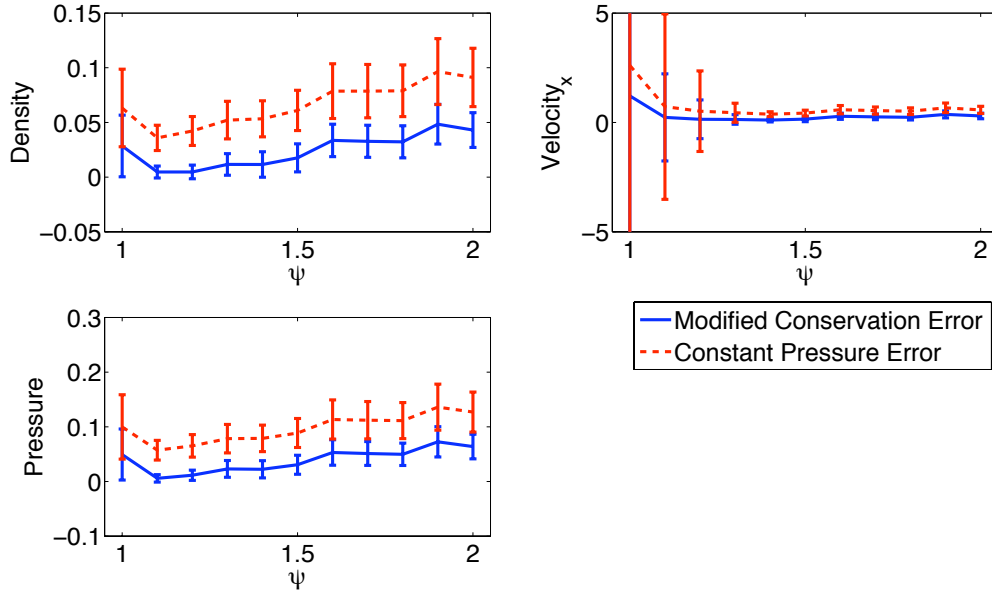


Figure 7.14: Plot of average error for each variable vs ψ .

equations and junction conditions, therefore, it is difficult for the velocities of the two models to agree.

We see from the results above that the modified junction conditions approximate the two-dimensional solution better than any of the other conditions in each case. To validate the modified junction conditions further, we consider another set of initial conditions given by,

$$\rho_L = 1 \quad u_L = 0 \quad p_L = 2. \quad (7.25)$$

$$(7.26)$$

with geometry given by $\theta = 30^\circ$ and $\psi = 2$. The error results are shown in Figure 7.16 and we see that once again the modified junction conditions have significantly less error than the other junction conditions. The spike in the density error is explained by the fact that the contact discontinuity does not line up between the one-dimensional and two-dimensional models.

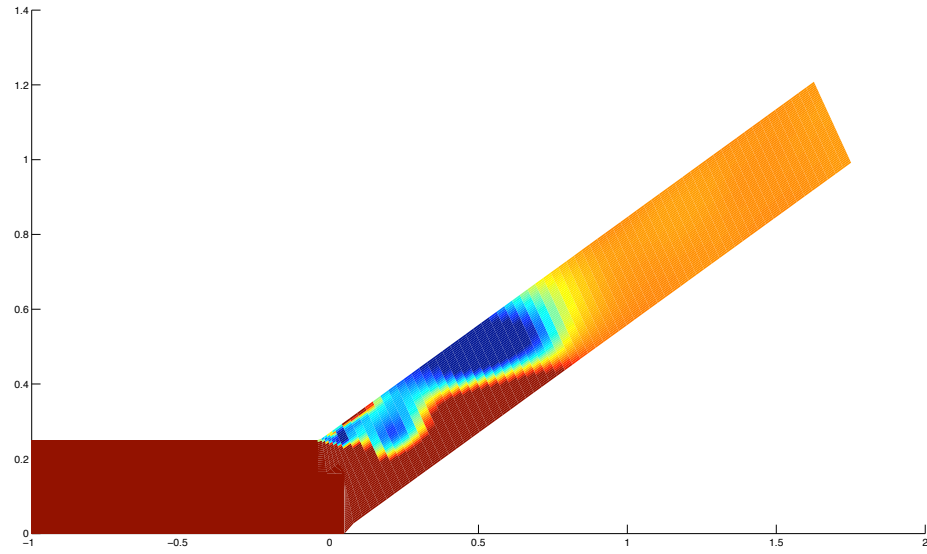


Figure 7.15: Two-dimensional solution of the horizontal velocity. Multi-dimensional effects are seen beyond that of a propagating shock wave.

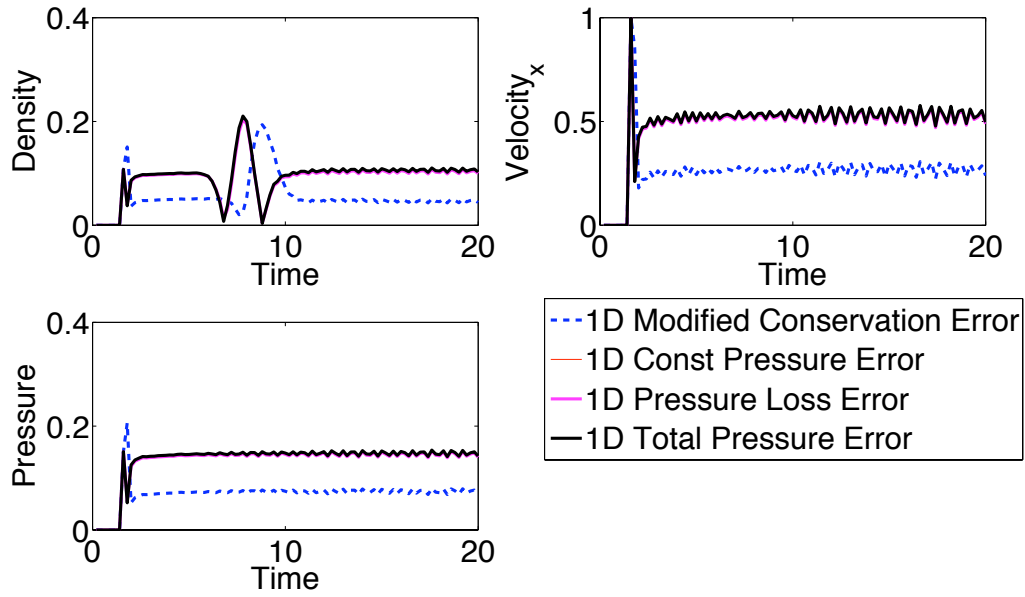


Figure 7.16: A test of the modified junction conditions with different initial conditions.

7.4 Conclusions

Unlike the nozzle junction, a split junction is one where physical approximations play an important role. We see in the three main pressure conditions presented above how approximations are made, especially in the pressure loss model. We also see approximations made by assuming conservation of mass and energy. While these assumptions seem quite reasonable, upon considering the two-dimensional solution conservation of mass does not appear to hold. By incorporating data from the two-dimensional solution, we are able to obtain a more accurate model. A main benefit of this modified model is that it takes the geometry of the junction into account. While the pressure loss model also does this, we see that it does not offer much benefit over the other classical models. This is because of the many assumptions made in the derivation of the pressure loss model. These assumptions, especially incompressibility, do not hold for the junction we consider here. However, the assumption made for the modified method do hold roughly, and thus that method yields better results.

Chapter 8

Conclusions

In this work, we consider two separate problems, laser drilling and transport network problems. While these two problems are obviously quite different in application, they both use a common mathematical technique, dimensional reduction. Dimensional reduction in the form of radial averaging is used in the laser model to simplify the computation. Network problems implement dimensional reduction to model multi-dimensional phenomena on a graph. In particular, radial averaging is used to model gas flow through various pipe junctions, and determine algebraic conditions that approximate the flow through those junctions.

In the laser drilling work, we examine many models for laser drilling already in existence, and look for ways to incorporate these models in a simplified version for quick computation. The key component in the simplified model we present is in the heat transfer portion of the model. Here we radially average the heat equations, allowing for an axisymmetric geometry to be specified, while reducing the computation to that of a one-dimensional heat equation. This reduces the computational cost and allows us to use various shapes for the geometry of the hole. Well-known kinetic theory is also incorporated into the model to account for the rapid evaporation due to the laser. Finally, experimental data is used to determine the best fit for the aspect ratio of the hole.

For the transport network problems, we begin by applying the domain decomposition method to these problems. Little research has been done in this area. We first describe how to implement junction conditions in the linear case. We then implement the domain decomposition method for the linear acoustics equations and develop theory to estimate *a priori* the number of iterations needed for the method to converge. This

is done for multiple cases depending on the equations defined on each edge and how the network is partitioned. These convergence estimations are then tested against numerical experiments and are found to hold with the exception that extra iterations are required to account for the discretization error. We also perform numerical experiments to show that how the network is partitions can affect the number of iterations needed for convergence.

A practical application of network problems is examined, in particular gas flow through a network of pipes. We look specifically at the local region of gas flow through various type of junctions. First, we consider a nozzle junction. The governing equations are derived for one-dimensional nozzle flow via radial averaging, and we see that the junction conditions are implicit within the governing equations. Well-know properties of the solution of the Riemann problem for these equations are stated. We then use some of these properties to determine conditions on the initial states that give good agreement between the one-dimensional and axisymmetric solutions.

The next junction that we consider is the splitting junction. Various conditions have been postulated, and all of these are implemented in our work. In addition to these well-known conditions, we use the numerical data from our two-dimensional simulation of the splitting junction to derive a modified junction condition. We compare these various models with the two-dimensional data and find that in many cases our modified model agrees with the data better than the known models. We examine how the error in the models is affected by the initial conditions and geometry of the junction, and show our results.

The extent of this work has covered many different ideas, involving modeling of kinetic processes and heat transfer, numerical methods applied to new and interesting problems, and examination and improvement of existing one-dimensional approximations of gas flow. Dimensional reduction is used throughout to simplify the models in an efficient manner.

REFERENCES

- [1] M. von Allmen, *Laser Drilling Velocities in Metals*, J. Appl. Phys., **47** (1976), pp. 5460-5463.
- [2] L. A. N. Amaral, A. Scala, M. Barthélemy, and H. E. Stanley, *Classes of small-world networks*, Proc. Natl. Acad. Sci. USA, **97** (2000), pp. 11149-11152.
- [3] N. Andrianov, and G. Warnecke, *On the solution to the Riemann problem for the compressible duct flow*, SIAM J. Appl. Math., **64** (2004), pp. 878-901.
- [4] M. Banda, M. Herty, and A. Klar, *Gas flow in pipeline networks*, Networks and Heterogeneous Media, **1** (2006), pp. 41-56.
- [5] M. D. Bassett, D. E. Winterbone, and R. J. Pearson, *Calculation of steady flow pressure loss coefficients for pipe junctions*, Proc. Instn. Mech. Engrs., **215** (2001), pp. 861-881.
- [6] M. D. Bassett, R. J. Pearson, N. P. Fleming, and D. E. Winterbone, *A multi-pipe junction model for one-dimensional gas-dynamic simulations*, SAE Transactions, **112** (2003), pp. 565-583.
- [7] P. S. Bearman, J. Moody, and K. Stovel, *Chains of affection: The structure of adolescent romantic and sexual networks*, American J. of Sociology, **110** (2002), pp. 44-91.
- [8] R. S. Benson, *The Thermodynamics and Gas Dynamics of Engine Manifolds*, Vol. 1, Oxford University Press, New York, 1982.
- [9] S. Bianchini, and A. Bressan, *Vanishing viscosity solutions of nonlinear hyperbolic systems*, Annals of Mathematics, **161** (2005), pp. 223-342.
- [10] C. Cercignani, *The Boltzman Equation and its Applications*, Springer-Verlag, New York, 1988.
- [11] C. Cercignani, *Rarefied Gas Dynamics: From Basic Concepts to Actual Calculations*, Cambridge University Press (2000).
- [12] C. L. Chan, and J. Mazumder, *One-dimensional steady-state model for damage by vaporisation and liquid expulsion due to laser-material expulsion*, J. Appl. Phys. **62** (1987), pp. 4579-4586.
- [13] W. S. Chang, and S. J. Na, *A study on the prediction of the laser weld shape with varying heat source equations and the thermal distortion of a small structure in micro-joining*, J. Material Processing Tech., **120** (2002), pp. 208-214.
- [14] G. Chryssolouris, *Laser Machining: Theory and Practice*, Springer-Verlag (1991).
- [15] R. M. Colombo, and M. Garavello, *On the p-system at a junction*, Contemporary Mathematics, **426** (2007), pp. 193-217.

- [16] R. M. Colombo, and C. Mauri, *Euler system for compressible fluids at a junction*, J. of Hyperbolic Differential Equations, **5** (2008), pp. 547-568.
- [17] R. M. Colombo, and M. Garavello, *On the 1D modeling of fluid flowing through a junction*, Preprint, 2009.
- [18] R. M. Colombo, and F. Marcellini, *Smooth and discontinuous junctions in the p-system*, J. Math. Anal. Appl., **361** (2009), pp. 440-456.
- [19] R. M. Colombo, and F. Marcellini, *Coupling conditions for the 3×3 Euler system*, Quaderno di Matematica n. 15/2009, Dipartimento di Matematica e Applicazioni, Universita di Milano-Bicocca. Submitted, 2009.
- [20] J. M. Corberán, *A new constant pressure junction model for N-branch junctions*, Proc. Int. Mech. Engin., **206** (1992), pp. 117-123.
- [21] A. Corcoran, L. Sexton, B. Seaman, P. Ryan, and G. Byrne, *The laser drilling of multi-layer aerospace material systems* J. Mat. Processing Tech., **123** (2002), pp. 100-106.
- [22] K. DeVault, P. A. Gremaud, V. Novak, M. S. Olufsen, G. Vernières, and P. Zhao, *Blood flow in the Circle of Willis: Modeling and calibration*, Multiscale Model. Simul., **7** (2008), pp. 888-909.
- [23] K. DeVault, *Numerical Study of Two Problems in Fluid Flow: Cavitation and Cerebral Circulation*, Ph.D Thesis, Department of Mathematics, North Carolina State University, 2008.
- [24] R. Diestel, *Graph Theory*, Springer-Verlag (2006).
- [25] P. S. Dodds, and D. H. Rothman, *Geometry of river networks*, Phys. Rev. E, **63** (2001), art. no. 016115, 016116, 016117.
- [26] F. Dubois, and P. LeFloch, *Boundary conditions for nonlinear hyperbolic systems of conservation laws*, J. Diff. Eq., **71** (1988), pp. 93-122.
- [27] P. Embid, J. Goodman, and A. Majda, *Multiple steady states for 1-D transonic flow*, SIAM J. Sci. Stat. Comput., **5** (1984), pp. 21-41.
- [28] M. J. Gander, L. Halpern, and F. Nataf, *Optimal convergence for overlapping and non-overlapping Schwarz waveform relaxation*, in Eleventh International Conference of Domain Decomposition Methods, C. H. Lai, P. Bjørstad, M. Cross, and O. Widlund, eds., DDM.org, Augsburg, 1999, pp. 27-36.
- [29] M. J. Gander, L. Halpern, and F. Nataf, *Optimal Schwarz waveform relaxation for the one dimensional wave equations*, SIAM J. Numer. Anal., **41** (2003), pp. 1643-1681.
- [30] R.K. Ganesh, and A. Faghri, *A generalized thermal modeling for laser drilling process- I. Mathematical modeling and numerical methodology*, Int. J. Heat Mass Transfer, **40** (1997), pp. 3351-3360.

- [31] M. Garavello, and B. Piccoli, *Traffic flow on a road network using the Aw-Rascle model*, Comm. in Partial Differential Equations, **31** (2006), pp. 243-275.
- [32] H. M. Glaz, and T. P. Liu, *The asymptotic analysis of wave interactions and numerical calculations of transonic nozzle flow*, Advances in Applied Mathematics, **5** (1984), pp. 111-146.
- [33] E. Godlewski, and P. A. Raviart, *Numerical Approximation of Hyperbolic Systems of Conservation Laws*, Springer, New York, 1996.
- [34] S. D. Godunov, *A difference method for numerical colculation of discontinuous solutions of the equations of hydrodynamics*, Mat. Sb. **47** (1959), pp. 271-306.
- [35] W. H. Hagar, *An approximate treatment of flow in branches and bends*, proc. Int. Mech. Engin., **198C** (1984), pp. 63-69.
- [36] A. Harten, *High resolution schemes for hyperbolic conservation laws*, J. Comput. Phys., **49** (1983), pp. 357-393.
- [37] H. Holden, and N. H. Risebro, *A mathematical model of traffic flow on a network of unidirectional roads*, SIAM J. Math. Anal., **26** (1995), pp. 999-1017.
- [38] B. A. Huberman, *The Laws of the Web*, MIT Press, Cambridge, 2001.
- [39] A. Jameson, W. Schmidt, and E. Turkel, *Numerical solution of the Euler equations by finite volume methods using Runge-Kutta time stepping schemes*, AIAA paper No. 81-1259, 1981.
- [40] G. Jiang, and C. W. Shu, *Efficient implementation of weighted ENO schemes*, J. Comput. Phys., **126** (1996), pp. 202-228.
- [41] A. Kar, and J. Mazumder, *Two-Dimensional Model for Material Damage due to Melting and Vaporisation during Laser Irradiation*, J. Appl. Phys., **68** (1990), pp. 3884-3891.
- [42] C. G. Khan Malek, *Laser processing for bio-microfluidics applications (part II)*, Anal. Bioanal. Chem., **385** (2006) pp.1362-1369.
- [43] C.J. Knight, *Theoretical modeling of rapid surface vaporization with back pressure*, AIAA Journal, **17** (1979), pp. 519-523.
- [44] H. O. Kreiss, *Initial boundary value problems for hyperbolic systems*, Comm. Pure. Appl. Math., **23** (1970), pp. 217-243.
- [45] D. Kröner, and M. D. Thanh, *Numerical solutions to compressible flows in a nozzle with variable cross-section*, SIAM J. Numer. Anal., **43** (2005), pp. 796-824.
- [46] A. Kurganov, and E. Tadmor, *New high-resolution central scheme for nonlinear conservation laws and convection-diffusion equations*, J. Comp. Phys., **160** (2000), pp. 241-282.

- [47] A. Kurganov, S. Noelle, and G. Petrova, *Semidiscrete central-upwind schemes for hyperbolic conservation laws and Hamilton-Jacobi equations*, SIAM J. Sci. Comput., **23** (2001), pp. 707-740.
- [48] J. E. Lagnese, and G. Leugering, *Dynamic domain decomposition in approximate and exact boundary control in problems of transmission for wave equations*, SIAM J. Control Optim., **38** (2000), pp. 503-537.
- [49] V. Latora, and M. Marchiori, *Is the Boston subway a small world network?*, Phys. A, **314** (2002), pp. 109-113.
- [50] P. D. Lax, *Shock waves and entropy*, in Contribution to Nonlinear Functional Analysis, E. H. Zarantonello, ed., Academic Press, New York, 1971, pp. 603-634.
- [51] B. van Leer, *Towards the ultimate conservative difference scheme. V. A second order sequel to Godunov's method*, J. Comput. Phys., **32** (1979), pp. 101-136.
- [52] P. G. LeFloch, and M. D. Thanh, *The Riemann problem for fluid flows in a nozzle with discontinuous cross-section*, Comm. in Math. Sci., **4** (2003), pp. 763-796.
- [53] G. Leugering, *Dynamic domain decomposition of optimal control problems for networks of strings and Timoshenko beams*, SIAM J. Control Optim., **37** (1999), pp. 1649-1675.
- [54] G. Leugering, *Domain decomposition of optimal control problems for dynamic networks of elastic strings*, Computational Optimization and Applications, **16** (2000), pp. 5-27.
- [55] R. J. LeVeque, *Finite Volume Methods for Hyperbolic Problems*, Cambridge University Press, Cambridge, UK, 2002.
- [56] S. A. Levin, B. T. Grenfell, A. Hastings, and A. S. Perelson, *Mathematical and computational challenges in population biology and ecosystem science*, Science, **275** (1997), pp. 334-343.
- [57] R. Li, and T. Erneux, *Preferential instability in arrays of coupled lasers*, Physical Review A, **46** (1992), pp. 4252-4260.
- [58] P.-L. Lions, *On the Schwartz alternating method*, Proc. First International Sympos. on Domain Decomposition Method for Partial Differential Equations, SIAM, Philadelphia, PA, 1988.
- [59] T. P. Liu, *Transonic gas flow in a duct of varying area*, Arch. Rat. Mech. Anal., **23** (1982), pp. 1-18.
- [60] T. P. Liu, *Nonlinear stability and instability of transonic flows through a nozzle*, Commun. Math. Phys., **83** (1982), pp. 243-260.
- [61] X. D. Liu, S. Osher, and T. Chan, *Weighted essentially non-oscillatory schemes*, J. Comput. Phys., **115** (1994), pp. 200-212.

- [62] P. Marliolis, *Interlocking directorates and control of corporations: The theory of bank control*, Social Sci. Quart., **56** (1975), pp. 425-439.
- [63] A. Maritan, A. Rinaldo, R. Rigon, A. Giacometti, and I. Rodríguez-Iturbe, *Scaling laws for river networks*, Phys. Rev. E, **53** (1996), pp. 1510-1515.
- [64] A. M. Miermanov, *Zadacha Stefana*, Nauka, Novosibirsk, 1986.
- [65] J. Miettinen, *Calculation of solidification-related thermophysical properties for steels*. Metallurgical and Materials Trans. B, **28** (1997), pp.281-297.
- [66] S. Milgram, *The small world problem*, Psych. Today, **2** (1967), pp. 60-67.
- [67] H. Nessyahu, and E. Tadmor, *Non-oscillatory central differencing for hyperbolic conservation laws*, J. Comput. Phys., **87** (1990), pp. 408-463.
- [68] M. E. J. Newman, *The structure and function of complex networks*, SIAM Review, **45** (2003), pp. 167-256.
- [69] S. Nicaise, *Some results on spectral theory over networks, applied to nerve impulse transmission* Lecture Notes in Mathematics, Vol. 1771 (Berlin, Springer), pp. 532-541.
- [70] J. Oliger, and A. Sundström, *Theoretical and practical aspects of some initial boundary value problems in fluid dynamics*, SIAM J. Appl. Math., **35** (1978), pp. 419-446.
- [71] S. Osher, and E. Tadmor, *On the convergence of difference approximations to scalar conservation laws*, Math. Comput., **50** (1988), pp. 19-51.
- [72] Y. V. Pokornyi, and A. V. Borovskikh, *Differential equations on networks (Geometric graphs)*, J. of Math. Science, **119** (2004), pp. 691-718.
- [73] A. Quarteroni and A. Valli, *Domain Decomposition Method for Partial Differential Equations*, Oxford University Press, New York, 1999.
- [74] P.N. Ramachandran Nair, Marc M. Baltensperger, Hans-Ulrich Luder, and Gerold K.H. Eyrich, *Pulpal Response to Er:YAG Laser Drilling of Dentine in Healthy Human Third Molars*, Lasers in Surgery and Medicine, **32** (2003), pp. 203-209.
- [75] S. Raman, J. Jeong, S.J. Kim, B. Sun, and K. Park, *Laser (UV) microvia application in cellular technology*, Circuit World, **26** (1999), pp.11-15.
- [76] John F. Ready, *Industrial Applications of Lasers*, Academic Press (1997).
- [77] P. L. Roe, *Approximate Riemann solvers, parameter vectors, and difference schemes*, J. Comput. Phys., **43** (1981), pp. 357-372.
- [78] D. Rugar, P. Hansma, *Atomic Force Microscopy*, Physics Today, October (1990), pp. 23-30.
- [79] S. Sankaranarayanan, H. Emminger, and A. Kar, *Energy loss in the plasma during laser drilling*, J. Phys. D: Appl. Phys., **32** (1999), pp. 1605-1611.

- [80] J. Scott, *Social Network Analysis: A Handbook*, Sage, London, 2000.
- [81] C. W. Shu, *Essentially non-oscillatory and weighted essentially non-oscillatory schemes for hyperbolic conservation laws*, in Advance Numerical Approximation of Nonlinear Hyperbolic Equations, A. Quarteroni, ed., Lecture Notes in Mathematics, Springer, New York, 1998, Vol. 1697, pp. 325.
- [82] M. Shusser, *Kinetic theory analysis of laser ablation of carbon: Applicability of one-dimensional models* J. of Applied Physics, **101** (2007).
- [83] B. Smith, P. Bjørstad, and W. Gropp, *Domain Decomposition: Parallel Multilevel Methods for Elliptic Partial Differential Equations*, Cambridge University Press, Cambridge, UK, 1996.
- [84] P. Solana, P. Kapadia, J.M. Dowden, and P.J. Marsden, *An analytical model for the laser drilling of metals with absorption within the vapour* J. Phys D: Appl. Phys., **32** (1999), pp. 942-952.
- [85] M. D. Thanh, *The Riemann problem for a nonisentropic fluid in a nozzle with discontinuous cross-sectional area*, SIAM J. Appl. Math., **69** (2009), pp. 1501-1519.
- [86] C. H. Townes, *The first laser*, in A Century of Nature: Twenty-One Discoveries that Changed Science and the World, L. Garwin, and T. Lincoln, eds., University of Chicago Press, Chicago, 2003, pp. 107-112.
- [87] J. Tu, *Personal Communication*, Dept. of Aerospace and Mechanical Engineering, North Carolina State University, 2008.
- [88] K.T. Voisey, S.S. Kudesia, W.S.O. Rodden, D.P. Hand, J.D.C. Jones, T.W. Clyne, *Melt ejection during laser drilling of metals*, Materials Science and Engineering, A356 (2003), 414-424.
- [89] D. J. Watts, and S. H. Strogatz, *Collective dynamics of "small world" networks*, Nature, **393** (1998), pp. 440-442.
- [90] K. Wiesenfeld, P. Colet, and S. H. Strogatz, *Frequency locking in Josephson arrays: Connection with the Kuramoto model*, Physical Review A, **57** (1998), pp. 1563-1569.
- [91] J. Xu, *Iterative methods by space decomposition and subspace correction*, SIAM Review, **34** (1992), pp. 581-613.
- [92] B.S. Yilbas, A.Z. Sahin, R. Davies, *Laser heating mechanism including evaproation process initiating laser drilling*, Int. J. , Mach. Tools and Manufacture. Vol. 35 (1995), pp.1047-1062.
- [93] B.S. Yilbas, M. Kanyon, *Analytical solution for pulsed laser heating process:convective boundary condition case*, Int. J. Heat Mass Transfer, **45** (2002), pp. 1571-1582.
- [94] B.S. Yilbas, and S.B. Mansoor, *Laser evaporative heating of surface: simulation of flow field in the laser produced cavity*, J. Phys. D: Applied Physics, **39** (2006), pp. 3863-3875.

- [95] T. Ytrehus, and S. Ostmo, *Kinetic Theory Approach to Interphase Processes*, Int. J. Multiphase Flow, **22** (1996), pp. 133-155.
- [96] H. Yuan, *On transonic shocks in two-dimensional variable-area ducts for steady Euler system*, SIAM J. Math. Anal., **38** (2007), pp. 1343-1371.

APPENDICES

Appendix A

Analysis of Φ

Here we summarize properties of solutions to

$$\Phi(\rho) := -\frac{2\kappa\gamma}{\gamma-1}\rho^{\gamma+1} + \left(u_0^2 + \frac{2\kappa\gamma}{\gamma-1}\rho_0^{\gamma-1}\right)\rho^2 - \left(\frac{a_0u_0\rho_0}{a_1}\right)^2 = 0. \quad (\text{A.1})$$

We give conditions for when (A.1) has one, two or no solutions, and present a selection criterion for choosing between the two solutions when they exist. First we note that if $u_0 = 0$, the solution is simple to obtain and the only non-vacuum solution is $\rho = \rho_0$. Therefore, let us assume $u_0 \neq 0$. We note that for any zero of (A.1),

$$-\frac{2\kappa\gamma}{\gamma-1}\rho^{\gamma+1} + \left(u_0^2 + \frac{2\kappa\gamma}{\gamma-1}\rho_o^{\gamma-1}\right)\rho^2 = \left(\frac{a_0u_0\rho_0}{a_1}\right)^2, \quad (\text{A.2})$$

which implies,

$$-\frac{2\kappa\gamma}{\gamma-1}\rho^{\gamma+1} + \left(u_0^2 + \frac{2\kappa\gamma}{\gamma-1}\rho_o^{\gamma-1}\right)\rho^2 > 0. \quad (\text{A.3})$$

Equation (A.3) can be used to determine an interval in which zeros of (A.1) must exist,

$$0 < \rho < \hat{\rho} := \left(\frac{\gamma-1}{2\kappa\gamma}u_0^2 + \rho_0^{\gamma-1}\right)^{\frac{1}{\gamma-1}}. \quad (\text{A.4})$$

Therefore we need only look for solutions to $\Phi = 0$ within the interval $\rho \in (0, \hat{\rho})$. We next look for critical points of Φ to determine how many zeros it has within this interval.

We take the derivative of Φ with respect to ρ ,

$$\frac{d\Phi}{d\rho} = -2\kappa\gamma\frac{\gamma+1}{\gamma-1}\rho^\gamma + 2\left(u_0^2 + \frac{2\kappa\gamma}{\gamma-1}\rho_0^{\gamma-1}\right)\rho. \quad (\text{A.5})$$

We see that there exists one critical point ρ_{\max} within the interval of interest $(0, \hat{\rho})$,

$$\rho_{\max} = \left(\frac{\gamma-1}{\kappa\gamma(\gamma+1)}u_0^2 + \frac{2}{\gamma+1}\rho_0^{\gamma-1}\right)^{\frac{1}{\gamma-1}}, \quad (\text{A.6})$$

and that

$$\frac{d\Phi(\rho)}{d\rho} > 0 \quad \rho \in (0, \rho_{\max}) \quad (\text{A.7})$$

$$\frac{d\Phi(\rho)}{d\rho} < 0 \quad \rho \in (\rho_{\max}, \hat{\rho}). \quad (\text{A.8})$$

So there exists a single maximum point within our interval of interest. Finally we examine $\Phi(0)$ and $\Phi(\hat{\rho})$, to find that

$$\Phi(0) = \Phi(\hat{\rho}) = -\left(\frac{a_0 u_0 \rho_0}{a_1}\right)^2 < 0. \quad (\text{A.9})$$

Putting all of this information together, we can determine the general structure of $\Phi(\rho)$. There are three cases of interest, depending on $\Phi(\rho_{\max})$, that are shown in Figure A.1. It is clearly seen that a real solution will exist if,

$$\Phi(\rho_{\max}) \geq 0. \quad (\text{A.10})$$

This condition can be translated to a condition on the geometry of the nozzle, namely on the ratio of the areas,

$$\frac{a_1}{a_0} \geq a_{\min} := \frac{\rho_0 |u_0|}{\sqrt{\kappa\gamma} \rho_{\max}^{\frac{\gamma+1}{2}}}. \quad (\text{A.11})$$

Using this condition on the geometry, we can state the three cases for finding a zero of

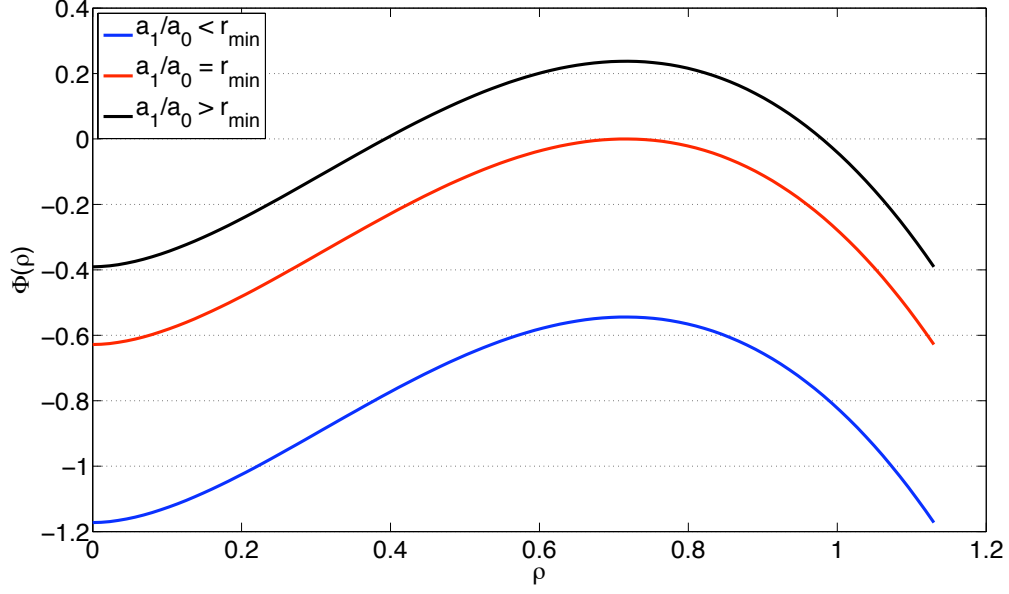


Figure A.1: Plot of $\Phi(\rho)$, for $\rho \in [0, \hat{\rho}]$. Area ratio is varied to show examples of two solutions, one solution and no solutions.

$\Phi(\rho)$,

$$\rho = \begin{cases} \rho_* < \rho_{\max} \text{ OR } \rho^* > \rho_{\max} & \text{if } \frac{a_1}{a_0} > a_{\min} \\ \rho_* = \rho^* = \rho_{\max} & \text{if } \frac{a_1}{a_0} = a_{\min} \\ \text{No real solution} & \text{if } \frac{a_1}{a_0} < a_{\min} \end{cases} \quad (\text{A.12})$$

Therefore, for a given fixed state $U_0 = (\rho_0, u_0, p_0, a_0)$, if the area ratio $\frac{a_1}{a_0} < a_{\min}(U_0)$, no 0-contact discontinuity will exist.

We give a lemma which is helpful in determining the selection criterion between the two zeros of Φ .

Lemma 3. *Let $U_0 = (\rho_0, u_0, p_0)$ be a fixed state on one side of the contact discontinuity and a_0, a_1 be the areas on either side such that $\frac{a_1}{a_0} > a_{\min}$, i.e. two real zeros ρ_* and ρ^* exist for $\Phi(\rho)$. Let $U_* = (\rho_*, u_*, p_*)$ and $U^* = (\rho^*, u^*, p^*)$ be the states corresponding to*

the two zeros. Then we have that

$$U_* \in \mathcal{G}_1 \cup \mathcal{G}_4 \quad (\text{A.13})$$

$$U^* \in \mathcal{G}_2 \cup \mathcal{G}_3 \quad (\text{A.14})$$

Moreover, whenever $U_0 \in \mathcal{G}_i$, either $U_* \in \mathcal{G}_i$ or $U^* \in \mathcal{G}_i$.

Proof. First we define a function g ,

$$\begin{aligned} g(\rho, U_0) &= u(\rho, U_0)^2 - c(\rho, U_0)^2 = u(\rho, U_0)^2 - \sqrt{\frac{\gamma p(\rho, U_0)}{\rho}} \\ &= u_0^2 + \frac{2\kappa\gamma}{\gamma-1}(\rho_0^{\gamma-1} - \rho^{\gamma-1}) - \kappa\gamma\rho^{\gamma-1} \end{aligned} \quad (\text{A.15})$$

where $u(\rho, U_0)$ and $p(\rho, U_0)$ correspond to a solution ρ of the jump conditions (6.32)-(6.34). Above we rewrite g in terms of ρ by using the jump relations (6.33) and (6.34) that must hold across the contact discontinuity. To prove statements (A.13) and (A.14), we show that $g(\rho_*) > 0$ and $g(\rho^*) < 0$ respectively. By calculation, we can see that,

$$g(\rho_{\max}) = 0. \quad (\text{A.16})$$

Also, by examining the derivative with respect to ρ we get,

$$\frac{dg}{d\rho} = -\kappa\gamma(\gamma+1)\rho^{\gamma-2} < 0 \quad \forall \rho \in [0, \hat{\rho}]. \quad (\text{A.17})$$

Hence, $g(\rho)$ is a monotone decreasing function with respect to ρ . Since we know that

$$\rho_* < \rho_{\max} < \rho^*, \quad (\text{A.18})$$

this implies that

$$g(\rho_*) > g(\rho_{\max}) = 0 \quad \Rightarrow |u_*| > c \quad (\text{A.19})$$

$$g(\rho^*) < g(\rho_{\max}) = 0 \quad \Rightarrow |u^*| < c \quad (\text{A.20})$$

Therefore, $U_* \in \mathcal{G}_1 \cup \mathcal{G}_4$ and $U^* \in \mathcal{G}_2 \cup \mathcal{G}_3$. Also, from relation (6.32), we know that u_* and u^* have the same sign as u_0 . Hence, one of the two solutions will always be in the

same region as the fixed state U_0 . □

There are multiple ways of defining the selection criterion for the 0-contact discontinuity, however they all reduce to the same basic form. We choose to use the evolutionary discontinuity criterion described in [3]. To this end, we define an evolutionary discontinuity.

Definition 11. Consider a discontinuity Σ in a physical flow, which is governed by a $d \times d$ hyperbolic system. Denote the number of characteristics incoming to Σ by n and coinciding with Σ by c . Further, denote the number of unknown variables on both sides of Σ together with the speed of Σ by $N = 2d + 1$, and the number of relations across Σ by m . Then Σ is called **evolutionary** if

$$N = n + c + m.$$

The idea is that all unknowns across the discontinuity can be determined from the incoming and coinciding characteristics and the relations across the discontinuity. In a strictly hyperbolic system, the evolutionarity criterion is equivalent to the Lax shock condition.

For a contact discontinuity, such as the one we are considering, this criterion says that the number of impinging characteristics on one side must be equal to the number of characteristics leaving on the other side. This is clearly equivalent to saying that the eigenvalues do not change sign across the discontinuity. Therefore, if the state on one side is in region \mathcal{G}_i , the state on the other side must also be in region \mathcal{G}_i . Lemma 3 guarantees that if two solutions of the jump conditions exists, then one of them will satisfy the evolutionarity criterion.

Appendix B

Proof of Lemma 2

Proof. We use the relation across the 0-wave to prove the lemma. We start by recalling that $\kappa = \frac{p}{\rho^\gamma}$ is constant across the 0-wave. Using this in Equation (6.32) we get,

$$a_0 u_0 \frac{p_0^{1/\gamma}}{\kappa^{1/\gamma}} = a_1 u_1 \frac{p_1^{1/\gamma}}{\kappa^{1/\gamma}}. \quad (\text{B.1})$$

We rearrange (B.1) to solve for p_1 ,

$$p_1 = \left(\frac{a_0}{a_1} \right)^\gamma p_0 \left(\frac{u_0}{u_1} \right)^\gamma, \quad (\text{B.2})$$

and differentiate with respect to u_1 ,

$$\frac{\partial p_1}{\partial u_1} = -\gamma \left(\frac{a_0}{a_1} \right)^\gamma p_0 u_0^\gamma u_1^{-(\gamma+1)} \quad (\text{B.3})$$

From (B.3) we see that statement 1 is proven.

Taking (B.1), if we rearrange to solve for p_1 and u_1 and then differentiate with respect to p_0 and u_0 respectively, we get,

$$\frac{\partial p_1}{\partial p_0} = \left(\frac{a_0 u_0}{a_1 v_1} \right)^\gamma > 0 \quad (\text{B.4})$$

$$\frac{\partial u_1}{\partial u_0} = \frac{a_0}{a_1} \left(\frac{p_0}{p_1} \right)^{1/\gamma} > 0, \quad (\text{B.5})$$

thus proving statement 2.

For statement 3, we begin by proving that p_1 is bounded. Following [3], we prove this by contradiction, that is assume $p_1 \rightarrow \infty$. We consider relation (6.33), and again eliminate ρ_1 to see,

$$\frac{\gamma}{\gamma-1}p_1^{1-1/\gamma}\kappa^{1/\gamma} < \frac{u_1^2}{2} + \frac{\gamma}{\gamma-1}p_1^{1-1/\gamma}\kappa^{1/\gamma} = \frac{u_0^2}{2} + \frac{\gamma}{\gamma-1}p_0^{1-1/\gamma}\kappa^{1/\gamma}. \quad (\text{B.6})$$

Since we know the right hand side is bounded by the hypothesis, this says $p_1 \nrightarrow \infty$.

Now using (B.1), we see that as $u_0 \rightarrow 0$, $u_1 \rightarrow 0$. Using this fact in (B.3) and the jump relation (6.34), we get that $\rho_1 \rightarrow \bar{\rho}$ and $p_1 \rightarrow \bar{p}$.

□

Appendix C

Pressure Loss Model Derivation

Here we summarize the work done in [5, 6] to derive the pressure loss model implemented for the splitting junction. Figure C.1 shows the geometry of the junction. We consider two control volumes, D-D'-R'-R, and R-R'-E'-E. It is assumed that there is no pressure loss in the first control volume, since within that region the flow is converging. Within the second control volume the flow is diverging, and it is there that the pressure is assumed to change.

The following notation is used throughout the derivation. First, the mass flow ratio is defined to be,

$$q = \frac{\dot{m}_2}{\dot{m}_1}, \quad (\text{C.1})$$

where \dot{m}_i is the mass flow rate within each pipe. Also, the area ratio is defined to be,

$$\psi = \frac{a_1}{a_2}. \quad (\text{C.2})$$

We note the following relationships,

$$u_2 = q\psi u_1 \quad u_R = q\psi \frac{u_1}{\xi}, \quad (\text{C.3})$$

where ξ denotes the ratio of the restricted area to the total pipe area. Next we consider

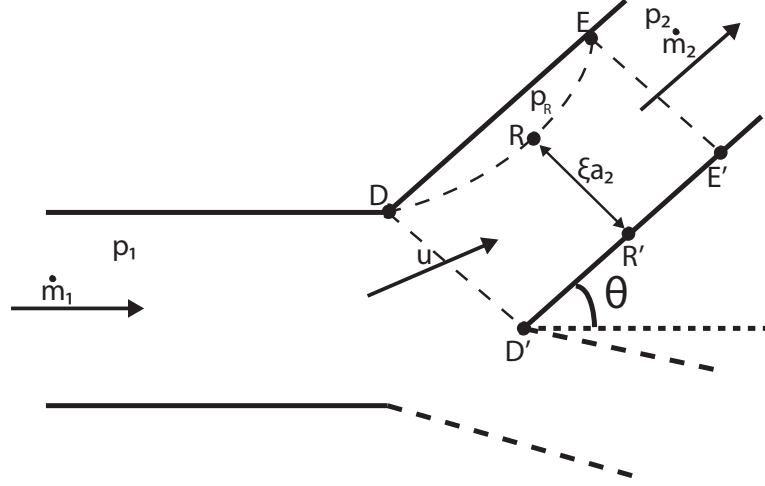


Figure C.1: Diagram of the physics modeled by the pressure loss junction condition.

the momentum equation within the converging control volume D-D'-R'-R, given by,

$$\bar{p}_1 a_2 - p_R a_2 = \dot{m}_2 u_R - \dot{m}_2 u_1 \cos \left[\frac{3}{4}(\theta) \right], \quad (\text{C.4})$$

where \bar{p}_1 is the average pressure along the line D-D' and p_R denotes the pressure along the line R-R'. It is assumed that the pressure at D' is equal to the stagnation pressure in pipe 1, so we have,

$$\bar{p}_1 = \frac{p_1 + p_{01}}{2} = p_1 + \frac{1}{4} \rho u_1^2. \quad (\text{C.5})$$

Since we assume that the pressure is constant within this region, we can use the Bernoulli equation to write,

$$\bar{p}_1 + \frac{1}{2} \rho u_1^2 = p_R + \frac{1}{2} \rho u_R^2. \quad (\text{C.6})$$

By combining Equations (C.3), (C.5), and (C.6), we obtain an equation for p_R ,

$$p_R = p_1 + \frac{1}{2} \rho u_1^2 \left[\frac{3}{2} - q^2 \frac{\psi^2}{\xi^2} \right]. \quad (\text{C.7})$$

We can now combine Equations (C.3), (C.5), and (C.8) to transform Equation (C.4) into,

$$0 = \frac{1}{\xi^2} - \frac{2}{\xi} + \frac{2}{q\psi} \cos \left[\frac{3}{4}(\theta) \right] - \frac{1}{q^2\psi^2} \quad (\text{C.8})$$

which is a quadratic equation for $\frac{1}{\xi}$. We solve this equation to obtain a relationship for $\frac{1}{\xi}$ in terms of the geometric properties of the junction and the mass flow ratio,

$$\frac{1}{\xi} = 1 + \sqrt{1 + \frac{1}{q^2\psi^2} - \frac{2 \cos \left[\frac{3}{4}(\theta) \right]}{q\psi}}. \quad (\text{C.9})$$

Now considering the second control volume R-R'-E'-E, we recall that this is where the pressure change occurs, and therefore Bernoulli's equation is written as,

$$p_R + \frac{1}{2}\rho u_R^2 = p_2 + \frac{1}{2}\rho u_2^2 + \Delta p \quad (\text{C.10})$$

where Δp is the change in pressure through the junction. Examining the momentum equation through this control volume, we have,

$$p_R a_2 - p_2 a_2 = \dot{m}_2 u_2 - \dot{m}_2 u_R. \quad (\text{C.11})$$

We are now able to obtain an equation for the pressure change Δp in terms of the junction geometry, mass flow ratio, and ξ . Combining Equations (C.3), (C.10), and (C.11), we obtain,

$$\Delta p = \frac{1}{2}\rho u_1^2 q^2 \psi^2 \left[1 - \frac{1}{\xi} \right]^2. \quad (\text{C.12})$$

Inserting the solution of $\frac{1}{\xi}$ from Equation (C.9) into (C.12) and rearranging, we obtain the following relationship for the pressures throughout the junction,

$$\frac{p_1 + \frac{1}{2}\rho u_1^2 - (p_2 + \frac{1}{2}\rho u_2^2)}{\frac{1}{2}\rho u_1^2} = q^2 \psi^2 + 1 - 2q\psi \cos \left[\frac{3}{4}(\theta) \right]. \quad (\text{C.13})$$

Assuming conservation of mass, (C.13) can be simplified to,

$$\frac{p_1 + \frac{1}{2}\rho u_1^2 - (p_2 + \frac{1}{2}\rho u_2^2)}{\frac{1}{2}\rho u_1^2} = \frac{1}{4}\psi^2 + 1 - \psi \cos \left[\frac{3}{4}(\theta) \right]. \quad (\text{C.14})$$